Transverse Photonic Doppler Velocimetry for Plate Impact Experiments

Thesis by
Moriah N. Bischann

In Partial Fulfillment of the Requirements for the
degree of
Bachelor of Science

CALIFORNIA INSTITUTE OF TECHNOLOGY
Pasadena, California

2017
(Submitted June 5, 2017)

And above all, watch with glittering eyes the whole world around you because the greatest secrets are always hidden in the most unlikely places.

Roald Dahl
The Minpins

ACKNOWLEDGEMENTS

I was lucky to have extraordinary people influence my formative academic years. I make it a point to express my gratitude in person because I feel as if something personal is lost in the written word. But for my readers, I would like to provide a snapshot of those who have supported my growth.

Thank you to my advisor Professor Guruswami Ravichandran for allowing me freedom to explore my research interests, sharing his knowledge, providing guidance, and giving me the resources I need to achieve my professional goals. His leadership turned my research into a passion. I extend my thanks to Dr. Michael Mello for advising this work. I truly appreciate Christian Kettenbeil for patiently demonstrating how to be a resourceful and resilient experimentalist and engineer. I am grateful for the opportunity to learn from him and work beside him on this project.

I want to thank Professor John F. Brady and Charlie Slominski for introducing me to the realm of theoretical research during my Summer Undergraduate Research Fellowship (SURF) in chemical engineering. Their belief in my abilities reinforced my standing in the Caltech community. I appreciate Dr. Owen Kingstedt, now an Assistant Professor, for teaching me about Split-Hopkinson Pressure Bar experiments during my SURF in aerospace. His steadfast backing encouraged me to confidently communicate my work. I am thankful to Dr. Ryan Rairigh and Dominik Alder at Lockheed Martin for introducing me to manufacturing. They showed me how to lead and inspire with kindness.

My sincere appreciation to Professor Katherine Faber for her interest in my career. I would also like to recognize my academic advisor Professor Julia Greer. I extend my appreciation to Cheryl Gause and Jamie Meighen-Sei for their support.

Thank you to my friends Kimberley Mac Donald and Louisa Avellar who are fellow members of Professor Ravichandran's group for their encouragement and guidance. Finally, thank you to my parents, brother, relatives, and friends for their love, compassion, and strength. We are a family, no matter what stands in our way.

Like runners in a relay race, each has edged me one step closer to my goal. This work is a culmination of everything they have taught me. Thank you for betting on me.

ABSTRACT

High-pressure shock waves propagate in materials when automobiles collide, projectiles impact against bunkers, and mining charges detonate beneath Earth's surface. It is difficult to quantify the behavior of materials experiencing such sudden and high pressures. Specialized interferometry techniques have enabled the study of rapid, high-strain-rate deformation during controlled plate impact testing.

Transverse motion during plate impact experiments is currently measured with the transverse displacement interferometer (TDI). However, the TDI does not take advantage of modern telecommunications technology and data analysis techniques that allow for the measurement of high velocities (in the km/s range) with fine time resolution. We designed and developed a transverse photonic Doppler velocimetry (TPDV) technique for plate impact experiments based entirely on fiber optic components. The TPDV system uses light diffracted from a grating to capture transverse motion. This signal is frequency upshifted to achieve more fringes per unit time. Data is analyzed using spectral analysis techniques to detect micrometer displacements on a nanosecond to microsecond timescale.

We demonstrated the TPDV technique's capabilities with normal impact of single crystalline y-cut α-quartz against borosilicate. We simultaneously collected photonic Doppler velocimetry (PDV) measurements of longitudinal displacements. Finally, we compared our longitudinal and transverse experimental results to theoretical calculations. Our data's orthogonal velocity jumps showed that the TPDV technique accurately detected transient velocities and the magnitudes of longitudinal and shear waves.

Our TPDV technique will facilitate the study of deformation and failure of materials during normal and pressure-shear plate impact. Comprehending shock-wave dominated deformation in materials is important for the design of aerospace structures, understanding planetary impact, and creating shock-mitigating materials.

TABLE OF CONTENTS

LIST OF ILLUSTRATIONS

LIST OF TABLES

Chapter 1

INTRODUCTION

The light that you see with your eyes, the sounds that you hear with your ears, and the vibrations that you feel with your hands have a subtle commonality: waves. Waves allow you to see the colorful flower bloom in the spring, the stars on a dark night, and the face of beloved friends. They allow you to hear the morning chirp of birds and the whisper of the wind. Waves allow you to feel the tremors of the earth and the vibration of your computer as it hums to life. Waves appeal to our senses and shape the way we experience life.

A rigorous study of waves can be traced back to Pythagoras [1]. This Greek philosopher studied how changing the length of a string affected the string's pitch. Vibration dynamics further inspired a mathematical framework for waves in the seventeenth century. Mersenne's law was developed in 1637, and refined in 1713 by Brook Taylor, to explain how the frequency of a string is inversely proportional to its length, proportional to the square root of the force stretching the string, and inversely proportional to the square root of the string's mass per unit length.

The vibrating string and other dynamics problems brought forth a mathematical study of waves. Isaac Newton studied pressure waves in 1687 which can be applied to the study of sound and light [1]. Leonhard Euler studied the vibrating ring in 1727 and was joined by Daniel Bernoulli around 1733 to study the hanging chain and linked pendulum [1]. Later work by both Euler in 1735 and Daniel Bernoulli in 1742 furthered understanding of the vibrating rod.

The study of stress waves in circular metal rods by John Hopkinson in 1872 lead his son Bertram Hopkinson to develop a ballistic pendulum method for testing the pressures produced by a bullet impact in 1913 [2]. World War II further spurred interest in the study of waves in impacted materials [3]. Percy Bridgman guided the development of impact techniques using explosive propellants in the early 1900s. These techniques were used to study how high pressure shock waves deform materials. Such situations arise when automobiles collide; micrometeoroids and debris impinge on spacecraft and aircraft; meteorites impact against planets; and earthquakes ripple through Earth [4–9].

Plate impact is a technique used to study shock impact in materials [10]. During a

plate impact experiment, an explosive charge accelerates a flyer plate to a velocity of 0.05 – 7.5 km/s towards a resting target plate (Figure 1.1). The impact of the flyer with the target generates a pressure wave that propagates within both plates. This wave is monitored within the target plate by measuring the displacement or velocity of the backside of the target as a function of time. This data can be used to infer the high-pressure properties of impacted materials.

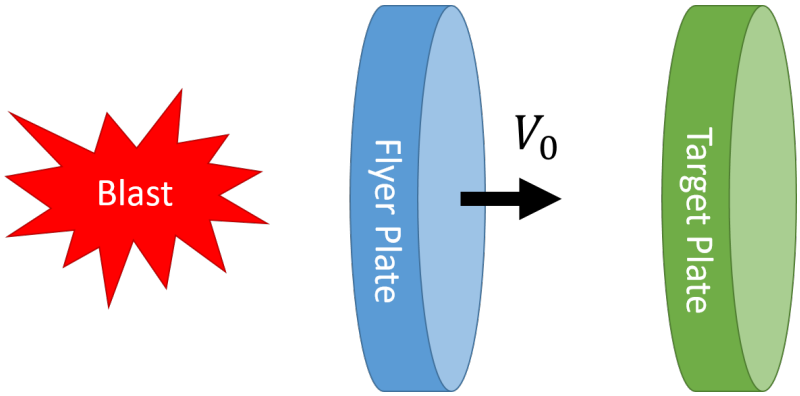

Figure 1.1: A plate impact system. During a palate impact experiment, an explosive charge accelerates a flyer plate to a velocity V_0. The flyer plate impacts against a resting target plate.

Quantifying deformation during plate impact experiments is difficult because deformations occur on a short time scale. Early measurement methods of stress, strain, and velocity are broadly categorized into contact and photography based techniques. Contact based methods include strain gauges; quartz, foil-like manganin, and polyvinylidene fluoride stress gauges; and particle velocity gauges [11]. Photography based methods include smear camera techniques and Moiré pattern analysis with high-speed cameras.

In 1965, L. M. Barker and R. E. Hollenbach at Sandia National Laboratory had the clever idea to apply interferometry — the use of interference patterns generated by mixing light waves to measure an object's displacement — to plate impact experiments [12]. The classic interferometry technique was devised by Albert Abraham Michelson during the 1887 Michelson-Morley experiments. In the 19th century, light was hypothesized to propagate through a medium called the luminiferous aether [13]. However, while it was known that other transmission mediums such as water and air interact with Earth, it was unknown if the luminiferous aether could similarly interact with Earth [14]. If the aether were capable of interacting with Earth, then Earth could drag the aether and the velocity of light would change according to

its orientation within this aether wind. The famous 1887 Michelson-Morley experiments sought to test this luminiferous aether drag hypothesis by measuring the speed of light along orthogonal directions of Earth using an array of optics (Figure 1.2) [15]. Even though these experiments did not detect changes in the speed of light, they did popularize interferometry as a method for measuring an object's displacement over time.

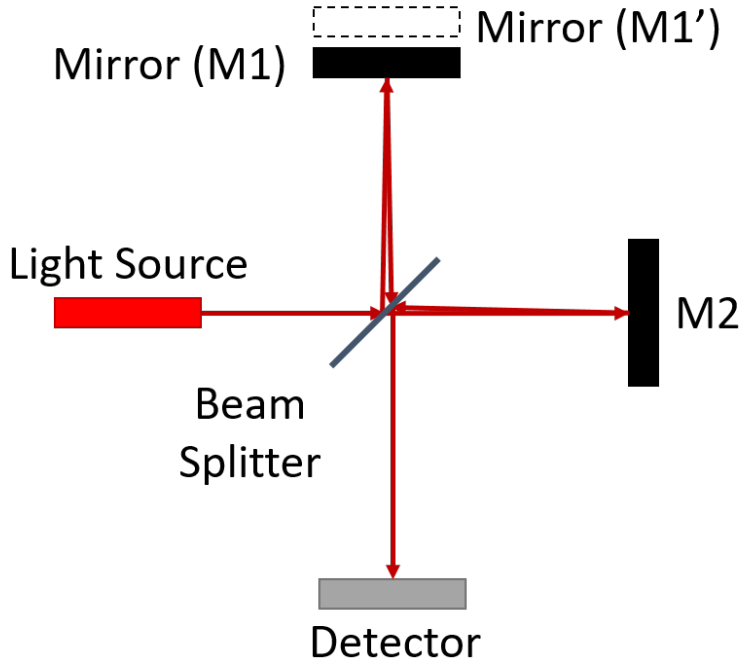

Figure 1.2: A variation of Michelson's interferometer. Light emitted by a source is split by a beam splitter. The beams travel to mirrors M1 and M2, reflect back to the beam splitter, and recombine. The interference pattern generated by the two beams is recorded by the detector. Displacing one of the mirrors, for instance M1 to M1', changes the interference pattern.

Barker and Hollenbach adapted Michelson's technique for plate impact experiments. This technique, named the normal displacement interferometer (NDI), uses the backside of the target plate as a mirror of the Michelson interferometer (Figure 1.3). This allowed the NDI to record the target's longitudinal displacement. By differentiating the target's displacement, Barker and Hollenbach found the free surface velocity of the backside of the target as a function of time.

Using the best technology available in 1965, the NDI measured velocities of up to 100 m/s with a distance resolution of 0.025 μm/fringe [12]. While these maximum velocities and resolutions are not as high as those of other techniques at the time,

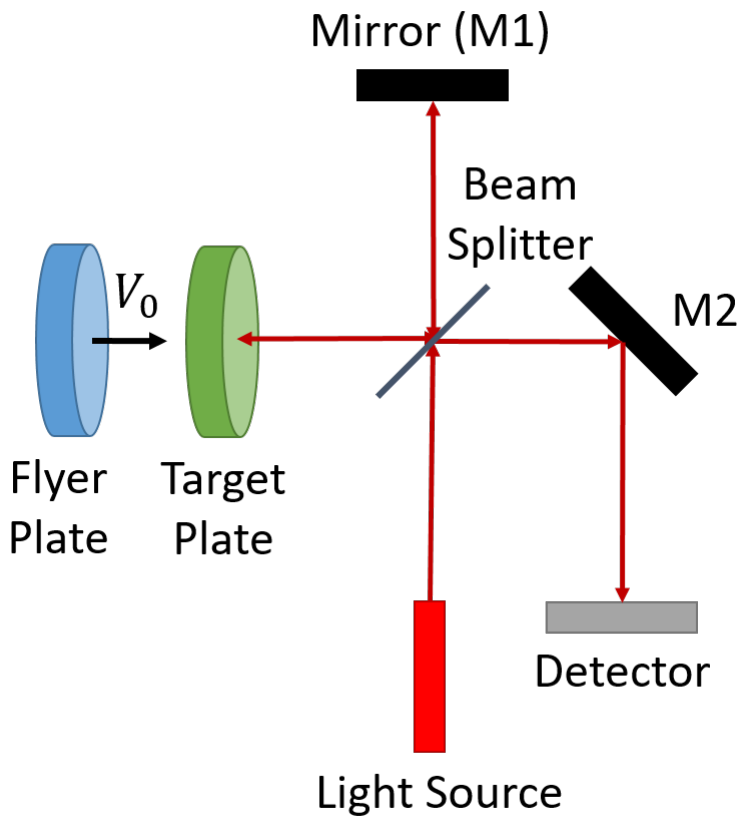

Figure 1.3: In a Normal Displacement Interferometer, the target plate serves as a mirror of the Michelson's interferometer [12].

such as smear camera techniques, the NDI technique had two main advantages over its predecessors [16]. Foremost, the NDI did not come into contact with the target surface and therefore could not alter the target's stress field [11]. Second, the NDI measured the displacement of the center point of the target, where a state of uniaxial stress remained the longest [12]. Other techniques, such as a quartz transducers, acquired data over the larger portions of the target face where a state of uniaxial stress is not assured [17].

Despite these improvements, the NDI had a major drawback. This interferometer was incapable of measuring transverse motion. Transverse motion occurs during pressure-shear plate impact experiments and during normal impact of anisotropic materials [10, 18]. Isotropic materials have properties that are constant along all directions in the material. In contrast, anisotropic materials have properties, such as strength and conductivity, that vary with direction along their crystal lattice [19]. For instance, isotropic soda-lime glass will stay the same color when rotated in plane

polarized light. However, anisotropic tourmaline displays pleochroic behavior and changes color when rotated in plane polarized light [20].

Quartz, or silicon dioxide, is an important anisotropic material with unique material properties. Throughout history, variants of silicon dioxide such as amethyst and rose quartz have been used for their beauty as gemstones [21]. Other SiO_2 variants such as flint and obsidian were historically crafted into tools, blades, and arrowheads or were used as an ignition source for fires [22, 23]. Quartz's modern value as an anisotropic material was brought to light in 1880 with Pierre and Jacques Curie's discovery of quartz's piezoelectric properties [24]. Piezoelectric materials produce an electromagnetic voltage when mechanically stressed, and are mechanically strained in the presence of an electromagnetic field. Quartz's piezoelectric properties were harnessed during World War One for submarine detection with sonar devices [25]. After the war, quartz oscillators developed in 1921 by Walter Guyton Cady found applications in clocks, microphones, speakers, and broadcasting towers [26].

Quartz's piezoelectric properties extend to the high-strain rate regime. In 1964, R. A. Graham at Sandia National Laboratory harnessed quartz's piezoelectric properties to create submicrosecond stress gauges for impact experiments [27]. Quartz's anisotropy also results in distinctive linking between longitudinal and transverse motion [28]. For instance, impacting along quartz's y-axis will induce motion along the y-axis and z-axis. Thus transverse motion is generated by the mere presence of longitudinal waves.

Measuring transverse motion during normal impact of anisotropic materials such as quartz is interesting, but fairly difficult. This motivated the development of the dynamic Moiré (shadow) technique in 1976 [29]. However, an interferometer that was capable of measuring coupled normal and transverse displacements with a higher sensitivity than Moiré technique was developed a year later.

In 1977, Kim, Clifton, and Kumar at Brown University used diffraction gratings and a modified NDI technique to measure transverse displacements in plate impact experiments [30]. Their transverse displacement interferometer (TDI) makes simultaneous, uncoupled measurements of longitudinal and transverse displacements by measuring the movement of a diffraction grating deposited onto the backside of the target (Figure 1.4). Kim, Clifton, and Kumar validated the capabilities of their NDI-TDI system with normal symmetric impact of single-crystalline y-cut α-quartz and compared their results to a theoretical framework developed by Johnson at Sandia Laboratories in 1971 [28].

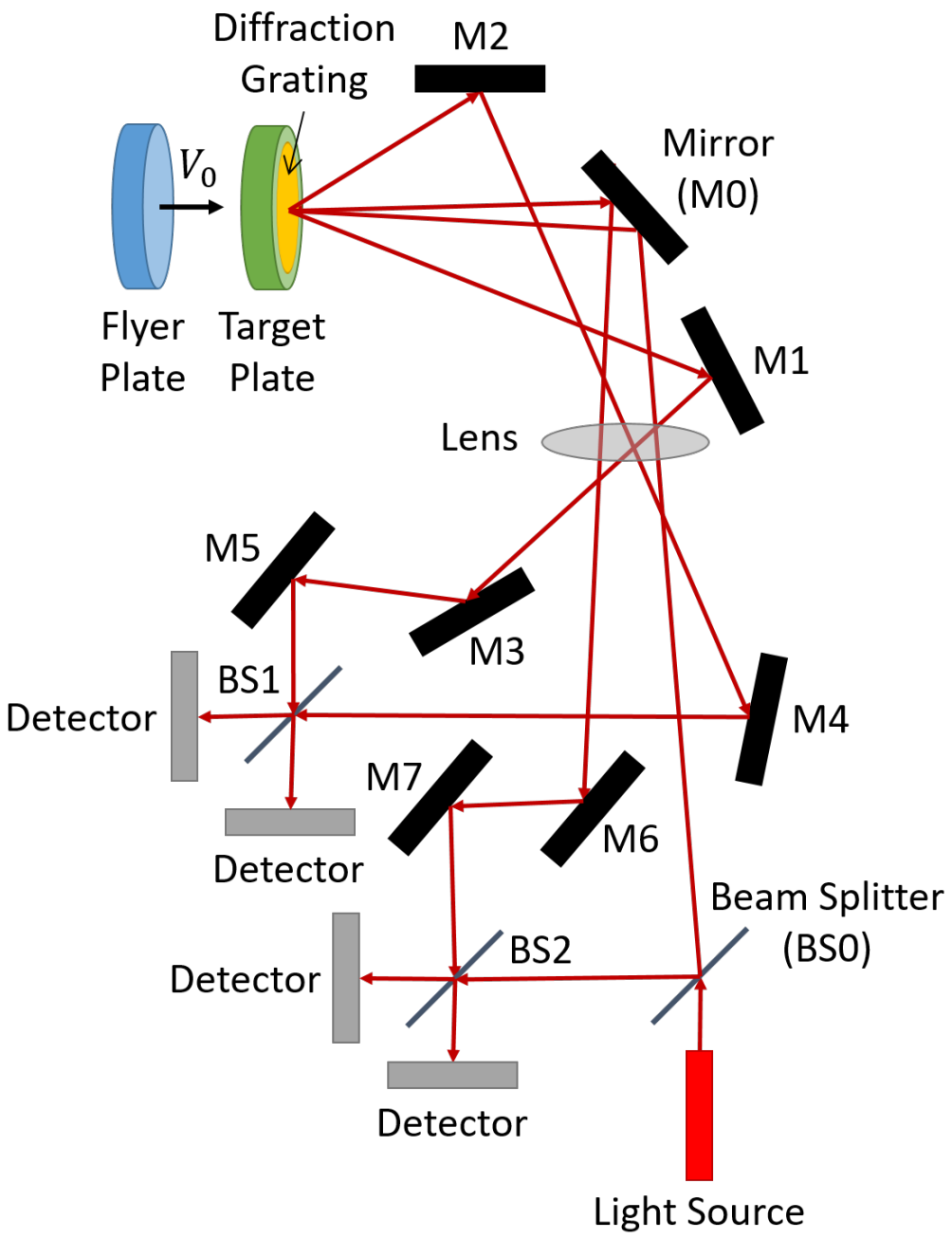

Figure 1.4: A Transverse Displacement Interferometer captures diffracted beams that contain transverse displacement information [30].

Developing a good interferometry technique for plate impact experiments is difficult because wave speeds can reach 10 km/s and experiments last only a few microseconds [31]. Early techniques were severely limited by contemporary optical technology. The maximum velocity and range of velocities that could be detected depended on

the frequency bandwidth of the interferometer's detector and oscilloscope [32].

Telecommunications technology developed in the latter half of the 20th century revolutionized the transmission of information by light waves. In 1966, researchers at Schott Glass guided light waves with bundled glass fibers [33]. This led to the development of the silica glass fiber-optic cable by researchers at Corning Glass Works in 1970 [34, 35]. Schott Glass further improved the design of fiber-optic cables in 1973 with the introduction of a quartz sheath for the quartz core (Figure 1.5) [36].

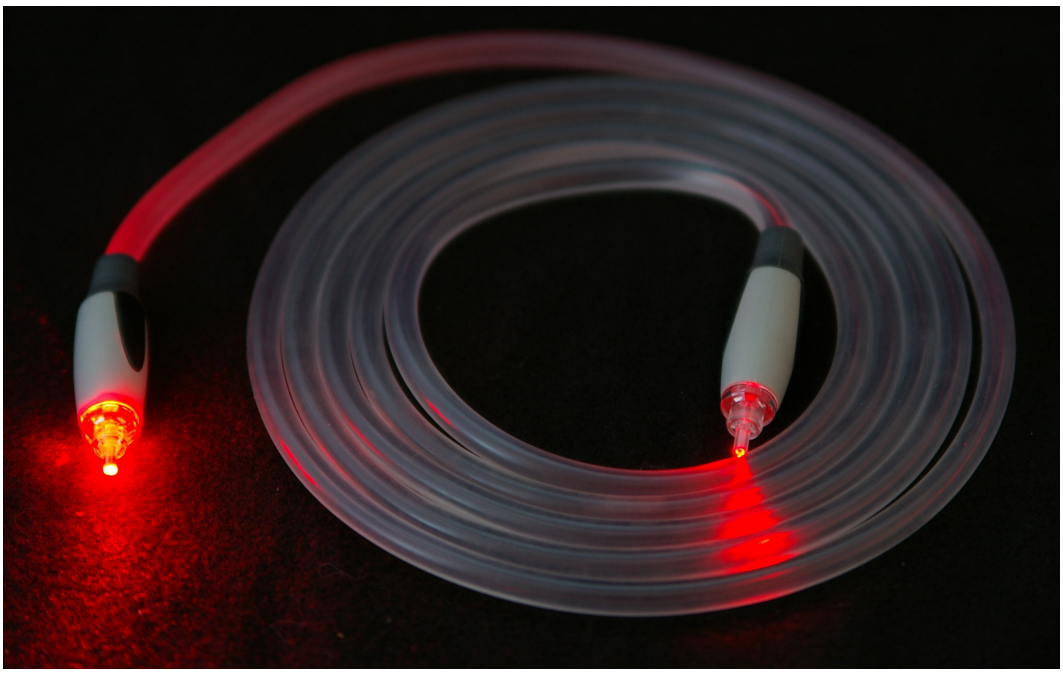

Figure 1.5: A laser on the left emits light into a fiber-optic cable. The light travels through the cable and exits on the right. Photo credit: "Fiber optic illuminated" by Hustvedt is licensed under CC BY-SA 3.0.

Interferometry techniques adapted 21st century advances in telecommunications technology. In 2004, scientists at Lawrence Livermore National Laboratory conceived a fiber-optic implementation of the NDI named the photonic Doppler velocimetry (PDV) technique [37]. PDV uses infrared light carried by fiber-optic cables to measure a target's longitudinal displacements on a nanosecond time scale [38].

The PDV technique has several advantages over its predecessors. First, because the PDV signal is frequency upshifted, PDV velocity data has better time resolution [39]. Additionally, the relatively low velocities experienced during the rise from zero

velocity to shocked velocity are better resolved with a frequency upshifted signal. Second, because the data signal is analyzed using short-time Fourier transforms, the velocity data extracted from the signal is not sensitive to the amplitude of the returning light – making the PDV less sensitive to tilt and surface roughness [39]. Third, the PDV is composed of fewer, commercially available parts than its predecessors and does not employ free-space optics such as mirrors and beam splitters. This makes the PDV simpler to implement than its predecessors.

Despite these advantages, the PDV is not a replacement for all interferometry techniques. Currently, the PDV is only capable of capturing longitudinal motion and cannot capture transverse motion like TDI. This thesis explores the development of a new system called the transverse photonic Doppler velocimetry (TPDV) technique. The TPDV technique combines the NDI-TDI's capability of monitoring longitudinal and transverse motion at a single spot on the target face with the simple fiber-optic configuration and spectral analysis techniques of the PDV system. This work validates the TPDV technique's capabilities with normal plate impact of single crystalline y-cut α-quartz against an isotropic flyer.

Development of the TPDV technique will allow scientists to more easily detect small changes in longitudinal and transverse velocity over large velocity ranges with nanosecond time scales. The TPDV will help facilitate the study of materials deforming anisotropically at high impact pressures during shock loading. This furthers our understanding of how waves interact with matter – allowing engineers to harness materials' properties to insightfully design planes, satellites, automobiles, and structures [40].

Chapter 2

THEORY

2.1 Classical Waves

Waveforms

Though we perceive differently, waves – such as mechanical water waves and acoustic waves, electromagnetic light waves, and gravitational waves – involve the transfer of energy in space and time. Some waves, such as pressure waves in materials, travel through a medium displacing particles as the wave passes by and then springing back when the wave has passed. Others, such as light waves, can travel in a vacuum causing variations in space's electric and magnetic fields.

The shape of the disturbance created by a passing wave is related to the shape's waveform[1] [41]. Waves come in many shapes, including geometric and sinusoidal varieties (Figure 2.1). For instance,

$$\psi(x,t) = A\cos(kx \mp \omega t) \tag{2.1}$$

is a common one-dimensional sinusoidal waveform. The value of the wave's disturbance ψ at a given point in space x and time t is a function of the wave's wavenumber k and angular frequency ω (Figure 2.2). Waves are generally periodic. This means that the shape of a wave repeats after one cycle. The distance traveled by the wave during one cycle is the wave's wavelength λ while the elapsed time to complete one cycle is the wave's period T.

The parameters used to describe a wave are related to one another. The wavenumber spatially describes the number of completed cycles per unit distance

$$k = \frac{2\pi}{\lambda}. \tag{2.2}$$

while the angular frequency temporally describes the number of completed cycles per unit time

$$\omega = \frac{2\pi}{T}. \tag{2.3}$$

Waves can also be described in terms of other parameters such as the phase velocity v, spatial wavenumber κ, and ordinary frequency f. The phase velocity temporally

[1] This section draws heavily on material found in [41].

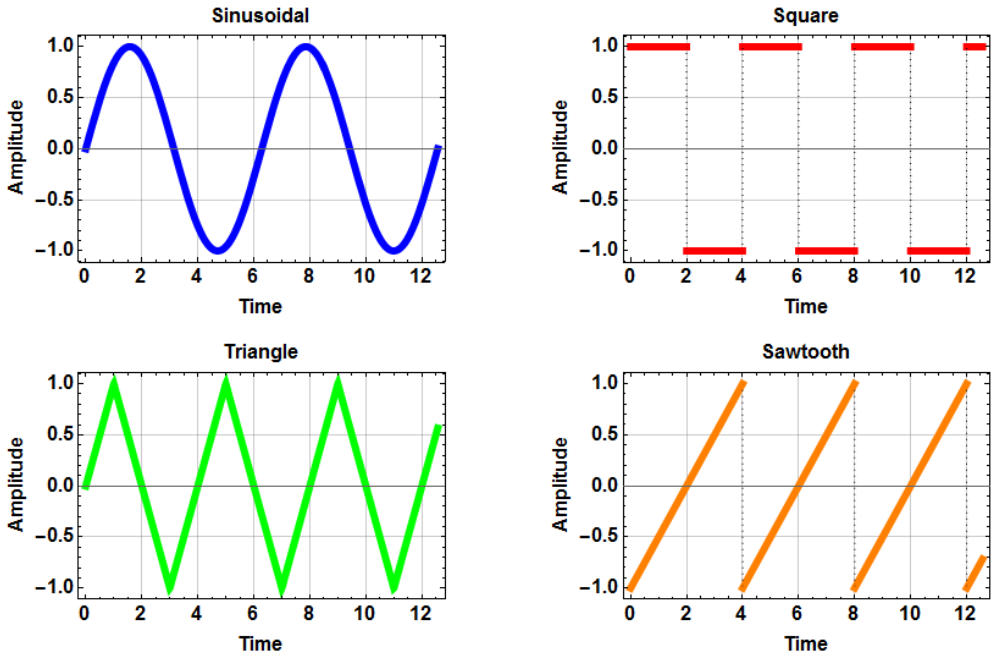

Figure 2.1: Example waveforms.

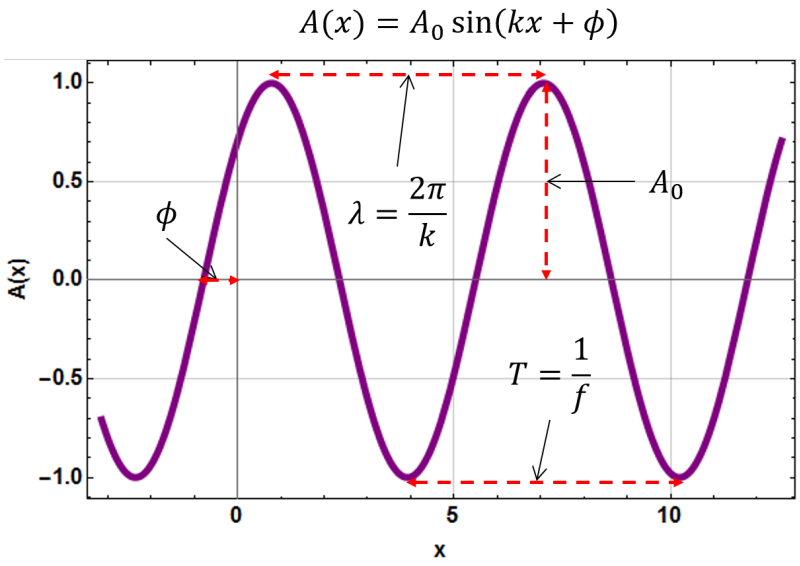

Figure 2.2: Wave parameters.

describes the distance a wave can travel in the time taken to complete one cycle

$$v = \frac{\lambda}{T} = \frac{\omega}{k}, \tag{2.4}$$

while the spatial wavenumber describes the number of completed cycles per unit

distance

$$\kappa = \frac{1}{\lambda}, \tag{2.5}$$

and the ordinary frequency temporally describes the number of completed cycles per unit time

$$f = \frac{1}{T} = \frac{\omega}{2\pi}. \tag{2.6}$$

Alternative forms of (2.1) are constructed using v and f,

$$\psi(x,t) = A\cos\left(x \mp vt\right) \tag{2.7}$$

and

$$\psi(x,t) = A\cos\left(2\pi\left(\kappa x \mp ft\right)\right). \tag{2.8}$$

A wave's phase information Φ incorporates both space and time information to represent the wave's location in it's cycle. A wave's phase can be understood in terms of a phase shift ϕ between two waves with identical wavenumbers and angular frequencies. Consider the two waves (Figure 2.3).

$$\psi_1(x,t) = A\sin\left(kx \mp \omega t\right) \tag{2.9}$$

and

$$\psi_2(x,t) = A\sin\left(kx \mp \omega t + \phi\right). \tag{2.10}$$

To observe the affect of ϕ, consider when ψ_1 and ψ_2 will each attain a value of zero at the location $x = 0$. The first wave ψ_1 will have a value of zero at $x = 0$ and $t = 0$ while the second wave ψ_2 will have a value of zero at $x = 0$ and $t = -\phi$. In effect, ϕ has delayed ψ_2, or ϕ has caused ψ_2 to lag behind ψ_1 by making ψ_2 start later in it's cycle. Thus, phase shifting controls the starting point of a wave in it's cycle.

The Wave Equation

Starting with the general wave traveling in space $\boldsymbol{x}$ and time t

$$\psi(\boldsymbol{x},t) = \mathscr{F}(\Phi) = \mathscr{F}(\boldsymbol{k}\boldsymbol{x} \mp \omega t) \tag{2.11}$$

use the chain rule to compute the first partial spatial derivatives for $i \in \{1,2,3\}$

$$\frac{\partial\psi}{\partial x_i} = \frac{\partial\mathscr{F}}{\partial x_i} = \frac{\partial\mathscr{F}}{\partial\Phi}\frac{\partial\Phi}{\partial x_i} = k_i\frac{\partial\mathscr{F}}{\partial\Phi}. \tag{2.12}$$

and using Faà di Bruno's formula to compute the second partial spatial derivatives

$$\frac{\partial^2\psi}{\partial x_i^2} = \frac{\partial^2\mathscr{F}}{\partial\Phi^2}\left(\frac{\partial\Phi}{\partial x_i}\right)^2 + \frac{\partial\mathscr{F}}{\partial\Phi}\frac{\partial^2\Phi}{\partial x_i^2} = k_i^2\frac{\partial^2\mathscr{F}}{\partial\Phi^2}. \tag{2.13}$$

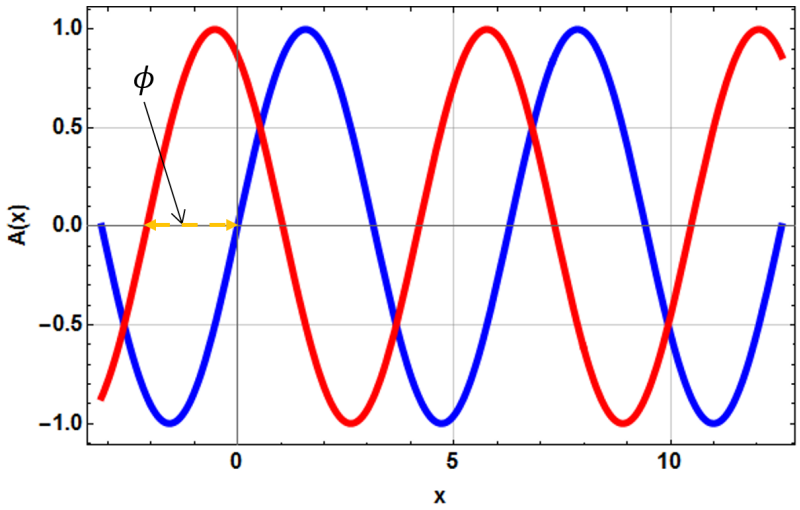

Figure 2.3: Wave $\sin(x)$ (blue) phase shifted by $2\pi/3$ to $\sin(x + 2\pi/3)$ (red).

The definition of the Laplace operator on a scalar function $\mathscr{G}$ is

$$\boldsymbol{\nabla}^2 \mathscr{G} = \frac{\partial^2 \mathscr{G}}{\partial x_j^2}. \tag{2.14}$$

Using (2.13), the Laplacian of ψ is

$$\boldsymbol{\nabla}^2 \psi = \frac{\partial^2 \psi}{\partial x_1^2} + \frac{\partial^2 \psi}{\partial x_2^2} + \frac{\partial^2 \psi}{\partial x_3^2} \tag{2.15}$$

$$= \left(k_1^2 + k_2^2 + k_3^2\right) \frac{\partial^2 \mathscr{F}}{\partial \Phi^2} \tag{2.16}$$

$$= |\boldsymbol{k}|^2 \frac{\partial^2 \mathscr{F}}{\partial \Phi^2}. \tag{2.17}$$

Noting the relationship between the wave vector $\boldsymbol{k}$ and the wavenumber k

$$k = |\boldsymbol{k}|, \tag{2.18}$$

the Laplacian of ψ becomes

$$\boldsymbol{\nabla}^2 \psi = k^2 \frac{\partial^2 \mathscr{F}}{\partial \Phi^2}. \tag{2.19}$$

Turning attention to the time dimension, the first partial temporal derivative is

$$\frac{\partial \psi}{\partial t} = \frac{\partial \mathscr{F}}{\partial t} = \frac{\partial \mathscr{F}}{\partial \Phi} \frac{\partial \Phi}{\partial t} = \mp \omega \frac{\partial \mathscr{F}}{\partial \Phi} \tag{2.20}$$

and the second partial temporal derivative is

$$\frac{\partial^2 \psi}{\partial t^2} = \frac{\partial^2 \mathscr{F}}{\partial \Phi^2} \left(\frac{\partial \Phi}{\partial t}\right)^2 + \frac{\partial \mathscr{F}}{\partial \Phi} \frac{\partial^2 \Phi}{\partial t^2} = \omega^2 \frac{\partial^2 \mathscr{F}}{\partial \Phi^2}. \tag{2.21}$$

Observing (2.19) and (2.21) respectively shows that

$$\frac{\partial^2 \mathscr{F}}{\partial \Phi^2} = \frac{1}{k^2} \boldsymbol{\nabla}^2 \psi \tag{2.22}$$

and

$$\frac{\partial^2 \mathscr{F}}{\partial \Phi^2} = \frac{1}{\omega^2} \frac{\partial^2 \psi}{\partial t^2}. \tag{2.23}$$

Combining (2.22) and (2.23)

$$\frac{1}{k^2} \boldsymbol{\nabla}^2 \psi = \frac{1}{\omega^2} \frac{\partial^2 \psi}{\partial t^2}. \tag{2.24}$$

Using relation (2.4), (2.24) becomes the three dimensional wave equation

$$\boldsymbol{\nabla}^2 \psi = \frac{1}{v^2} \frac{\partial^2 \psi}{\partial t^2}. \tag{2.25}$$

The left-side is a spatial description of the wave and the right-side is a time description of the wave. This makes the wave equation a useful tool for studying the behavior of pressure waves in materials and light waves in electromagnetic fields.

Plane Waves

A subset of waves satisfying the wave equation (2.25) are called plane waves. Plane waves propagate in a series of parallel planes called wavefronts (Figure 2.4). The normals to the planes $\boldsymbol{n}$ are parallel to the wave's propagation direction, or wave vector, $\boldsymbol{k}$. These planes extend infinitely in the two spatial directions perpendicular to $\boldsymbol{k}$ and ψ has a constant value on each plane. In an orthonormal basis, this imposes the condition that any two points $\boldsymbol{r}_0$ and $\boldsymbol{r}_1$ on a single plane must form a vector perpendicular to $\boldsymbol{k}$ and must produce the same value of ψ. Mathematically, this is expressed as

$$(\boldsymbol{r}_1 - \boldsymbol{r}_0) \cdot \boldsymbol{k} = 0. \tag{2.26}$$

Distributing (2.26)

$$\boldsymbol{r}_1 \cdot \boldsymbol{k} - \boldsymbol{r}_0 \cdot \boldsymbol{k} = 0 \tag{2.27}$$

and varying $\boldsymbol{r}_1$ while holding $\boldsymbol{r}_0$ constant shows that

$$\boldsymbol{r}_1 \cdot \boldsymbol{k} = \boldsymbol{r}_0 \cdot \boldsymbol{k}. \tag{2.28}$$

Generalizing $\boldsymbol{r}_1$ to any point $\boldsymbol{r}$ on the plane, (2.28) shows that for any given t, a plane wave satisfies

$$\boldsymbol{r} \cdot \boldsymbol{k} = \text{constant} \tag{2.29}$$

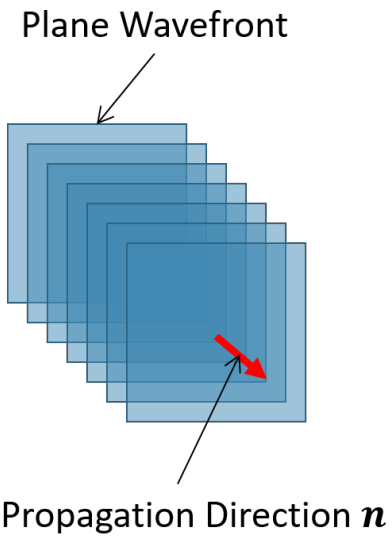

Figure 2.4: Plane wave (blue) propagating in the direction $\boldsymbol{n}$ (red).

and has the general form

$$\psi(\boldsymbol{r}, t) = \mathscr{F}\left(\boldsymbol{k} \cdot \boldsymbol{r} \mp \omega t + \phi\right). \tag{2.30}$$

A common plane wave equation satisfying (2.29) is

$$\psi(\boldsymbol{r}, t) = Ae^{(i(\boldsymbol{k}\cdot\boldsymbol{r}\mp\omega t+\phi))} \tag{2.31}$$

Upon application of Euler's fomula

$$e^{(i\theta)} = \cos(\theta) + i\sin(\theta) \tag{2.32}$$

yields the real and imaginary components of (2.31)

$$\mathrm{Re}\left[\psi(\boldsymbol{r}, t)\right] = A\cos\left(\boldsymbol{k} \cdot \boldsymbol{r} \mp \omega t + \phi\right) \tag{2.33}$$

and

$$\mathrm{Im}\left[\psi(\boldsymbol{r}, t)\right] = A\sin\left(\boldsymbol{k} \cdot \boldsymbol{r} \mp \omega t + \phi\right) \tag{2.34}$$

which are commonly seen in physics and engineering applications.

2.2 Plate Impact: Elastic Waves and Materials

Plate Impact System

During a plate impact experiment, an explosive charge accelerates a flyer plate to a velocity V_0 between 0.05 – 7.5 km/s towards a stationary target plate[2] (Figure 2.5) [28, 39]. The impact of the flyer with the target generates a pressure wave that propagates within both plates. These waves will travel through the materials, altering the material's particle velocity and stress state. This wave is monitored within the target plate by measuring the displacement or velocity of the backside of the target plate as a function of time. This data can be used to infer the material's behavior during high-pressure impact.

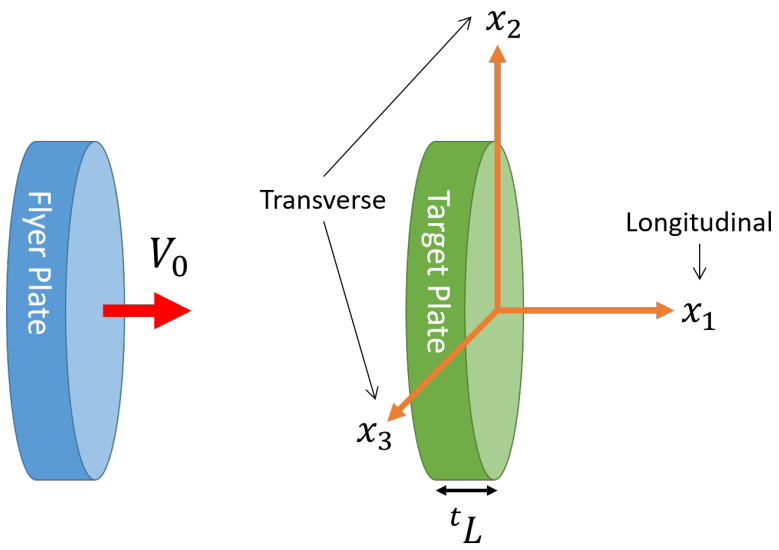

Figure 2.5: Normal impact system.

Plate impact experiments can be categorized in several ways. First, experiments can be classified by the type of impact. During normal impact experiments, the flyer plate only has a normal velocity component relative to the target plate. During pressure-shear impact experiments, the flyer plate has a normal and transverse velocity component relative to the target plate. Second, experiments can be classified by the plate of interest. During a classical plate impact experiment, the target plate is the material of interest. In a reverse ballistic plate impact experiment, the flyer plate is the material of interest. Third, experiments can be further classified by symmetry. Symmetric experiments have flyer and target plates made of the same material and they are impacted along the same crystal orientation for crystalline materials.

[2]This section draws heavily on material found in [28] and [39].

The particle velocity and stress state in the flyer and target plates can be derived using linear elasticity and by applying the proper boundary conditions.

Elastic Waves

As an elastic wave travels in a material, it displaces planes of atoms which spring back into position after the wave has passed. If the planes of atoms are forced closer together, then the wave is compressive. If the planes of atoms are forced apart, then the wave is tensile (Figure 2.6).

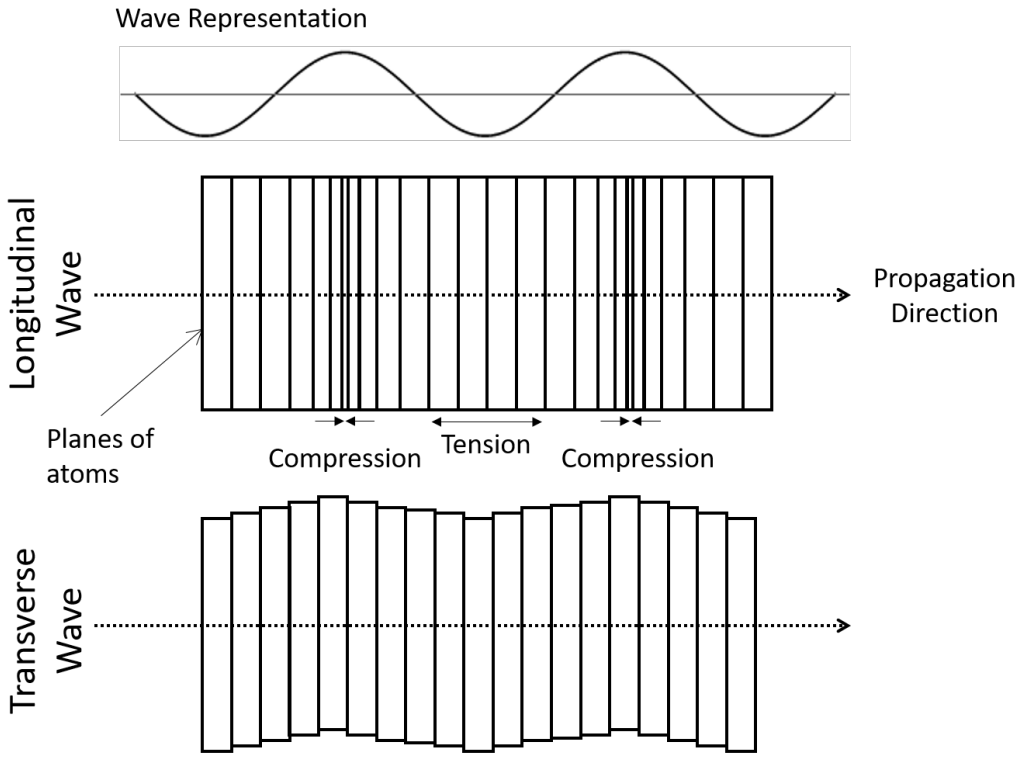

Figure 2.6: Compression and tensile longitudinal waves and transverse waves in a material.

Elastic waves are plane waves in materials[3] [28]. These mechanical waves are described by a variant of the wave equation (2.25) that can be derived from a linear momentum balance in terms of displacements. This wave equation

$$\rho \frac{\partial^2 u_i}{\partial t^2} = C_{ijkl} \frac{\partial^2 u_k}{\partial x_j \partial x_l} \tag{2.35}$$

describes the displacement u_i of an infinite linear elastic material in space x_i and time t according the material's density ρ and elastic-constant tensor C_{ijkl}. The

[3]This section draws heavily on material found in [28].

elastic-constant tensor contains information about the symmetry of the material.

A waveform solution to (2.35) traveling in a direction parallel to the unit vector a_m can be formed as

$$u_i = U_i \mathscr{F}(\Phi) = U_i \mathscr{F}\left(t - a_m \frac{x_m}{v}\right). \tag{2.36}$$

This waveform states that the material's displacement u_i for a given propagation direction a_m in a given direction x_m is a function $\mathscr{F}$ of the wave's velocity v scaled by a relative-displacement amplitude, or wave polarization, U_i. The polarization U_i describes the displacement direction relative to the propagation direction (Figure 2.6). If the displacement direction is parallel to the propagation direction, then the wave is longitudinal. If the displacement direction is perpendicular to the propagation direction, then the wave is transverse. Waves with polarizations for the continuum of cases in-between are called quasi-longitudinal or quasi-transverse depending on their dominant character.

To solve for the velocities of these waves and their polarizations, take the first and second spatial and temporal partial derivatives of (2.36) and insert into (2.35). The result is

$$\left(C_{ijkl} a_l a_j - \rho v^2 \delta_{ik}\right) U_k = 0. \tag{2.37}$$

Defining the acoustic tensor Γ_{ik}

$$\Gamma_{ik} = C_{ijkl} a_j a_l \tag{2.38}$$

to describe the interaction between the material and the direction of wave propagation shows that (2.37) is an eigensystem

$$\Gamma_{ik} U_k = \rho v^2 \delta_{ik} U_k \tag{2.39}$$

relating the velocities and directions of waves along a given direction in the material.

The eigensystem (2.39) is solved by observing that

$$\left(\Gamma_{ik} - \rho v^2 \delta_{ik}\right) U_k = 0 \tag{2.40}$$

for eigenvalues

$$\Lambda = \rho v^2 \tag{2.41}$$

found from the characteristic equation

$$\det\left(\Gamma_{ik} - \Lambda \delta_{ik}\right) = 0. \tag{2.42}$$

Each eigenvalue Λ corresponds to an eigenvector U_k. Since a square matrix of size n has at most n distinct eigenvalues, (2.39) shows that there are at most three waves generated in a material upon impact. Additionally, because Γ_{ik} is Hermitian, it's eigenvectors are orthogonal. This means that one generated wave is longitudinal or quasi-longitudinal, and two generated waves are transverse or quasi-transverse.

Analysis of Normal Impact

Coordinate System The flyer and target plates' eigenvectors ${}^{f}\boldsymbol{U}^{(i)}$ and ${}^{t}\boldsymbol{U}^{(i)}$ from (2.39) are used to solve the normal impact system. The flyer and target plates' respective impact directions ${}^{f}a$ and ${}^{t}a$, and material constants ${}^{f}\boldsymbol{C}$ and ${}^{t}\boldsymbol{C}$, are defined in each plate's crystalline coordinate systems ${}^{f}\boldsymbol{e}$ and ${}^{t}\boldsymbol{e}$. These two crystalline coordinate systems do not necessarily coincide with one another, nor do they necessarily coincide with the impact coordinate system ${}^{I}\boldsymbol{e}$. Therefore, the flyer and target plates' eigenvectors need to be rotated from their crystalline coordinate systems into in the impact coordinate system using a rotation matrix.

A general coordinate transformation matrix $\boldsymbol{Q}$ from coordinate system $\boldsymbol{e}$ to $\boldsymbol{e}^{\star}$ is given by

$$Q_{kl} = e_k \cdot e_l^{\star} \tag{2.43}$$

where $e_k^{\star}$ are the basis vectors in the crystal and e_l are the basis vectors in the impact system. Thus vectors $\boldsymbol{w}$ in $\boldsymbol{e}$ are mapped to $\boldsymbol{e}^{\star}$ by

$$w_k^{\star} = Q_{kl} w_l. \tag{2.44}$$

and tensors $\boldsymbol{W}$ are mapped to $\boldsymbol{e}^{\star}$ by

$$W_{kl}^{\star} = Q_{kj} Q_{lp} W_{jp}. \tag{2.45}$$

Both the flyer and target plates have a respective rotation matrix ${}^{f}\boldsymbol{Q}$ and ${}^{t}\boldsymbol{Q}$ relating their quantities in their crystal system to the target system.

Displacement, Strain, and Stress The displacements of a semi-infinite flyer plate f ($x_1 \leq 0$) and a semi-infinite target plate t ($x_1 \geq 0$) as a function of location x_1 and time $\tau < \tau_s$ where τ_s is the separation time are

$${}^{f}\boldsymbol{u}(x_1, \tau) = \sum_{i=1}^{3} \alpha_i \, {}^{f}\boldsymbol{U}^{(i)} h\left(\tau + \frac{x_1}{{}^{f}v_i}\right) + \begin{bmatrix} V_0 \tau \\ 0 \\ 0 \end{bmatrix} \tag{2.46}$$

$$ {}^{t}\boldsymbol{u}\left(x_1,\tau\right)=\sum_{i=1}^{3}\beta_i\,{}^{t}\boldsymbol{U}^{(i)}h\left(\tau-\frac{x_1}{{}^{t}v_i}\right) \tag{2.47} $$

where

$$ h\left(\theta\right)=\int_{-\infty}^{\theta}H(z)\mathrm{d}z. \tag{2.48} $$

The coefficients α_i and β_i are fitting constants, ${}^{f}\boldsymbol{U}^{(i)}$ and ${}^{t}\boldsymbol{U}^{(i)}$ are the flyer and target plates' respective i^{th} eigenvectors in the impact coordinate system ${}^{I}\boldsymbol{e}$, and $H(z)$ is the unit step function. The function $h\left(\theta\right)$ has a value $h\left(\theta\right)=0$ for $\theta<0$ and $h\left(\theta\right)=\theta$ for $\theta\geq 0$. Physically, $h\left(\theta\right)$ ensures that the i^{th} wave does not displace material at x_1 prior to its arrival.

The strains in the flyer and target plates are derived from small strain theory. This assumes that the geometry of the deforming body is not changed by the tiny displacements in the material, and by extension, that the body is not plastically deforming. The infinitesimal strain tensor $\boldsymbol{\epsilon}$ is found from the displacements

$$ \epsilon_{ij}=\frac{1}{2}\left(\frac{\partial u_i}{\partial x_j}+\frac{\partial u_j}{\partial x_i}\right) \tag{2.49} $$

and the stress tensor $\boldsymbol{\sigma}$ is found from Hooke's law

$$ \sigma_{ij}=C_{ijkl}\epsilon_{kl}. \tag{2.50} $$

From conservation of angular momentum

$$ \sigma_{ij}=\sigma_{ji}. \tag{2.51} $$

Using this symmetry, the strains, stresses, and elastic-constant tensor can be written in condensed (Voigt) notation. Focusing only on deformation in the x_1 direction, the condensed form of (2.50) is

$$ \boldsymbol{\varepsilon}=\begin{bmatrix}\epsilon_{11}\\ 2\epsilon_{12}\\ 2\epsilon_{13}\end{bmatrix} \tag{2.52} $$

$$ \boldsymbol{s}=\begin{bmatrix}\sigma_{11}\\ \sigma_{12}\\ \sigma_{13}\end{bmatrix} \tag{2.53} $$

$$ \boldsymbol{\zeta}=\begin{bmatrix}C_{11} & C_{16} & C_{15}\\ C_{16} & C_{66} & C_{56}\\ C_{15} & C_{56} & C_{55}\end{bmatrix} \tag{2.54} $$

$$s_k = \zeta_{kl}\varepsilon_l. \tag{2.55}$$

Applying (2.46) and (2.47) to (2.49) and (2.52) yields the strain

$$\boldsymbol{\varepsilon}(x_1,\tau) = \begin{bmatrix}\epsilon_{11}\\ 2\epsilon_{12}\\ 2\epsilon_{13}\end{bmatrix} = \begin{bmatrix}\frac{1}{2}\left(\frac{\partial u_1}{\partial x_1}+\frac{\partial u_1}{\partial x_1}\right)\\ 2\left(\frac{1}{2}\left(\frac{\partial u_1}{\partial x_2}+\frac{\partial u_2}{\partial x_1}\right)\right)\\ 2\left(\frac{1}{2}\left(\frac{\partial u_1}{\partial x_3}+\frac{\partial u_3}{\partial x_1}\right)\right)\end{bmatrix} = \begin{bmatrix}\frac{\partial u_1}{\partial x_1}\\ \frac{\partial u_1}{\partial x_2}+\frac{\partial u_2}{\partial x_1}\\ \frac{\partial u_1}{\partial x_3}+\frac{\partial u_3}{\partial x_1}\end{bmatrix}. \tag{2.56}$$

This makes the m^{th} entry in ${}^f\boldsymbol{\varepsilon}$ and ${}^t\boldsymbol{\varepsilon}$

$${}^f\varepsilon_m(x_1,\tau) = -\sum_{i=1}^{3}\left(\frac{\alpha_i}{{}^fv_i}\right){}^fU_m^{(i)}H\left(\tau+\frac{x_1}{{}^fv_i}\right) \tag{2.57}$$

$${}^t\varepsilon_m(x_1,\tau) = \sum_{i=1}^{3}\left(\frac{\beta_i}{{}^tv_i}\right){}^tU_m^{(i)}H\left(\tau-\frac{x_1}{{}^tv_i}\right) \tag{2.58}$$

where $U_m^{(i)}$ represents the m^{th} entry the i^{th} eigenvector. The stress in the flyer plate ${}^f\boldsymbol{s}$ and target plate ${}^t\boldsymbol{s}$ are then calculated through (2.55).

Boundary Conditions Stress and displacement boundary conditions restrict the values of $\boldsymbol{\alpha}$ and $\boldsymbol{\beta}$.

Newton's third law states that forces arise in equal but opposite pairs. This means that stress is equal in magnitude and opposite in direction on both sides of the impact interface

$${}^f\boldsymbol{s}(x_1=0,\tau) = -{}^t\boldsymbol{s}(x_1=0,\tau). \tag{2.59}$$

The magnitude of the shear stresses depends on the friction coefficient between the two interfaces, which is loosely proportional to the surfaces' roughnesses [42]. Rough interfaces usually transmit higher amounts of shear stress than smooth surfaces. Modeling shear stress as proportional to the difference in the flyer and target plates' velocities, the extent of shear stress transmission can be controlled using

$${}^f\sigma_{12}(x_1=0,\tau) = \eta\left({}^f\dot{u}_2 - {}^t\dot{u}_2\right) \tag{2.60}$$

$${}^f\sigma_{13}(x_1=0,\tau) = \eta\left({}^f\dot{u}_3 - {}^t\dot{u}_3\right) \tag{2.61}$$

where η is a constant and $\dot{\boldsymbol{u}}$ is the partial time derivative of displacement

$$\dot{\boldsymbol{u}} = \frac{\partial \boldsymbol{u}}{\partial \tau}. \tag{2.62}$$

The case $\eta = 0$ represents zero shear-stress transmission across the interface while the case $1/\eta = 0$ represents displacement continuity (${}^f\dot{u}_2 = {}^t\dot{u}_2$ and ${}^f\dot{u}_3 = {}^t\dot{u}_3$).

Additionally, continuity of the displacements at the impact interface ensures that the flyer and target plates remain in contact

$$ {}^f u_1(x_1 = 0, \tau) = {}^t u_1(x_1 = 0, \tau). \tag{2.63} $$

Thus, the system of equations

$$ \begin{cases} {}^f \boldsymbol{s}(x_1 = 0, \tau) + {}^t \boldsymbol{s}(x_1 = 0, \tau) = 0 \\ {}^f u_1(x_1 = 0, \tau) - {}^t u_1(x_1 = 0, \tau) = 0 \end{cases} \tag{2.64} $$

can be solved for the set of six coefficients $\{\alpha_1, \alpha_2, \alpha_3, \beta_1, \beta_2, \beta_3\}$. Substituting $\boldsymbol{\alpha}$ and $\boldsymbol{\beta}$ into (2.46), (2.47), (2.57), (2.58) and (2.55) yields a description of the deformation of the flyer-target plate system.

Free-Surface Velocity The free-surface velocity of the target plate is found by introducing a finite target plate thickness ${}^tL$. When the waves generated at the interface reach the surface at $x_1 = {}^tL$, the surface will displace. The velocity of the moving surface $\boldsymbol{V}_{\text{free}}$ is related to the velocity of the particles $\boldsymbol{U}_p$ by [10]

$$ \boldsymbol{U}_p = \frac{1}{2}\boldsymbol{V}_{\text{free}}. \tag{2.65} $$

The particle velocity is found by differentiating displacement with respect to time

$$ \boldsymbol{U}_p = \frac{\partial\, {}^t\boldsymbol{u}}{\partial \tau}. \tag{2.66} $$

Applying (2.47), the particle velocity is

$$ {}^t\boldsymbol{U_p}\,(x_1, \tau) = \sum_{i=1}^{3} \beta_i\, {}^t\boldsymbol{U}^{(i)} H\left(\tau - \frac{x_1}{{}^t v_i}\right) \tag{2.67} $$

and from (2.65) the free surface velocity of the target plate is

$$ {}^t\boldsymbol{V}_{\text{free}}(\tau) = 2\sum_{i=1}^{3} \beta_i\, {}^t\boldsymbol{U}^{(i)} H\left(\tau - \frac{{}^tL}{{}^t v_i}\right). \tag{2.68} $$

Normal Impact of Isotropic Flyer and Trigonal Target

Select trigonal materials, such as single crystalline y-cut α-quartz, exhibit strong deformation anisotropy (Figure 2.7). This means that some trigonal materials can exhibit transverse motion when impacted normally with an isotropic flyer material such as glass. For instance, impacting along the y-axis of a trigonal target plate

$$ {}^{t}\boldsymbol{a} = \begin{bmatrix} 0 \\ 1 \\ 0 \end{bmatrix} \tag{2.69} $$

can induce motion along [001].

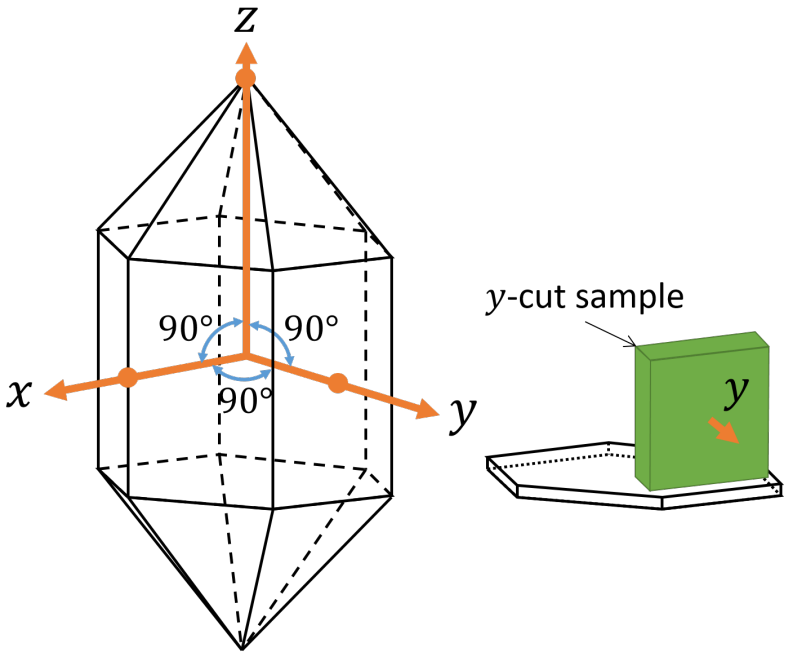

Figure 2.7: Trigonal α-quartz crystal axes (left) and y-cut α-quartz sample (right). The large surface of the y-cut sample has a normal parallel to the crystal's y-axis.

Since the flyer plate is isotropic, the $\langle 100 \rangle$ family of and the directions [100], [010], and [001] are symmetrically equivalent (Figure 2.8). This means that impacting along [100] is equivalent to impacting along [010]. For simplicity, the direction of impact of the flyer plate is taken to be

$$ {}^{f}\boldsymbol{a} = \begin{bmatrix} 0 \\ 1 \\ 0 \end{bmatrix}. \tag{2.70} $$

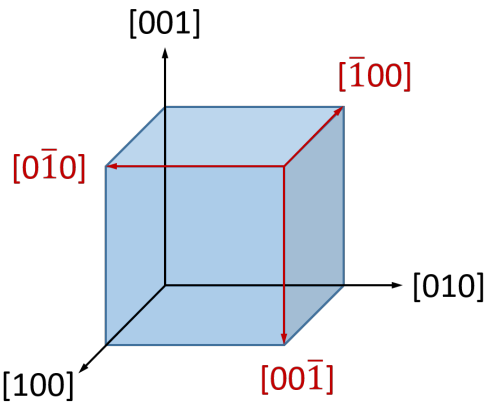

Figure 2.8: Isotropic lattice directions.

Given this set-up, the initial velocity of the flyer plate is

$$ {}^{f}\boldsymbol{V}_0 = \begin{bmatrix} 0 \\ V_0 \\ 0 \end{bmatrix}. \tag{2.71} $$

Next, the elastic constant tensor for a material with 32-point-group trigonal symmetry in Voigt notation is

$$ {}^{t}\boldsymbol{C} = \begin{bmatrix} C_{11} & C_{12} & C_{13} & C_{14} & 0 & 0 \\ C_{12} & C_{22} & C_{23} & C_{24} & 0 & 0 \\ C_{13} & C_{23} & C_{33} & 0 & 0 & 0 \\ C_{14} & C_{24} & 0 & C_{44} & 0 & 0 \\ 0 & 0 & 0 & 0 & C_{55} & C_{56} \\ 0 & 0 & 0 & 0 & C_{56} & C_{66} \end{bmatrix} \tag{2.72} $$

where the elastic constants $\{C_{11}, C_{12}, C_{13}, C_{14}, C_{22}, C_{23}, C_{24}, C_{33}, C_{44}, C_{55}, C_{56}, C_{66}\}$ are specific to the material [43]. The elastic constant tensor for an isotropic material is

$$ {}^{f}\boldsymbol{C} = \frac{E}{(1+\nu)(1-2\nu)} \begin{bmatrix} 1-\nu & \nu & \nu & 0 & 0 & 0 \\ \nu & 1-\nu & \nu & 0 & 0 & 0 \\ \nu & \nu & 1-\nu & 0 & 0 & 0 \\ 0 & 0 & 0 & \frac{1-2\nu}{2} & 0 & 0 \\ 0 & 0 & 0 & 0 & \frac{1-2\nu}{2} & 0 \\ 0 & 0 & 0 & 0 & 0 & \frac{1-2\nu}{2} \end{bmatrix} \tag{2.73} $$

where the elastic constant E is the material's Young's modulus and parameter ν is the material's Poisson's ratio.

The acoustic tensor (2.38) for the trigonal target plate impacted along [010] is

$$ {}^{t}\mathbf{\Gamma} = \begin{bmatrix} C_{66} & 0 & 0 \\ 0 & C_{22} & C_{24} \\ 0 & C_{24} & C_{44} \end{bmatrix} \tag{2.74} $$

and the acoustic tensor for the isotropic flyer plate impacted along [010] is

$$ {}^{f}\mathbf{\Gamma} = \begin{bmatrix} \frac{E}{2(\nu+1)} & 0 & 0 \\ 0 & \frac{E(1-\nu)}{(1-2\nu)(\nu+1)} & 0 \\ 0 & 0 & \frac{E}{2(\nu+1)} \end{bmatrix} \tag{2.75} $$

Allowing the following dummy variables

$$ \xi = \frac{-C_{22} + C_{44} + \sqrt{C_{22}^2 - 2C_{44}C_{22} + 4C_{24}^2 + C_{44}^2}}{2C_{24}} \tag{2.76} $$

and

$$ K = \sqrt{C_{22}^2 + 4C_{24}^2 - 2C_{22}C_{44} + C_{44}^2} \tag{2.77} $$

the eigensystem (2.40) of ${}^{t}\Gamma$ for the trigonal target plate is found

$$ \begin{array}{ll} {}^{t}\rho\,{}^{t}v_i^2 & {}^{t}\boldsymbol{U}^{(i)} \\ \hline \frac{1}{2}\left(C_{22} + C_{44} - K\right) & \{0, -\xi, 1\} \\ \frac{1}{2}\left(C_{22} + C_{44} + K\right) & \{0, 1, \xi\} \\ C_{66} & \{1, 0, 0\} \end{array} . \tag{2.78} $$

Allowing the following dummy variable

$$ \kappa = \frac{E}{2(\nu + 1)} \tag{2.79} $$

the eigensystem of ${}^{f}\Gamma$ for the isotropic flyer plate is

$$ \begin{array}{ll} {}^{f}\rho\,{}^{f}v_i^2 & {}^{f}\boldsymbol{U}^{(i)} \\ \hline 2\kappa(\nu-1)/2\nu-1 & \{0, 1, 0\} \\ \kappa & \{0, 0, 1\} \\ \kappa & \{1, 0, 0\} \end{array} . \tag{2.80} $$

The isotropic flyer and trigonal target plates' wavespeeds and polarization directions from (2.78) and (2.80) are used to solve for the free surface velocity of the backside of the trigonal target plate (Section 2.2).

2.3 Interferometry: Electromagnetic Waves and Light

Photonic Doppler Velocimetry System

The photonic Doppler velocimetry (PDV) and transverse photonic Doppler velocimetry (TPDV) systems use interference patterns generated by interfering beams of light to detect the displacement of moving surfaces[4]. In the case of plate impact, the moving surface is the backside of the target plate [39, 41, 44].

A PDV-TPDV system consists of a series of fiber-optic cables and probes that are linked to a light source, photodetector, and oscilloscope (Figure 2.9). A laser emits light into a fiber-optic cable which carries the light to a PDV probe. The PDV probe focuses the light and beams the light onto a diffraction grating deposited on the backside of the target. The target's displacement changes the light's phase and encodes it with the target's displacement information.

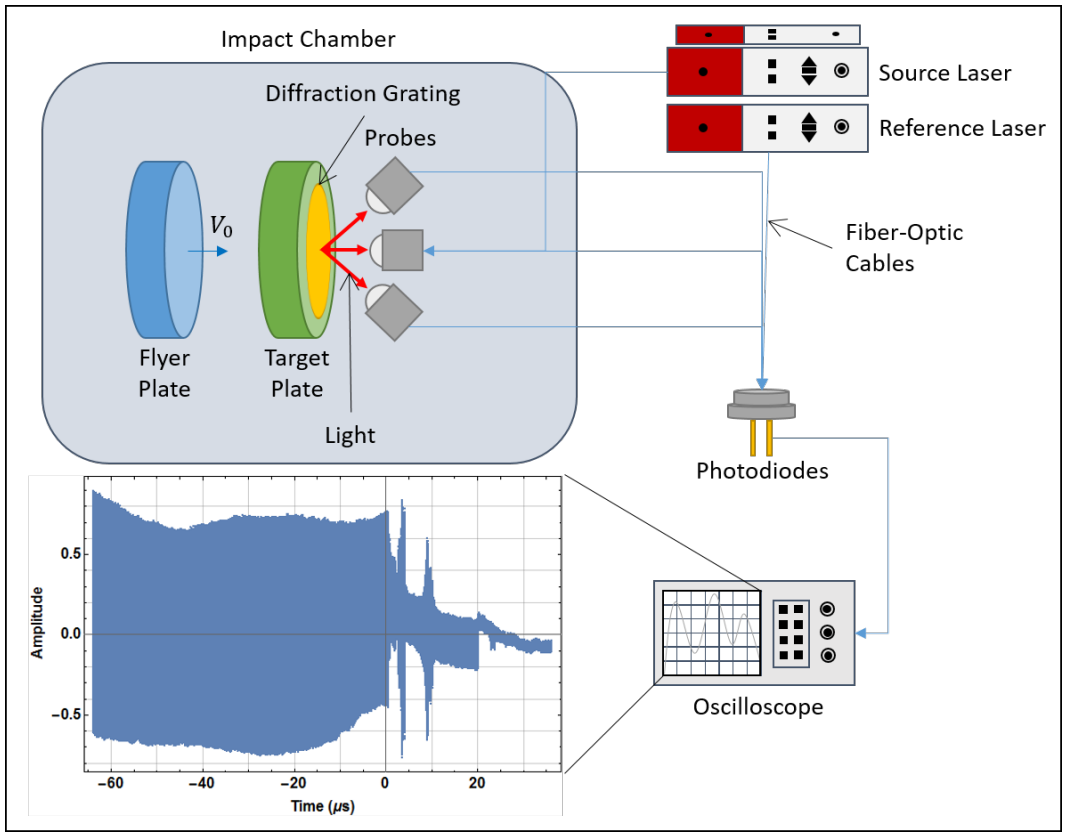

Figure 2.9: Simplified PDV-TPDV system.

Three probes collect the light that reflects and diffracts from the diffraction grating. The PDV probe re-captures the light reflecting normally. Two other probes capture

[4]This section draws heavily on material found in [41], [39], and [44].

the light diffracting at angles $\pm\theta$ from the target's surface normal. The probes funnel the returning light through separate fiber-optic cables. Each beam travels along its respective fiber-optic cable and combines with an equal portion of reference light. The reference light has a different wavelength than the source light and is generated with a separate laser. The combined target-reference light feeds into a photodetector. A digitizer, or digital oscilloscope, turns the photodetector's analog voltage signal into a digital signal. The oscilloscope records the signals' intensities as a function of time.

The PDV probe capturing light normal to the target's surface contains information about the target's longitudinal motion. The TPDV probes capturing light diffracting from the target's surface contain information about the target's transverse motion. At least two of the three probes must function to determine the target's motion in three dimensions. If only longitudinal displacement information is needed, then the PDV-TPDV system can be implemented with one normal PDV probe and a diffraction grating does not need to be deposited on the back of the target.

Electromagnetic Plane Waves

Light is an electromagnetic plane wave described by a variant of the wave equation (2.25) that is derived from Maxwell's equations

$$\frac{\partial^2 \boldsymbol{E}}{\partial t^2} = c_0^2 \nabla^2 \boldsymbol{E}. \tag{2.81}$$

This wave equation describes the variation in the electric field E in space $\boldsymbol{r}$ and time t according to the speed of light c_0. A solution to (2.81) is the plane wave equation

$$\boldsymbol{E} = \boldsymbol{E_0} \exp\left[i\left(\boldsymbol{k}\cdot\boldsymbol{r} - \omega t + \phi\right)\right]. \tag{2.82}$$

The plane wave equation for light describes how the light's electric field $\boldsymbol{E}$ varies with space in terms of its propagation (wave) vector $\boldsymbol{k}$ and how the light's electric field varies with time in terms of its angular frequency ω. The phase constant ϕ describes the wave's starting position and $\boldsymbol{E_0}$ is the field's amplitude.

Analysis of Interferometry

Optical Path Length As light of wavelength λ_0 travels a distance s between points a and b through a medium with a continuously varying refractive index $n(s)$, it covers a distance equal to its optical path length (OPL)

$$OPL = \int_a^b n(s)\mathrm{d}s \tag{2.83}$$

and accumulates an optical phase ϕ

$$\phi = \frac{2\pi}{\lambda_0} \int_a^b n(s)\mathrm{d}s. \tag{2.84}$$

The light's accumulated phase is proportional to the number of cycles completed by the light while traveling the distance equal to its OPL (Figure 2.10). In a vacuum environment $n = 1$, and light accumulates a phase

$$\phi = \frac{2\pi}{\lambda_0} (b - a). \tag{2.85}$$

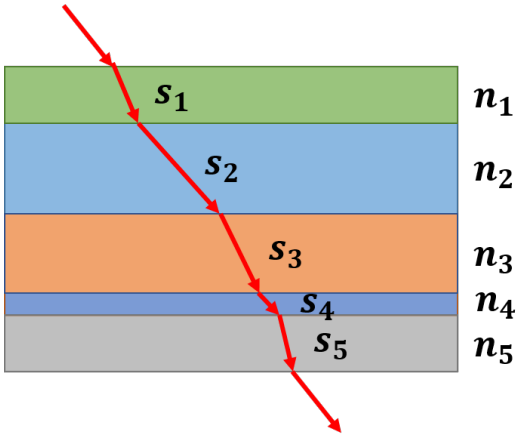

Figure 2.10: Light's optical path as it travels through various materials s of varying refractive index n.

Using (2.85), the accumulated optical phase of light beam traveling to a stationary surface and back is

$$\phi = \frac{2\pi}{\lambda_0} (2\delta) \tag{2.86}$$

where the distance δ between the light source and the surface is covered twice.

Diffraction The distance δ depends on the light's angle of incidence to the target's grating and diffraction angle from the target's grating. Light beamed onto the diffraction grating on the target's rear surface at normal incidence, will reflect and diffract from the backside of the target according to the diffraction equation

$$d \sin \theta_n^{\pm} = \pm n\lambda_0, \quad n \in \mathbb{Z} \tag{2.87}$$

where d is the diffraction grating spacing and $\theta_n^{\pm}$ is the $\pm n^{\text{th}}$ diffraction angle (Figure 2.11). This relation shows that one part of the incident beam, $n = 0$ reflects and that the rest of the incident beam, $|n| > 0$, diffracts at an infinite number of discrete angles.

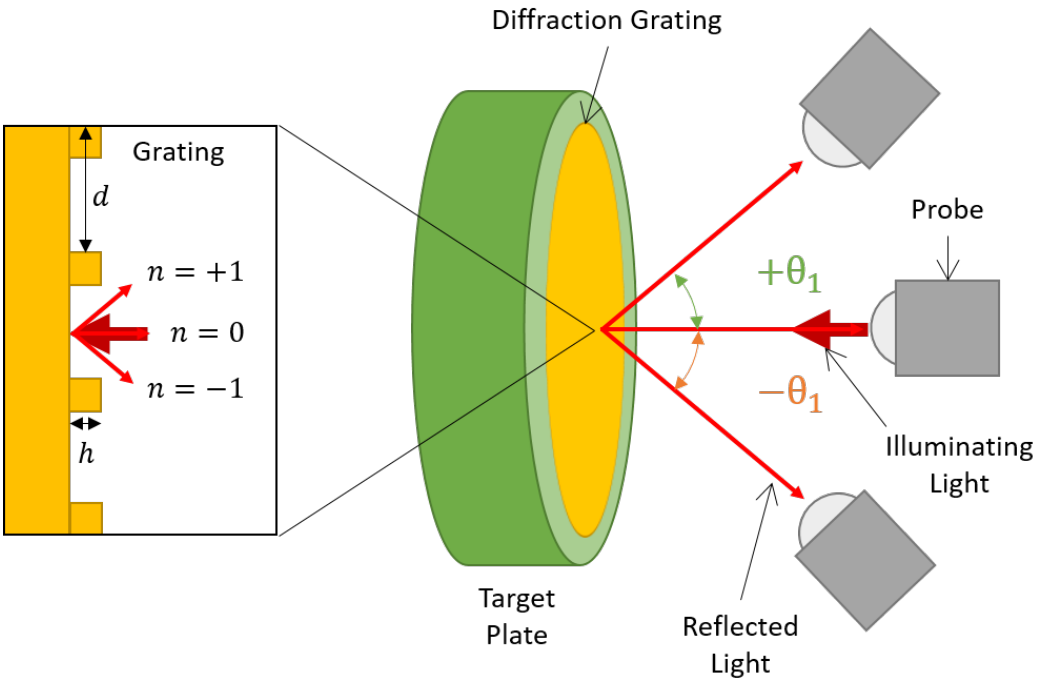

Figure 2.11: Light diffracts from a grating on the back of a target plate at angles according to the diffraction equation 2.87. Note that for $\lambda = 1550$ nm and $d = 2.5$ μm, the $n \geq 2$ beams are not diffracted.

Phase Change When the light reflects from a moving surface, the light experiences a changes in its OPL and ϕ (Figure 2.12). The change in path length depends on the longitudinal displacement $u(t)$ and transverse displacement $v(t)$ of the surface, the angle of the diffracted light θ, and time t. Phase accumulation due to longitudinal displacement is

$$\Delta\phi_u(t) = \frac{2\pi}{\lambda_0} u(t)\,(1 + \cos\theta) \tag{2.88}$$

while phase accumulation due to transverse displacement is

$$\Delta\phi_v(t) = \frac{2\pi}{\lambda_0} v(t) \sin\theta. \tag{2.89}$$

Combining these phase shifts with the initial phase of the un-shifted light ϕ_0 yields the total phase for the shifted beam

$$\phi(t) = \frac{2\pi}{\lambda_0} \left(u(t)\,(1 + \cos\theta) + v(t)\sin\theta\right) + \phi_0 \tag{2.90}$$

Heterodyning Each of the three data signals is a combination of two light beams. One beam is the light returning from the target and carries the target's displacement

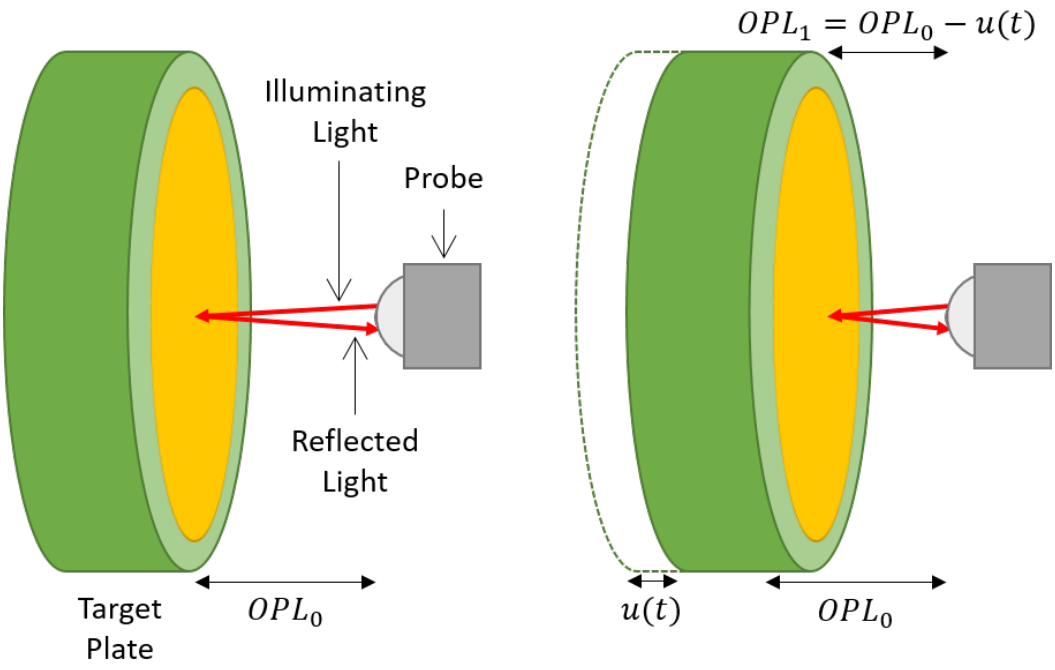

Figure 2.12: Light's OPL changes with surface displacement $u(t)$.

information. The second is a high frequency reference beam. The returning target light is combined with reference light to downshift the signal's frequency to a range that is detectable by the detector and oscilloscope, and to create a beating phenomenon that reveals the target's displacement history.

This mixing process is called heterodyning. During a heterodyne process, two signals f_1 and f_2 are combined together to create two new signals $f_1 + f_2$ and $f_1 - f_2$. This mixing process creates a beating phenomenon from the interfering waves

$$f_b = f_1 - f_2 \tag{2.91}$$

where the beat frequency f_b is smaller that the two original frequencies (Figure 2.13).

Two-Beam Interference The two-beam interference equation describes how the phase changed target light and reference light combine to create the signal read by the detector. When two waves combine, the Principle of Superposition states that their electric fields $\boldsymbol{E}$ from (2.82) are additive such that

$$\boldsymbol{E}_\star(\boldsymbol{r}, t) = \boldsymbol{E}_1(\boldsymbol{r}, t) + \boldsymbol{E}_2(\boldsymbol{r}, t). \tag{2.92}$$

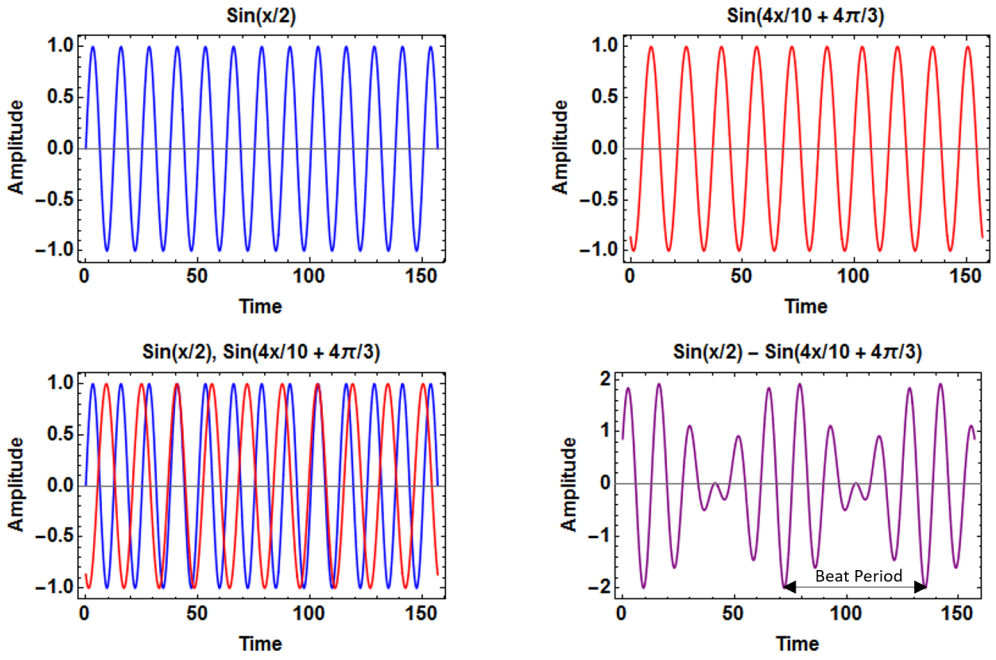

Figure 2.13: Two signals are heterodyned to produce a beat frequency smaller than either of the original frequencies. A smaller beat frequency corresponds to a longer beat period.

The irradiance I of an electric field is a measure of the field's intensity and represents the amount of power per unit area generated by the electric field. In a vacuum, the time averaged irradiance is given by

$$I(\boldsymbol{r}, t) = \frac{\epsilon_0 c_0}{2} \boldsymbol{E} \cdot \boldsymbol{E}^* \tag{2.93}$$

where ϵ_0 is the permittivity constant of a vacuum and c_0 is the speed of light. The irradiance of the combined electric fields (2.92) yields the two beam formula for the intensity of the combined waves

$$I_\star(\boldsymbol{r}, t) = I_1 + I_2 + 2\sqrt{I_1 I_2} \cos\left((\boldsymbol{k}_1 - \boldsymbol{k}_2) \cdot \boldsymbol{r} + (\omega_2 - \omega_1)\, t + (\phi_1 - \phi_2)\right) \tag{2.94}$$

Because the intensities of the two original waves I_1 and I_2 are constant, they can be subtracted out to observe the oscillating intensity of the mixed signal

$$I_{\star,o}(\boldsymbol{r}, t) = 2\sqrt{I_1 I_2} \cos\left((\boldsymbol{k}_1 - \boldsymbol{k}_2) \cdot \boldsymbol{r} + (\omega_2 - \omega_1)\, t + (\phi_1 - \phi_2)\right). \tag{2.95}$$

The polarization vectors $\boldsymbol{k}$ and frequencies ω are ideally constant while ϕ can change with time.

Phase Change of Mixed Light The phase information $\Phi_{\star,o}$ is the mixed signal's oscillating intensity $I_{\star,o}$ cosine argument (2.95)

$$\Phi_{\star,o}(\boldsymbol{r},t) = (\boldsymbol{k}_1 - \boldsymbol{k}_2)\cdot\boldsymbol{r} + (\omega_2 - \omega_1)\,t + (\phi_1 - \phi_2) \tag{2.96}$$

contains information about the frequency of the mixed light. The first time derivative of the interference phase information $\Phi_{\star,o}$ represents the rate of change of the mixed light's phase, or the angular frequency of the interfered light

$$\omega_{\star,o}(t) = \frac{\mathrm{d}}{\mathrm{d}t}\Phi_{\star,o}. \tag{2.97}$$

Combining the analyses (2.87), (2.90), (2.91), (2.95), and (2.97) to the normal and transverse interfered beams yields the signal's frequencies and recorded velocities.

Photonic Doppler Velocimetry Probe Analysis

Three Probes The diffraction equation (2.87) yields the angles $\theta_n^{\pm}$ of the $\pm n^{\text{th}}$ beams diffracting from the target's grating. The $n = 0$ beam corresponds to the reflecting beam that is shifted by the target's longitudinal motion. This single beam is captured for the PDV system. The infinite number of $|n| > 0$ beams carry coupled information regarding the target's longitudinal and transverse displacements. Two of these higher order beams are captured for the TPDV system.

Normal probe The light collected by the normal probe corresponds to the $n = 0$ diffracted beam. Using (2.87), $\theta_0 = 0$. Applying θ_0 to (2.90) yields the phase shift of the reflected light

$$\phi_N(t) = \frac{4\pi}{\lambda_0}u(t) + \phi_{N,0} \tag{2.98}$$

where the subscript N denotes the normally reflected beam. Calculating the phase information of the oscillating intensity (2.95) of the normal beam mixed with reference light yields

$$\Phi_{NR,o}(\boldsymbol{r},t) = (\boldsymbol{k}_R - \boldsymbol{k}_N)\cdot\boldsymbol{r} + (\omega_N - \omega_R)\,t + (\phi_R - \phi_N) \tag{2.99}$$

$$= (\boldsymbol{k}_R - \boldsymbol{k}_S)\cdot\boldsymbol{r} + (\omega_S - \omega_R)\,t + \left(\phi_R - \left(\frac{4\pi}{\lambda_0}u(t) + \phi_{N,0}\right)\right) \tag{2.100}$$

where the subscript R denotes the reference light and the subscript S denotes the source light. Calculating the angular frequency of the interfered light (2.97)

$$\omega_{NR,o} = \frac{\mathrm{d}}{\mathrm{d}t}\Phi_{NR,o} \tag{2.101}$$

$$= (\omega_S - \omega_R) - \frac{4\pi}{\lambda_0}\dot{u}(t) \tag{2.102}$$

and applying identity (2.6) yields the ordinary frequency of the interfered light

$$f_{NR,o} = (f_S - f_R) - \frac{2}{\lambda_0}\dot{u}(t). \tag{2.103}$$

or

$$f_{NR,o} = f_C - \frac{2}{\lambda_0}\dot{u}(t). \tag{2.104}$$

where f_C is the carrier frequency present at zero velocity. Subtracting out the carrier frequency gives the target's longitudinal velocity

$$\dot{u}(t) = -\frac{\lambda_0}{2}\left(f_{NR,o} - f_C\right). \tag{2.105}$$

Transverse probes The light collected by the transverse probes corresponds to the $|n| > 0$ diffracted beams. Using (2.87),

$$\theta_n^{\pm} = \sin^{-1}\left(\frac{\pm n\lambda_0}{d}\right). \tag{2.106}$$

The beam diffracting at a positive angle θ_n^+ will be denoted by the subscript + and the beam diffracting at a negative angle θ_n^- will be denoted by the subscript −. Applying $\theta_n^{\pm}$ to (2.90) yields the phase shift of the reflected light

$$\phi_+(t) = \frac{2\pi}{\lambda_0}\left(u(t)\left(1 + \cos\theta_n\right) + v(t)\sin\theta_n\right) + \phi_{+,0} \tag{2.107}$$

and

$$\phi_-(t) = \frac{2\pi}{\lambda_0}\left(u(t)\left(1 + \cos\theta_n\right) - v(t)\sin\theta_n\right) + \phi_{-,0}. \tag{2.108}$$

Calculating the phase information of the oscillating intensity (2.95) of the respective beams mixed with reference light yields

$$\Phi_{+R,o}(\boldsymbol{r}, t) = (\boldsymbol{k}_R - \boldsymbol{k}_+)\cdot\boldsymbol{r} + (\omega_+ - \omega_R)\,t + (\phi_R - \phi_+) \tag{2.109}$$

$$= (\boldsymbol{k}_R - \boldsymbol{k}_S)\cdot\boldsymbol{r} + (\omega_S - \omega_R)\,t + \left(\phi_R - \left(\frac{2\pi}{\lambda_0}\left(u(t)\left(1 + \cos\theta_n\right) + v(t)\sin\theta_n\right) + \phi_{+,0}\right)\right) \tag{2.110}$$

and

$$\Phi_{-R,o}(\boldsymbol{r}, t) = (\boldsymbol{k}_R - \boldsymbol{k}_-)\cdot\boldsymbol{r} + (\omega_- - \omega_R)\,t + (\phi_R - \phi_-) \tag{2.111}$$

$$= (\boldsymbol{k}_R - \boldsymbol{k}_S)\cdot\boldsymbol{r} + (\omega_S - \omega_R)\,t + \left(\phi_R - \left(\frac{2\pi}{\lambda_0}\left(u(t)\left(1 + \cos\theta_n\right) - v(t)\sin\theta_n\right) + \phi_{-,0}\right)\right) \tag{2.112}$$

where the subscript R denotes the reference light and the subscript S denotes the source light. The angular frequency of the interfered light (2.97) is now

$$\omega_{+R,o} = \frac{\mathrm{d}}{\mathrm{d}t}\Phi_{+R,o} \tag{2.113}$$

$$= (\omega_S - \omega_R) + \frac{\mathrm{d}}{\mathrm{d}t}\left(-\frac{2\pi}{\lambda_0}\left(u(t)\left(1+\cos\theta_n\right) + v(t)\sin\theta_n\right)\right) \tag{2.114}$$

$$= (\omega_S - \omega_R) - \frac{2\pi}{\lambda_0}\left(\dot{u}(t)\left(1+\cos\theta_n\right) + \dot{v}(t)\sin\theta_n\right) \tag{2.115}$$

and

$$\omega_{-R,o} = \frac{\mathrm{d}}{\mathrm{d}t}\Phi_{-R,o} \tag{2.116}$$

$$= (\omega_S - \omega_R) + \frac{\mathrm{d}}{\mathrm{d}t}\left(-\frac{2\pi}{\lambda_0}\left(u(t)\left(1+\cos\theta_n\right) - v(t)\sin\theta_n\right)\right) \tag{2.117}$$

$$= (\omega_S - \omega_R) - \frac{2\pi}{\lambda_0}\left(\dot{u}(t)\left(1+\cos\theta_n\right) - \dot{v}(t)\sin\theta_n\right). \tag{2.118}$$

Applying the identity (2.6) yields the ordinary frequency of the interfered light beams

$$f_{+R,o} = (f_S - f_R) - \frac{1}{\lambda_0}\left(\dot{u}(t)\left(1+\cos\theta_n\right) + \dot{v}(t)\sin\theta_n\right) \tag{2.119}$$

and

$$f_{-R,o} = (f_S - f_R) - \frac{1}{\lambda_0}\left(\dot{u}(t)\left(1+\cos\theta_n\right) - \dot{v}(t)\sin\theta_n\right). \tag{2.120}$$

In terms of the carrier frequency f_C present at zero velocity,

$$f_{+R,o} = f_C - \frac{1}{\lambda_0}\left(\dot{u}(t)\left(1+\cos\theta_n\right) + \dot{v}(t)\sin\theta_n\right) \tag{2.121}$$

and

$$f_{-R,o} = f_C - \frac{1}{\lambda_0}\left(\dot{u}(t)\left(1+\cos\theta_n\right) - \dot{v}(t)\sin\theta_n\right). \tag{2.122}$$

The two unknown displacements u and v can now be found from the linearly independent signals $f_{+R,o}$ and $f_{-R,o}$. This system solves for

$$\dot{u}(t) = -\left(f_{+R,o} + f_{-R,o} - 2f_C\right)\frac{\lambda_0}{2\left(1+\cos\theta\right)} \tag{2.123}$$

and

$$\dot{v}(t) = -\left(f_{+R,o} - f_{-R,o}\right)\frac{\lambda_0}{2\sin\theta}. \tag{2.124}$$

The frequencies of the diffracted target beams can be found by analyzing the signal recorded by the oscilloscope and yield the un-coupled longitudinal and transverse motions of the target.

2.4 Spectral Analysis of Waves

Fourier Transforms

Discrete Fourier Transform (DFT) While constructing a wave from a set of frequencies is fairly straight forward, determining the frequencies of a given wave is difficult[5] [38, 45, 46]. This challenge is exacerbated for noisy signals comprised of discrete data points that do not behave in a periodic fashion.

Fourier transforms are a means of extracting the frequency content of a wave represented as amplitude vs time. If a wave is represented by a continuous function $f(t)$ then the continuous Fourier transform $\mathcal{F}_t$ returns a continuous function $F(\nu)$ whose value is proportional to the magnitude of each frequency component ν over $f(t)$ entire time domain

$$F(\nu) = \mathcal{F}_t\left[f(t)\right](\nu) \tag{2.125}$$

$$= \int_{-\infty}^{\infty} f(t)e^{(-2\pi i\nu t)}\mathrm{d}t. \tag{2.126}$$

However, experimental data is rarely continuous. Rather, data is collected at a precise sampling rate yielding a time-series of individual amplitude vs time data points. This results in a discretized function $f_k = f(t_k)$ where t_k is the time of the k^{th} point collection for $k = 0, \ldots, N-1$ and N sample points (Figure 2.14).

The continuous Fourier transform (2.126) cannot be applied to the discrete function f_k. Instead, the discrete Fourier transform (DFT) $\mathcal{F}_n$ was designed for aperiodic-discrete signals. The DFT is calculated by sampling the discrete-time Fourier transform (DTFT). The DTFT is continuous in frequency space, and sampling the DTFT produces a function that is discrete in frequency space but that can be calculated by a a computer. The DFT returns a value proportional to the magnitude of each discrete frequency component n over the time domain $t \in [t_0, t_{N-1}]$

$$F_n = \mathcal{F}_k\left[\{f_k\}_{k=0}^{N-1}\right](n) \tag{2.127}$$

$$= \sum_{k=0}^{N-1} f_k e^{\left(-2\pi i n\frac{k}{N}\right)}. \tag{2.128}$$

The discrete frequencies n corresponding to each DFT coefficient F_n are

$$n \in \left\{0, \frac{F_s}{N}, \frac{2F_s}{N}, \ldots, \frac{F_s}{2}\right\} \tag{2.129}$$

[5] This section draws heavily on material found in [38], [45], and [46].

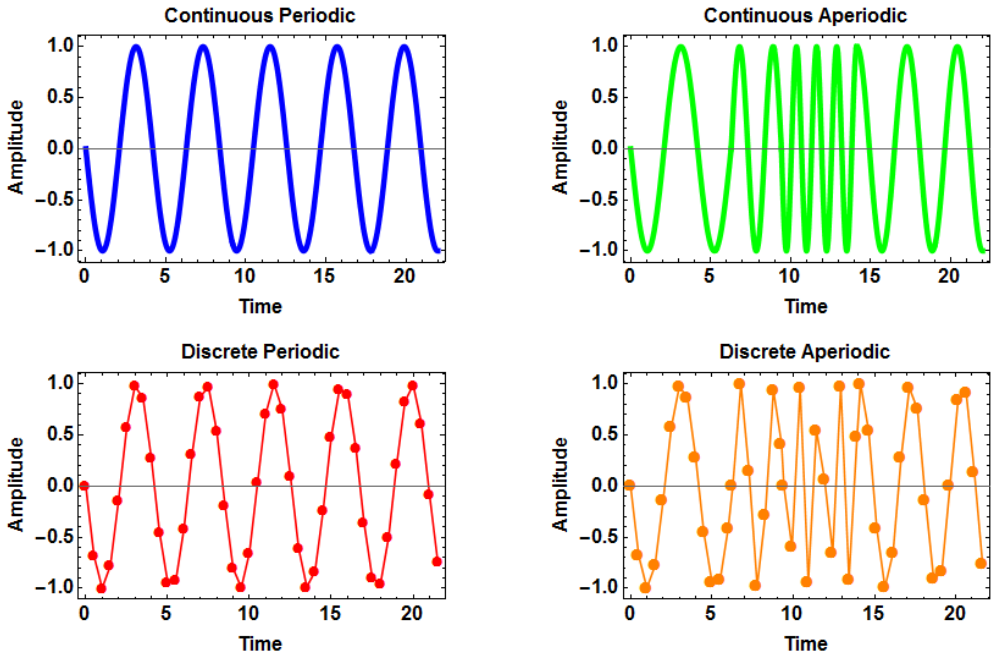

Figure 2.14: Continuous, discrete, periodic, and aperiodic data.

where F_s is the sampling frequency and N is the number of data points in the signal. This relation shows that frequency (wavelet) resolution, or the space between frequency bins, is proportional to the length of the data signal. In addition, the maximum frequency that can be detected is known as the Nyquist frequency f_N

$$f_N = \frac{F_s}{2} \tag{2.130}$$

which is directly related to the sampling frequency. Therefore, the sampling frequency sets the upper bound on accurate frequency detection.

Fast Fourier Transform (FFT) and Zero-padding The fast Fourier transform (FFT) is an efficient algorithm for computing a data set's DFT when the total number of data points N is a power of two. This reduces the total computation time from $2N^2$ to $2N \log_2 N$. If a signal does not have N as a multiple power of two, then the signal can be zero-padded to a length equal to a power of two so that the FFT may be implemented efficiently. Zero-padding involves appending a series of zeros to the end of a time series signal which increases the length of the signal to N_{fft} without adding additional information (Figure 2.15). Because zero-padding increases the total number of data points to N_{fft}, zero-padding increases the number of frequency bins in (2.129). This increases the FFT resolution because more data points are used, however this does not increase the frequency (wavelet) resolution because no new

information is being added. The frequency bin spacing Δf_{bin} of a zero-padded signal is

$$\Delta f_{\text{bin}} = \frac{F_s}{N_{fft}} \tag{2.131}$$

while the frequency bin spacing of a signal without zero-padding is

$$\Delta f_{\text{bin}} = \frac{F_s}{N}. \tag{2.132}$$

Zero-padding will result in an amplitude-frequency plot that is more resolved, however zero-padding will not increase the ability to distinguish frequency components that are close together. Zero-padding does have the drawback of increasing computation time since $N_{fft} \geq N$.

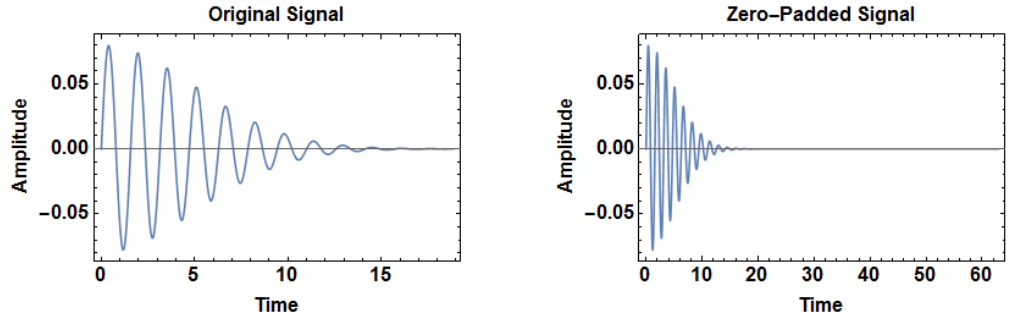

Figure 2.15: A signal (left) is zero-padded to increase it's length in time (right).

Short Time Sliding Fourier Transform (STFT) The DFT yields the frequency content of the signal over the signal's entire time domain $t \in [t_0, t_{N-1}]$. This is fine for a stationary signal where frequency does not change with time because frequencies are not expected to change, and are therefore present, over the entire t interval. However, lack of time resolution does create problems when the signal's frequency varies with time.

The short time sliding Fourier transform (STFT) process was developed to provide time resolution to the DFT. During a STFT, the data is windowed according to time τ and a discrete Fourier transform (2.129) is performed on of each window of data. This window starts at $[0, \tau]$ and will then slide up in time according to the window shift parameter ε to $[\varepsilon, \tau + \varepsilon]$. The process of sliding, windowing, and computing the DFT continues until all of the data has been decomposed. This results in an array of data that represents the intensity of each frequency component at the time center of each time window.

Unlike the continuous Fourier transform, which will only produce a non-zero value at the exact frequency of the continuous function, the windowed DFT will output non-zero values called sidelobes for frequencies close to the actual frequency value (Figure 2.16). This phenomenon is called spectral leakage. Spectral leakage can complicate the processes of identifying dominant frequency components.

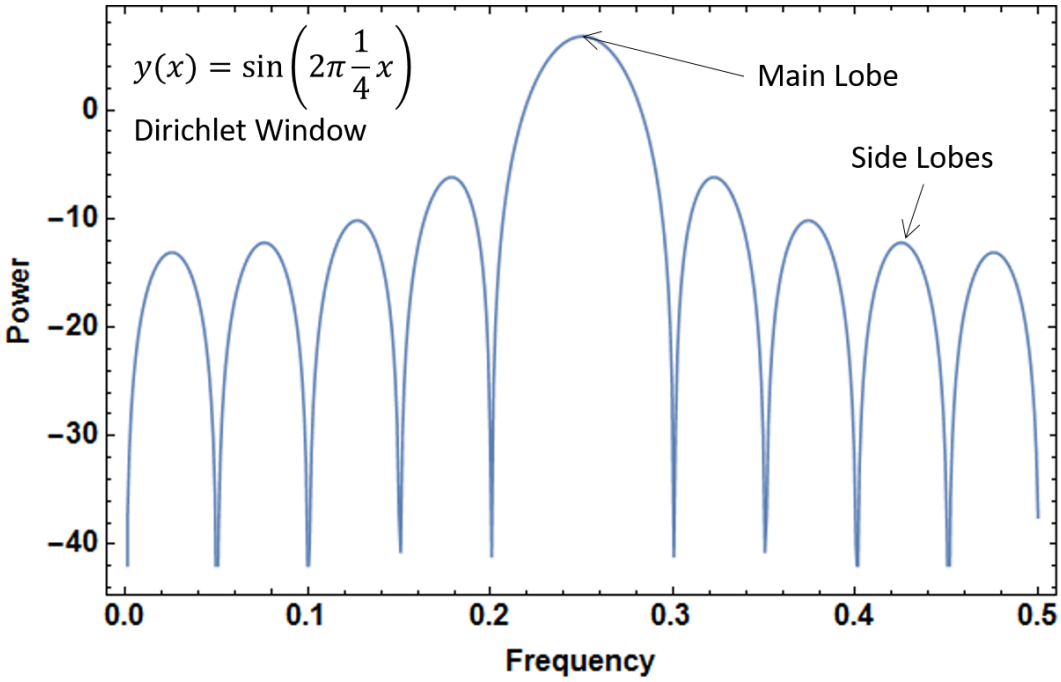

Figure 2.16: Spectral leakage in a windowed signal's periodogram.

Windowing Methods The precision and accuracy of the STFT depends on the choice of window function over the time window τ (Figure 2.17) [47]. When a signal is multiplied by a window function, a new amplitude modulated signal is generated that is non-zero within the window and rapidly tends to zero outside of the window (Figure 2.18). This clamping of the signal at the edges reduces the spectral leakage phenomenon by reducing boundary discontinuities. Removing boundary discontinuities makes the signal periodic in time, which is an assumption of the Fourier transform. Although, information at the edge of the window is lost when a window is clamped. Information loss is mitigated by shifting the window by an amount $\varepsilon < \tau$ to create overlap between adjacent windows.

The general tradeoff with different windowing functions is the amplitude minimization of the sidelobes and the width minimization of the main lobe (Figure 2.16). The boxcar-rectangle, Hamming, and Hann are common window functions that perform

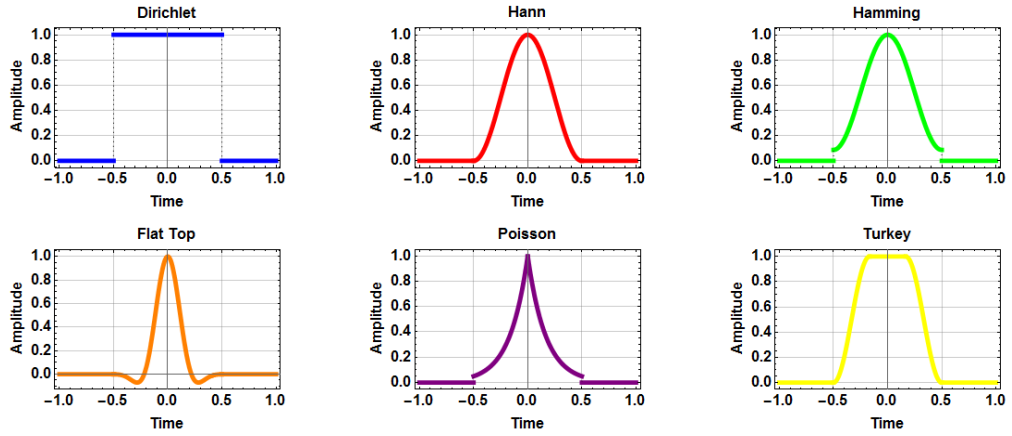

Figure 2.17: Windowing functions are non-zero within the time window and tend to zero outside of the time window.

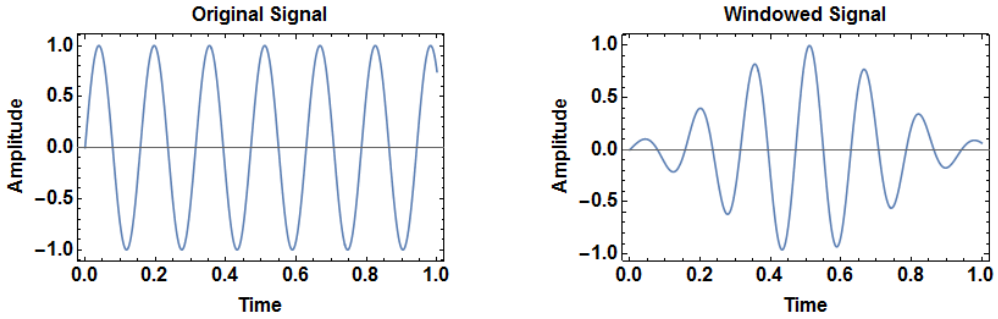

Figure 2.18: A signal (left) is amplitude modulated by a window function to produce a modified signal (right).

well over different frequency ranges and at different noise levels (Dolan). For data with high noise levels, the boxcar and Hamming windows are preferred. However, if the level of noise is low, then a Hann window will provide more precise results.

Uncertainty Principle The uncertainty principle plays a large role in the STFT. Classically, the uncertainty principal in quantum mechanics states that knowledge of the values of position x and momentum p are limited by

$$\sigma_x \sigma_p \geq \frac{\hbar}{2} \tag{2.133}$$

where σ_x is the standard deviation of position, σ_p is the standard deviation of momentum, and $\hbar$ is the reduced Planck constant. Similarly, the uncertainty relationship for frequency f and time t during signal processing is the Gabor limit

$$\left(\Delta \bar{f}\right) \tau \geq \frac{1}{4\pi} \tag{2.134}$$

where $\left(\Delta\bar{f}\right)$ is the characteristic peak width or thickness of a frequency's line on a spectrogram (Figure 2.19). Spectrograms are a plot of the intensity of each frequency component as a function of time. Darker colors indicate a higher frequency presence at a given moment in time. The darkest color indicates the dominant frequency component.

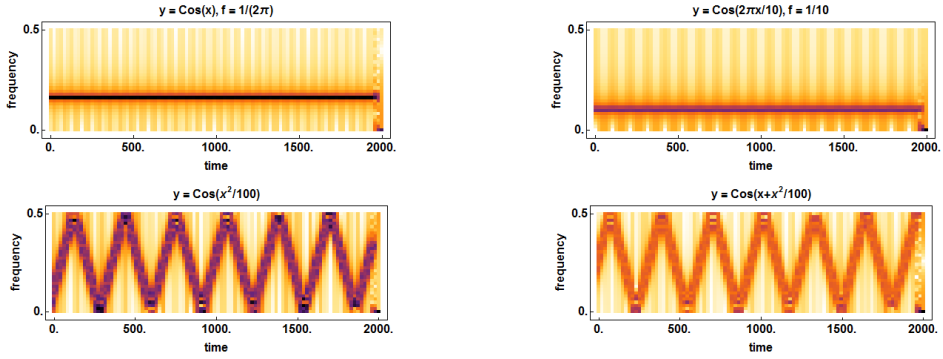

Figure 2.19: Spectrograms of functions.

If the window τ is large, then N is large and the frequency resolution (2.132) is high. However, with a large time window, it is unknown at what point in time each of the resolved frequencies occurred. Although, if the window τ is small, then N is small and the frequency resolution (2.132) is low. This means that it is difficult to see small changes in frequency (ie it is hard to separate frequencies that are close together) over a small time window. Finally, if τ is too small, then there may not be enough data points to compute the DFT or enough periods of the signal might not be captured to accurately compute the DFT. To accurately decompose the signal using the DFT, it is good practice to make τ long enough to capture at least one period of the local signal.

Power Spectral Density

Periodogram Now that the frequencies and their respective Fourier coefficients have been determined at each time center, the strength of each frequency can be determined. A frequency's strength is quantified by its power density. At each time center, the power density – or power per unit frequency – can be calculated in the frequency domain using the signal's Fourier coefficients [48]. Similar to the calculation of Fourier coefficients, the process for calculating the power spectral density (PSD) of a continuous function is different for that of a discrete function.

The PSD of a continuous signal $f(t)$ in the frequency domain is calculated from the

a truncated Fourier transform similar to (2.126)

$$F(\nu) = \frac{1}{\sqrt{T}} \int_0^T f(t) e^{(-2\pi i \nu t)} \mathrm{d}t. \tag{2.135}$$

These coefficients are now used to calculate the PSD of each frequency of the continuous signal

$$S(\nu) = \lim_{T \to \infty} \boldsymbol{E} \left[|F(\nu)|^2 \right] \tag{2.136}$$

where $\boldsymbol{E}$ is the expected value operator.

However, for a discrete data signal $f_k = f(t_k)$ the DFT coefficients (2.128) obtained at each STFT time center are used to calculate the discrete PSD

$$S(n) = \frac{\Delta t}{N} \left| \sum_{k=0}^{N-1} f_k e^{\left(-2\pi i n \frac{k}{N}\right)} \right|^2 \tag{2.137}$$

for

$$\frac{-1}{2\Delta t} < f \leq \frac{1}{2\Delta t}. \tag{2.138}$$

This estimation of PSD for respective frequencies is called a periodogram.

Peak Fitting The dominant frequency of each time center is found using the a power spectral density distribution or periodogram. There are several methods for finding the peak in the power-frequency distribution, each of which can yield a slightly different peak location (Figure 2.20). First, the frequency corresponding to the maximum power can be found. However, finding the simple maximum of the data limits the possible choices for frequency maxima to frequency bins in the dataset (2.129). With the second method, peak fitting, it is possible to interpolate the data set and find the location of the peak in-between frequency bins. Example fits include Gaussian and polynomial. A Gaussian fit is believed to have a frequency resolution of

$$\Delta f = \left(\sqrt{\frac{6}{F_s}} \frac{\sigma}{\pi} \right) \tau^{\left(\frac{-3}{2}\right)} \tag{2.139}$$

where σ is the noise fraction and τ is the window size [38]. Finally, wavelet analysis can be used to find the dominant frequencies [49, 50]. At high frequencies, wavelet analysis yields great time resolution for rapidly changing signals. At low frequencies, wavelet analysis yields great frequency resolution for slowly changing signals.

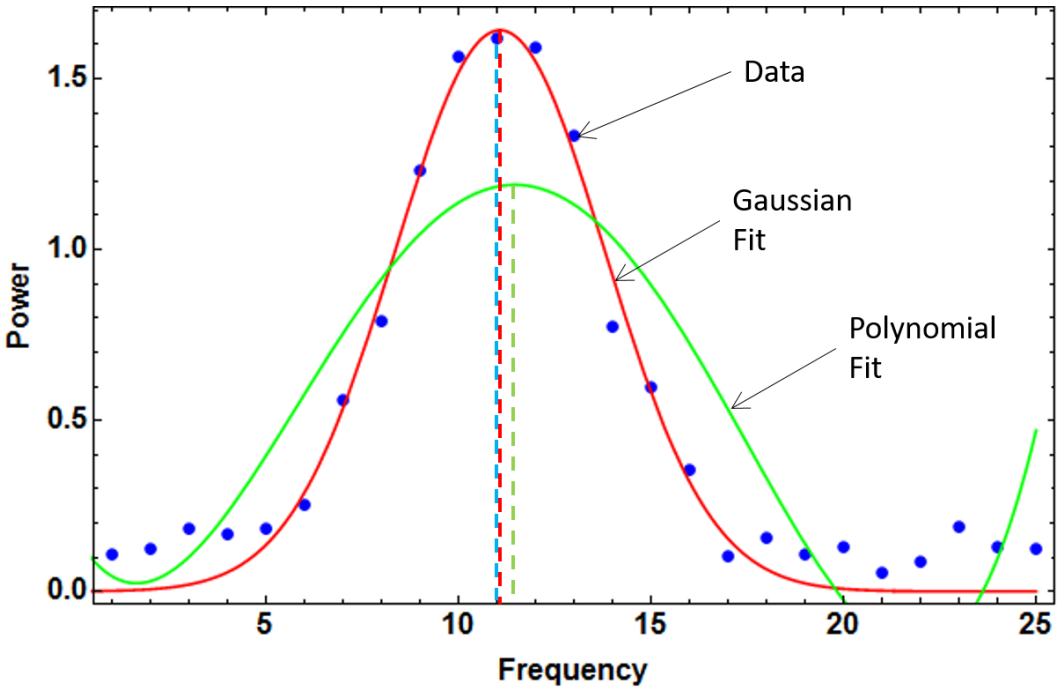

Figure 2.20: The estimated location of a peak depends on the peak-finding method. Finding the maximum of the data points restricts the returned maximum to one of the points in the data set. Using a curve fitting method allows for interpolation between points in the data set and can return a maximum that is in-between two data points.

Velocity Extraction

Each of the three signals from the PDV-TPDV are processed using a STFT. The STFT coefficients are then used to calculate the power spectral density of each frequency bin at each time center. The peak in the power spectrum at each time center locates the dominant frequency at each time center. The carrier frequency is then subtracted from the dominant frequency. This carrier frequency upshifts the frequency content of the underlying signal to obtain whole fringes for window sizes that are shorter than the signal's period (Figure 2.21). This enables the analysis of slowly varying signals with small window sizes and therefore increased time resolution.

Finally, the velocity of the target is calculated at each time center using the proper velocity-frequency relationship: (2.105), (2.123), or (2.124). The velocity's time resolution is proportional to τ and the velocity's resolution is proportional to N. The window size needs to be chosen such that changes in velocity have a non-zero rise time. This means that there are gradual changes in velocity, rather than sudden jumps.

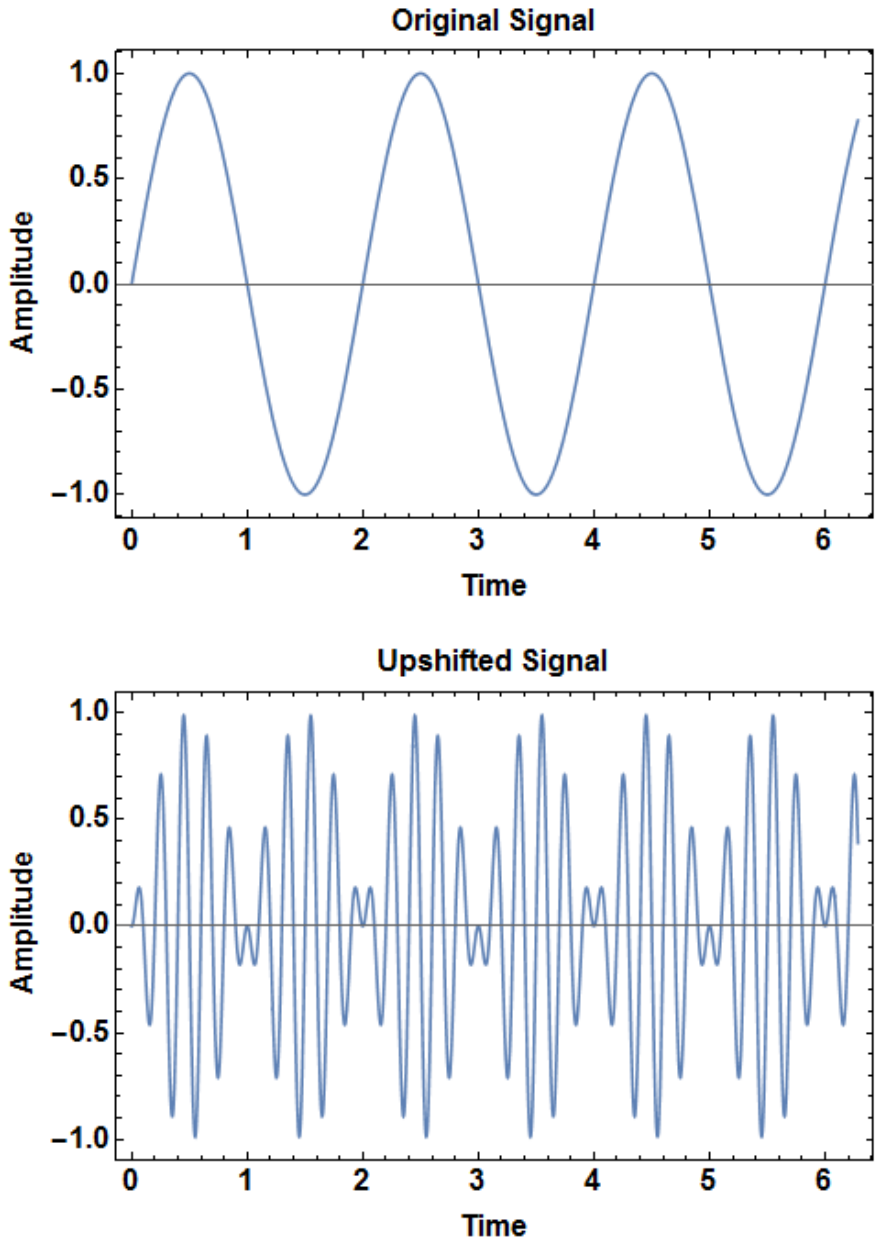

Figure 2.21: A 0.5 Hz signal is upshifted by a 5 Hz signal to obtain more fringes in a given time window.

Chapter 3

METHODS

3.1 Specimen Preparation

Materials

Target Plate To evaluate the capabilities of the combined photonic Doppler velocimetry (PDV) and transverse photonic Doppler velocimetry (TPDV) interferometer, the target material needed to have a strong coupling between longitudinal and transverse motion[1] [39]. Single crystalline y-cut α-quartz was selected as a target material because it's strong coupling between longitudinal and transverse motion when impacted normally is well documented in literature (Figure 2.7).

The target plate's dimensions were restricted by the powder gun's 36 mm barrel diameter and by the length of the desired data record. The target plate had to have a smaller diameter than the flyer plate to allow space for shorting pins. Since the flyer plate's diameter was limited by the barrel diameter, 33 mm was an approximate upper bound on the target plate's diameter. The length of the desired data record, approximately 2 μs, set a lower bound on the target plate's diameter. The target's diameter needed to be sufficiently large such that lateral release waves generated at the target plate's edges would not reach the center of the target before the desired amount of data was collected. This set the lower bound on target plate diameter at approximately 25 mm.

Plates of single crystalline y-cut α-quartz were obtained from UniversityWafer in South Boston, MA with specifications listed in Table (3.1). A plate was chosen for impacting and this plate's z-axis was found using a petrographic microscope and interference figures [51]. The z-axis was then indicated with an etch mark on the plate's circumference. The y-cut character of two other samples were checked using electron backscatter diffraction (Appendix A).

Values for quartz's density and elastic-constant tensor listed in Table (3.2) were taken from literature. The data from reference [43] is for ordinary cultured quartz and was obtained using resonance-ultrasound spectroscopy.

[1] This chapter draws heavily on material found in [39].

Geometry	Diameter	Thickness	Surface roughness	y-cut tolerance
cylindrical	30 ± 0.1 mm	5 mm	$8 - 10$ Å	$\pm 10'$

Table 3.1: Quartz plates specifications.

Density	C_{22}	C_{24}	C_{44}	C_{66}
2.6497 g/cm^3	87.16 GPa	18.15 GPa	58.14 GPa	40.26 GPa

Table 3.2: Ordinary cultured quartz material constants [43].

Flyer Plate Three requirements constrained the choice of flyer material. First, the flyer material needed to be isotropic. Choosing an isotropic flyer material simplified alignment procedures. Second, an appropriate flyer material had a low density ρ and longitudinal wavespeed c_l. This created a low acoustic impedance Z

$$Z = \rho \cdot c_l \tag{3.1}$$

and resulted in lower pressures during the experiment for a given impact velocity [52, 53]. Third, the flyer material needed to have a high yield strength in compression and shear. This ensured that the flyer plate would not fail before the target plate failed, and that the impact interface could support a sufficient amount of shear stress. Borosilicate glass was chosen for the flyer material.

The flyer plate's thickness was chosen such that wave reflections from the backside of the flyer plate would not reach the impact interface prior to separation. Specifically,

$$L_F > \frac{c_{F,l}}{c_{T,l}} L_T \tag{3.2}$$

where L_F and L_T are the respective flyer and target plate thicknesses, and $c_{F,l}$ and $c_{T,l}$ are the respective flyer and target plate longitudinal wavespeeds.

Plates of Borofloat 33 glass were obtained from UniversityWafer in South Boston, MA with specifications listed in Table (3.3). Values for borosilicate's material constants listed in Table (3.4) were taken from Schott North America mechanical properties data sheets [54].

Photolithography

A diffraction grating was fabricated on the backside of the target plate as part of the TPDV system. The grating was designed according to reference [55] and fabricated according to reference [56] with materials specified in Table (3.5) (Figure 3.1).

Geometry	Diameter	Thickness	Surface roughness
cylindrical	33.909 ± 0.1 mm	6.5 ± 0.1 mm	< 1.0 nm

Table 3.3: Borosilicate glass plates specifications.

Density	Young's Modulus	Poisson's Ratio
2.23 g/cm^3	64 kN/mm^2	0.2

Table 3.4: Borosilicate glass material constants [54].

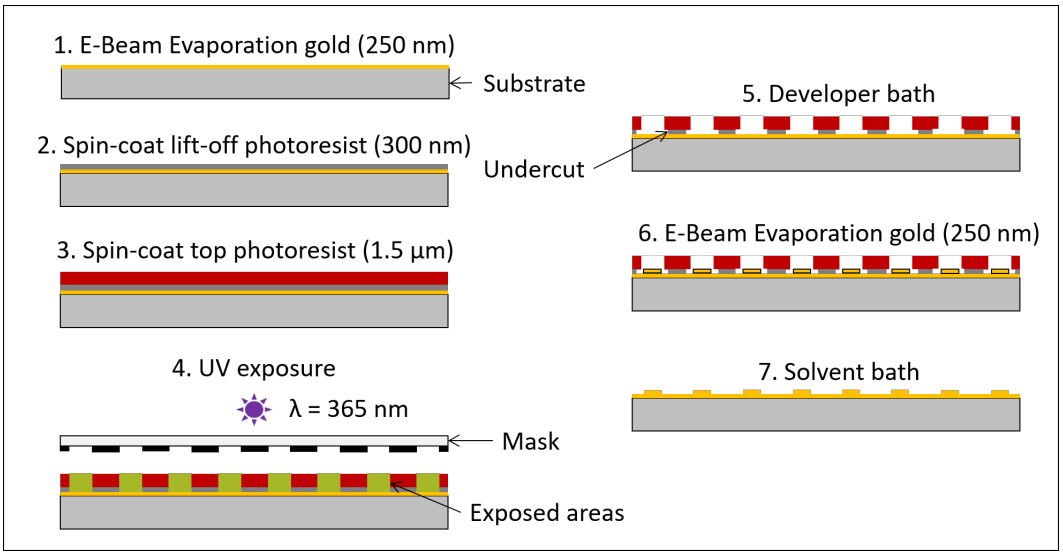

Figure 3.1: A substrate is coated in a layer of gold, followed by a layer of lift-off (bottom photoresist) and a top layer of photoresist. The coated substrate is exposed to ultra-violet light and then developed in a bath. Another layer of gold is deposited and the remainder of the photoresist is removed in a solvent bath. A gold diffraction grating results from this process. Modified schematic courtesy of Christian Kettenbeil.

The quartz plates were coated in a thin layer of metal and a thin layer of gold using physical vapor deposition in a cleanroom environment. The gold layer serves as a reflective coating and the metal layer adheres the gold to the quartz substrate (Figure 3.2). Photolithography was then performed in a cleanroom environment using a Ronchi Rulings mask pitched at 400 line per mm (2.5 μm spacing) manufactured by Applied Image. The grating was aligned parallel to the quartz substrate's x-axis (Figure 3.3). The layers of metal and photoresist were thin and have a negligible

Adhesion material	chrome, 10 nm
Reflective coating	gold, 250 nm
Lift-off 1	LOR 3A (MicroChem Corp.), 0 nm
Photoresist 2	Microposit S1813 (MicroChem Corp.), 1000 nm
Grating material	Microposit S1813 (MicroChem Corp.), ≈1000 nm

Table 3.5: Diffraction grating specifications.

effect on the measured free-surface velocity history. The final grating's period, height, and shape were checked with atomic force microscopy (Figure 3.4).

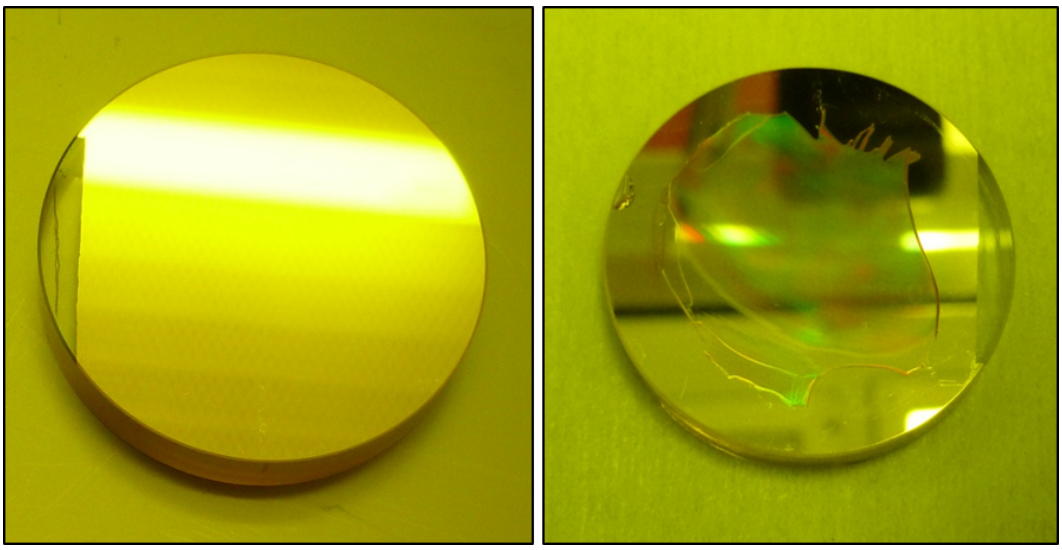

Figure 3.2: A quartz substrate coated in gold (left). A photoresist diffraction grating in the center of the substrate (right).

This grating will produce 1st order diffracted beams at angles of (2.87)

$$\theta_1 = \sin^{-1}\left(\pm\frac{1550.012\times10^{-9}}{2.5\times10^{-6}}\right) \tag{3.3}$$

$$= \pm 38.32°. \tag{3.4}$$

Note that the 2nd order and high order diffracted beams are not generated since they are predicted to occur at angles greater than 90°.

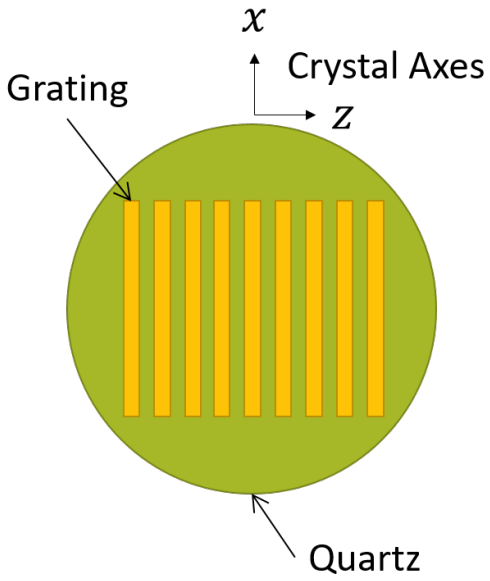

Figure 3.3: The diffraction grating is aligned parallel to quartz's x-axis (not to scale).

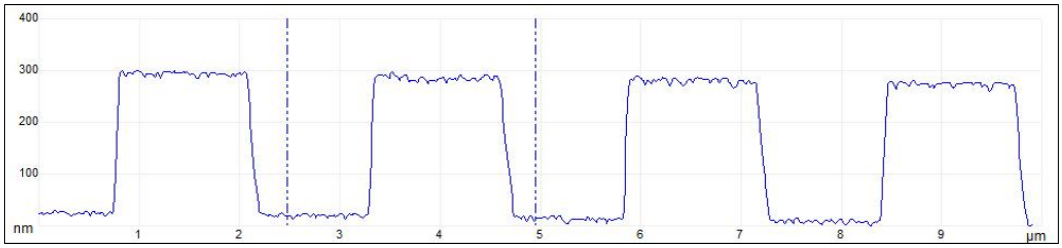

Figure 3.4: Atomic force microscopy data from a practice gold grating on tungsten carbide. The top plateaus are the tops of the grating and the bottom plateaus are the gold coating. This grating has a height of about 290 nm. Courtesy of Christian Kettenbeil.

3.2 Interferometer Construction

Optical Configuration

A photonic Doppler velocimetry system was built by Michael B. Rauls with a transverse modification[2]. The combined photonic Doppler velocimetry (PDV) and transverse photonic Doppler velocimetry (TPDV) system is comprised of drive, reference, and sensing groups[3] (Figure 3.5). Each group comprises of optical devices linked with fiber-optic cables. The lasers and main PDV-TPDV components

[2]This assembly was initially referred to as the heterodyne transverse velocity interferometer (HTVI). It is now referred to as the transverse photonic Doppler velocimetry system.

[3]This section draws heavily on material found in [39].

are housed in boxes. These boxes and oscilloscope reside outside of the impact chamber (Figure 3.6). Four system channels collect and carry data. One channel measures the flyer plate's down barrel velocity, one channel carries PDV data, and two channels carry TPDV data.

Drive Group The drive group generates the PDV-TPDV system source light, illuminates the target, and collects light reflected and diffracted from the target.

A Koheras BOOSTIK E15 high power, low-noise single frequency Erbium doped fiber laser manufactured by NKT Photonics A/S generates the driver light source. This laser has an adjustable center wavelength between 1550 nm and 1570 nm with a maximum power output of 2 W. A wavelength of 1550.012 nm and a power output of 2 W was chosen for these experiments. A low power was chosen so the light would not scorch the diffraction grating and so the detection system would not be overwhelmed.

The laser light is carried through a polarization-maintaining PM 8 μm fiber optic cables, a single-mode (SM) 9 μm fiber optic cables, and a fiber-optic connector with angled physical contact (FC/APC). A PM fiber is used initially since it came with the laser. SM fibers are used after the initial PM fiber since the following optical components are insensitive to the light's polarization. Connectors with angled physical contact were used to minimize backreflection. The light arrives at a Compact Fiberoptic Coupler/Splitter 1x4 with a 25/25 coupling ratio manufactured by Agiltron. The splitter splits the laser light into four equal beams, forming four channels. Each beam is carried by SM cables and FC/APCs to a three-port Optical Circulator manufactured by Agiltron. The circulator sends the light along SM cables to the probes.

The PDV probe is a pigtail style collimator for 1550 nm with a 1.4 mm aspheric lens manufactured by OZ Optics. The two TPDV probes are pigtail style collimator for 1550 nm with an 6.2 mm aspheric lens manufactured by OZ Optics. The TPDV probes have a wider lens than the PDV probes to capture more light from the displacing target. The down barrel probe was manufactured by AC Photonic. The light returns from the probes and re-enters the circulators which re-direct the light sent back along SM cables and FC/APCs to Variable Fiber Optic Attenuators manufactured by OZ Optics. These attenuators decrease the strength of the reflected target light to about -14dBm.

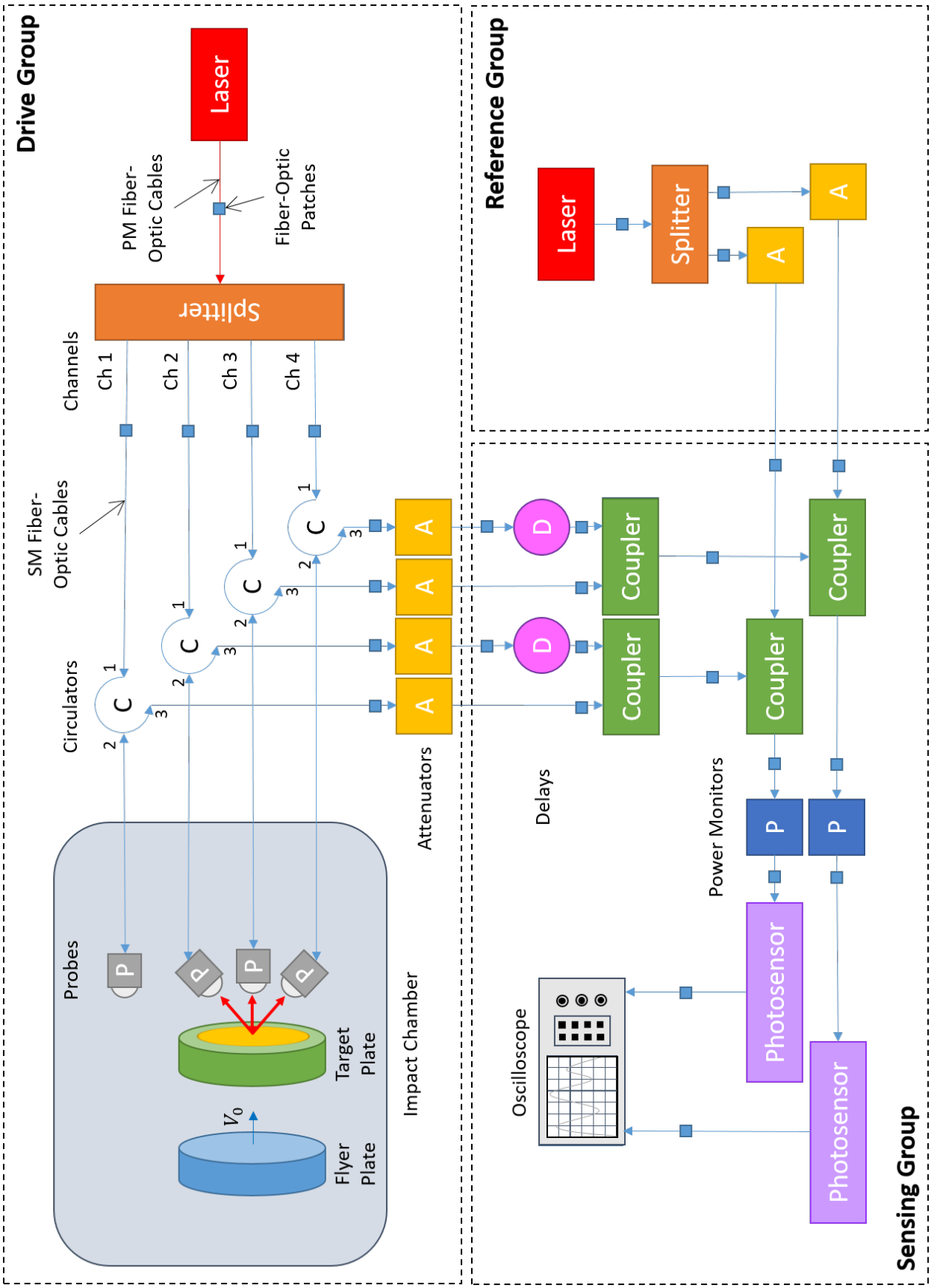

Figure 3.5: PDV-TPDV system configuration consists of drive, reference, and sensing groups connected through fiber-optic cables.

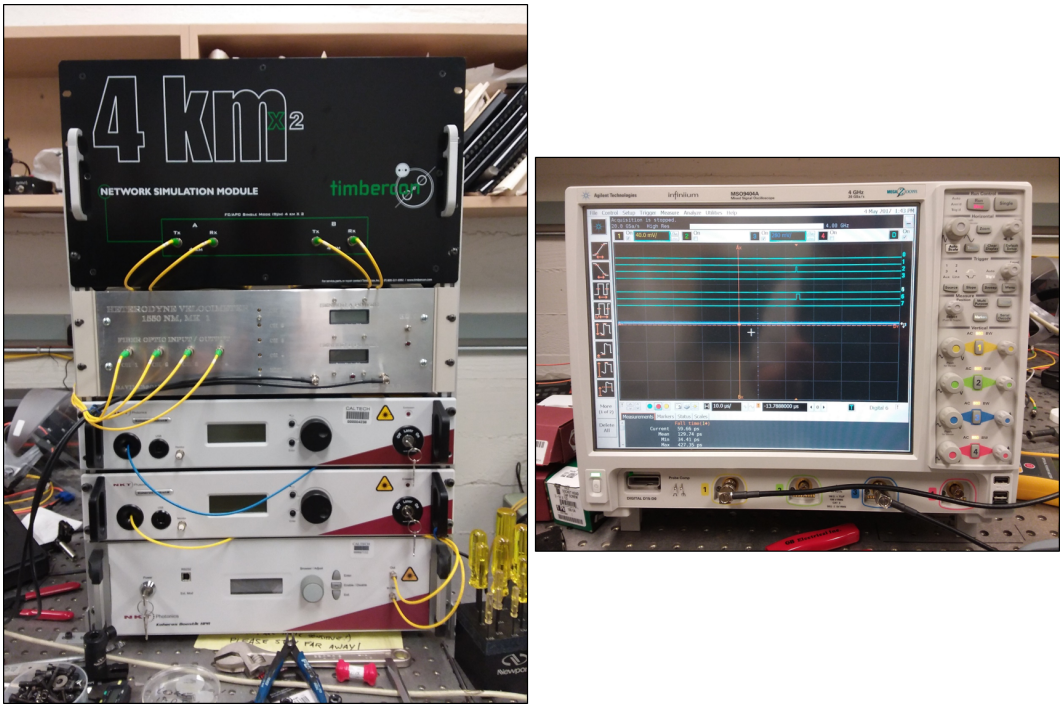

Figure 3.6: Laser systems (left) with the driver laser, booster, reference laser, interferometer box, and fiber-delay (bottom to top). The digital oscilloscope (right) collects data.

Reference Group The reference group generates the PDV-TPDV system reference light. A Koheras ADJUSTIK E15 low noise, single frequency Erbium doped fiber laser manufactured by NKT Photonics A/S generates the reference light source. This laser has an adjustable center wavelength between 1535 nm and 1580 nm with a power output of 40 mW. The wavelength of the emitted light is selected to adjust the PDV-TPDV system's upshift. Increasing the upshift decreases the system's sensitivity. Because oscilloscopes have limited bandwidth, upshifting also decreases the system's maximum detectable velocity. However, upshifting is necessary to achieve high temporal resolution at low velocities. Wavelengths used in these experiments are found in Table (3.6).

Driver wavelength	1550.012 nm
Reference wavelength	1550.023 nm
Calculated beat (carrier) frequency	1.37259 GHz
Calculated maximum detectable velocity	2036.26 m/s

Table 3.6: Laser specifications with approximate beat frequencies and maximum detectable velocities.

The laser light is carried through SM cables and FC/APC connectors to a Single Mode FiberOptic Coupler/Splitter with a 50/50 coupling ratio manufactured by Agiltron. The splitter splits the laser light into two equal beams. Each beam is carried by SM cables and FC/APCs to Variable Fiber Optic Attenuators manufactured by OZ Optics. These attenuators decrease the strength of the reference light to -4dBm.

Sensing Group The four channels from the driver group and two beams from the reference group meet in the sensing group. The sensing group mixes the target light with the reference light and converts the analog voltage signals into digital signals for analysis.

Two driver channels are sent through a 4 km x2 Network Simulation Module manufactured by Timbercon. Each delayed channel is combined with an un-delayed channel. SM cables and FC/APCs carry each channel to one of two Single Mode FiberOptic Coupler/Splitters with a 50/50 coupling ratio manufactured by Agiltron. This forms two sets of paired channels. The 4 km loop postpones the delayed signal by approximately 19 μs. Since the velocity records from the target last approximately 3 μs and the signals' frequency components are distinct, the delay allows the signals to be distinguished while decreasing the number of PDV-TPDV system components (Figure 3.7).

The two combined sets of channels are each blended with a reference beam. The combined channels and reference beams are carried through SM cables and FC/APCs in a Single Mode FiberOptic Coupler/Splitter with a 10/90 coupling ratio manufactured by Agiltron. The two signals output from the coupler contain 10% reference light and 90% driver light. Each of the two driver-reference channels are fed through SM cables and FC/APCs into a Power Monitor with a -50 to $+16$ dBm power range and 1280 to 1580 nm spectral range manufactured by EigenLight. The power monitors measure and display the amount of power traveling through the fiber-optic, but do not amplify or attenuate the signal. After the power monitor, the two channels are sent through SM cables and FC/APCs to an Optical Receiver (photodiode) with a bandwidth of 30 kHz to 13 GHz manufactured by Miteq. The photodiodes turn the light signal into an electrical signal by generating a current with captured photons. A 4 GHz analog bandwidth MSO9404A Mixed Signal Oscilloscope (MSO) manufactured by Agilent Technologies monitors the electrical current generated by the photodiodes, collecting data at 20 giga-samples per second.

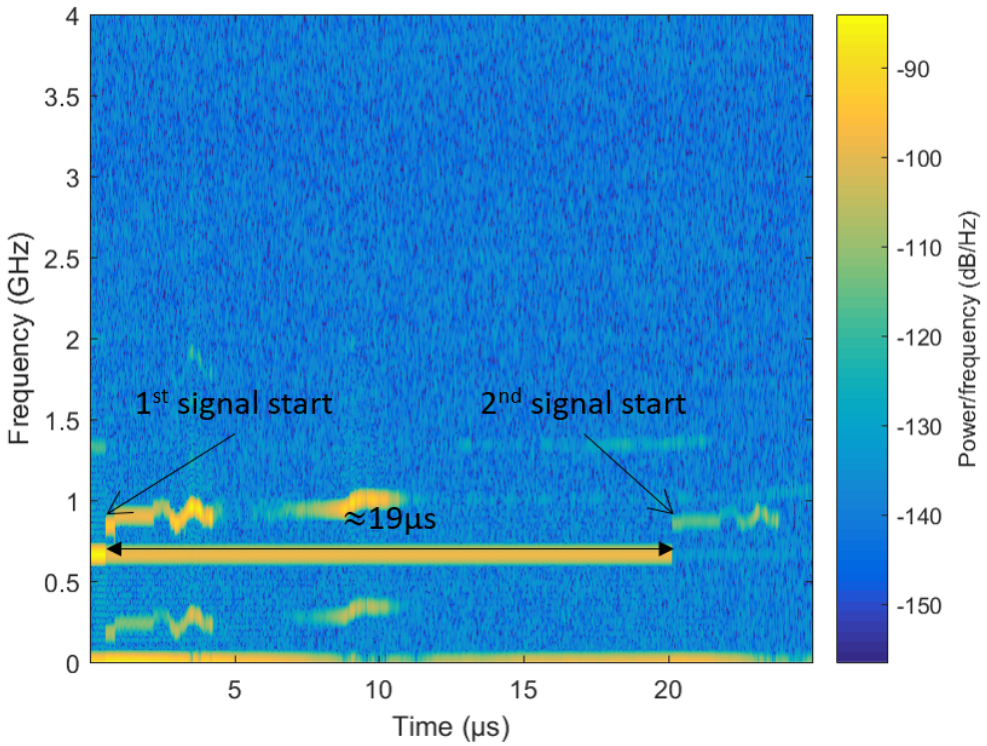

Figure 3.7: A signal delayed by approximately 19 μs is distinguished from an un-delayed signal by its frequency components in a spectrogram.

Data Acquisition Data acquisition is triggered on the oscilloscope using four CA-1038 Shorting Pins manufactured by Dynasen. The shorting pins were mounted through the specimen holder and soldered to an ethernet cable. A CS2-50-300 Pin Mixer manufactured by Dynasen applies a voltage across the pins.

When the flyer plate impacts the target plate, the shorting pins are crushed, and the circuit shorts. For an ideal short circuit, resistance R becomes zero. Given Ohm's law

$$\Delta V = \iota R, \tag{3.5}$$

the voltage ΔV two points will be zero in a short circuit regardless of the current ι. The pin mixer detects this drop in voltage and outputs the shorting pins' summing output and individual outputs. The summing output is linked to all four pins and outputs a signal once one of the pins is shorted. The summing output is chosen to trigger data acquisition so that a malfunctioning pin will not prematurely start data collection.

The summing output is then directed through a circuit designed by Michael B.

Rauls to increase the summing output's voltage. The voltage increase allows for a higher trigger threshold and prevents electromagnetic disturbances from prematurely triggering data acquisition. The modified summing output is fed into the oscilloscope a data from the PDV-TPDV system is collected when a critical voltage is reached.

Target Probes

The active PDV probe is a pigtail style collimator for 1550 nm with a 1.4 mm aspheric lens manufactured by OZ Optics. The two passive TPDV probes are pigtail style collimators for 1550 nm with a 6.2 mm aspheric lens manufactured by OZ Optics. The TPDV probes have a wider lens than the PDV probes to capture more light from the displacing target.

Platform Optical Mount, 0.5 in., ±11° Hex Adjustment, 4-40 were obtained from Newport Corporation. A 4 mm hole was drilled into the PDV mount and an 8 mm hole was machined into the two TPDV mounts. The probes were inserted into the holes of their respect holders (Figure 3.8).

A probe holder was designed by Christian Kettenbeil to contain the probe-mount assembly (Figure B.2). The probe holder was designed to capture the 1^{st} order diffracted beams at angles of ±38.32° while minimizing the distance between the probe lenses and the backside of the target. The probe holder was additive manufactured from Rigur RGD450 simulated polypropylene using stereolithography.

The active probe-stage assembly was slid into the normal PDV probe slot. The two passive probe-stage assemblies were slid into the two angled TPDV probe slots. The case to probe holder is press-fit into place to seal the probes inside (Figure 3.9).

3.3 Powder Gun Implementation

Powder Gun Overview

The Guggenheim Aeronautical Laboratory at the California Institute of Technology (GALCIT) plate impact system is a simple breech-loaded single-shot smooth-bore cannon (Figures 3.10 and 3.11). A solenoid firing pin sparks an ignition charge (Figure 3.12). The flames from the ignition charge are fed into a manifold flame splitter which ignites the main charge. When a critical pressure is reached, the sealing cap breaks free and the sabot and flyer plate accelerate down the barrel to the target plate. A key way in the barrel and a key on the sabot prevent the sabot from rotating. This powder gun is designed for sabot velocities between 450 m/s and 1800 m/s.

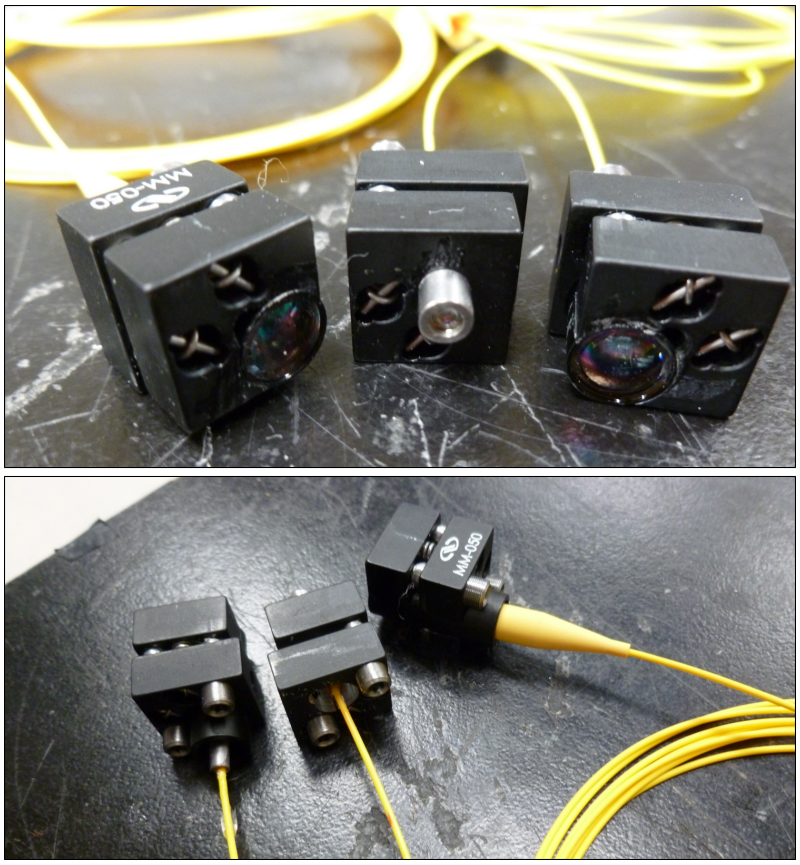

Figure 3.8: The TPDV probes (left and right) and PDV probe (center) in their mounts.

The flyer plate impacts the target plate and crushes the shorting pins. A combined photonic Doppler velocity (PDV) and transverse photonic Doppler velocity (TPDV) interferometer affixed to the backside of the specimen holder monitors the displacement of the backside of the target. The crushing of the shorting pins triggers PDV-TPDV data collection on the oscilloscope. The flyer plate, target plate, and PDV-TPDV assemblies are destroyed during each shot cycle (Figure 3.13).

Experiment Configuration

Sabot A sabot serves as the main projectile and carries the flyer plate (Figure B.1). The sabot is machined from a 1-1/2 inch diameter Slippery Nylon (molybdenum disulfide filled Nylon) Rod obtained from McMaster-Carr and has a slot for for a 3D printed press-fit key that aligns with the barrel's key way. The sabot is pulled through the barrel starting from the exit end in the impact chamber using fishing line to ensure that it will slide through while maintaining an air-tight seal. Adjustments are made to the sabot and key as necessary with sand paper and files. A cylindrical

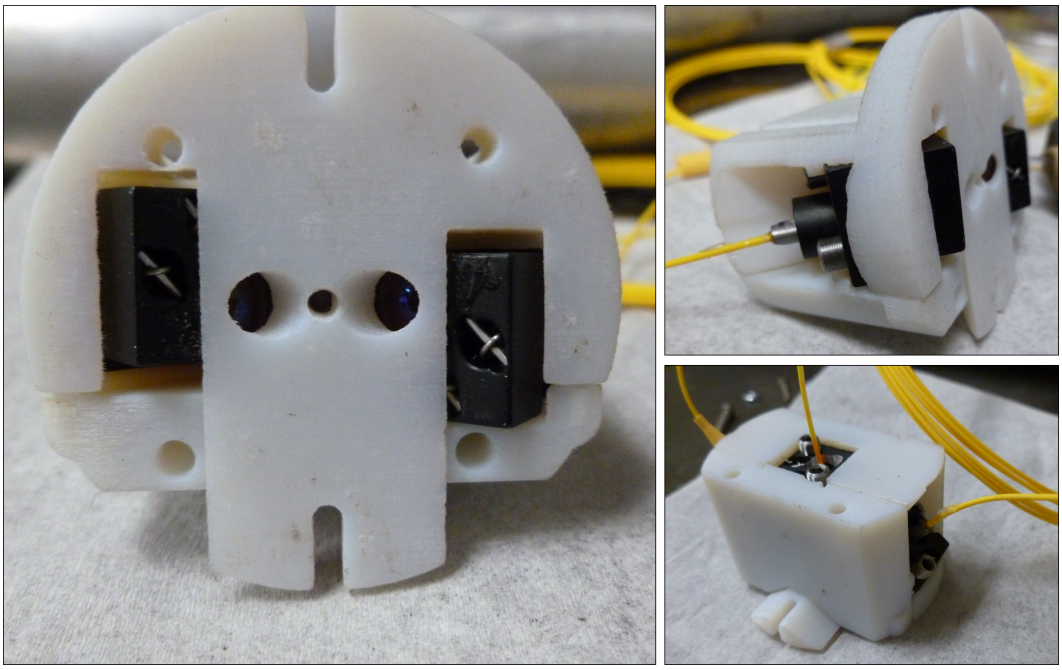

Figure 3.9: Probe holder assembly with probes and mounts.

bar of metal is epoxied into the hollowed out center of the sabot using Gorilla two-part Epoxy (Figure 3.14). The metal bar increases the sabot's mass which decreases the flyer plate's impact velocity. The sabot is pulled through the barrel again using fishing line to check the fit.

Once the fit has been checked, the flyer plate is epoxied into place with Gorilla two-part Epoxy (Figure 3.15). Epoxy is applied to back face and diameter of the flyer plate and excess squeeze out is cleaned off with acetone. A weight is placed on top of the flyer plate while the epoxy cures.

A small piece of copper shim is glued to the outer edge of the sabot. The copper provides a reflective surface to measure the sabot's down barrel velocity. The complete sabot-flyer plate assembly is inserted into the barrel's exit end in the impact chamber.

Target A specimen holder designed by Christian Kettenbeil is machined from Delrin. PMMA arms are cut and press-fitted into holes drilled into the side of the holder. The target plate's grating is aligned within the specimen holder such that light diffracts in the horizontal direction. This is accomplished with an alignment system designed by Christian Kettenbeil (Figure 3.16). Once the target plate is aligned in the holder, the target is epoxied into place with Gorilla two-part Epoxy

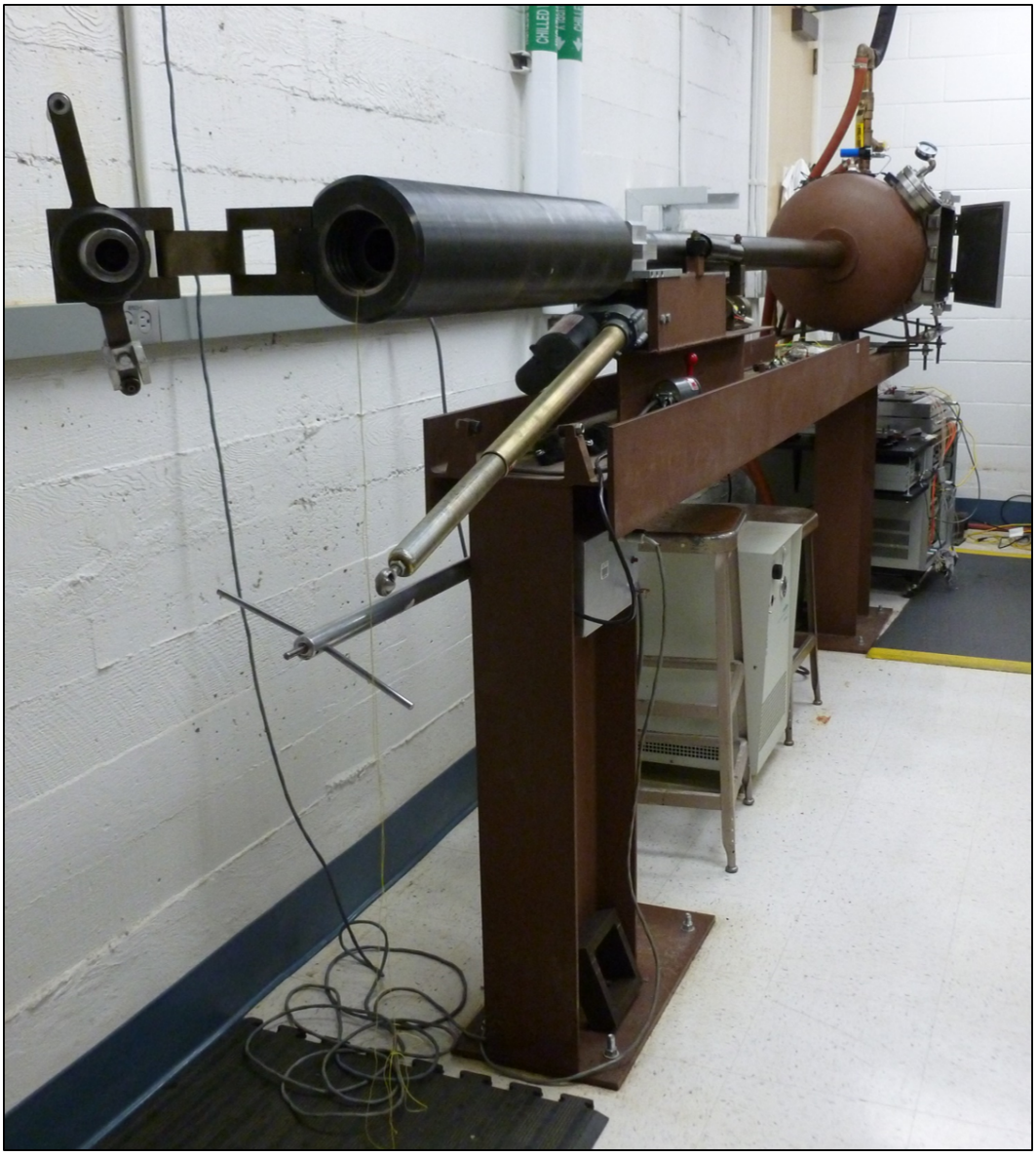

Figure 3.10: GALCIT plate impact system.

(Figure 3.17). Epoxy is placed in a thin line around the outer edges of top and bottom face of the target plate where it makes contact with the holder. Excess epoxy is cleaned off with acetone.

The probe holder is placed on the back of the specimen holder perpendicular to the grating lines. The probe holder is screwed into the specimen holder. The probes in the probe holder are connected to a 2287/21 ORL-55 SmartClass Optical Return Loss Meter manufactured by JDSU, a SmartPocket OLP-34 Optical Power Meter manufactured by JDSU, and a JW3208 Handheld Optical Power Meter manufactured

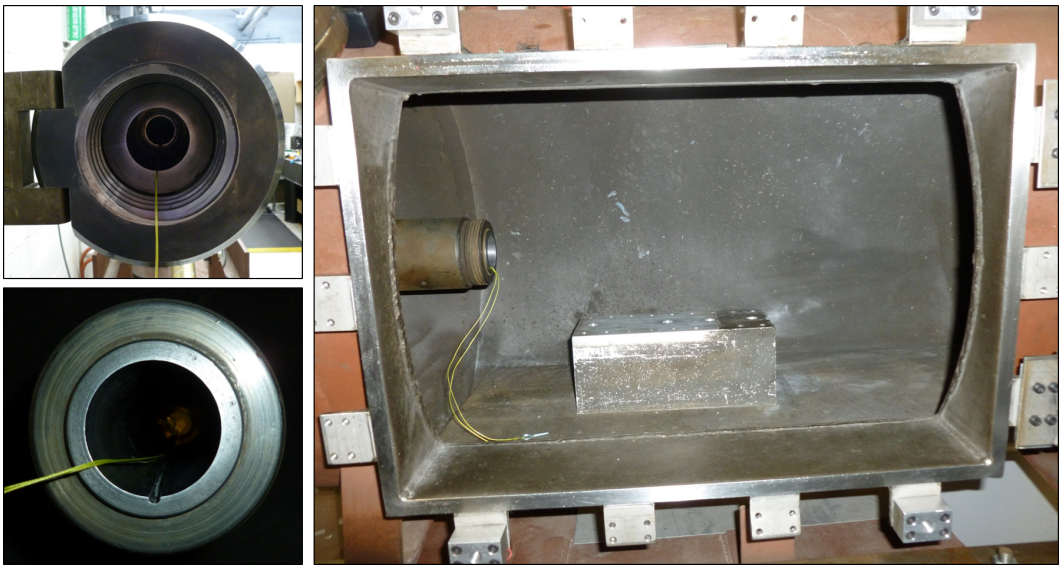

Figure 3.11: GALCIT plate impact system breech (upper left), barrel exit with key way (lower left), and impact chamber (right). Fishing line is used to pull the sabot through the barrel and check the sabot's fit.

by JoinWit. The laser source shines a light on the grating, which reflects light back to the probes. The power in the probe's return is measured by the power meters. Returns for these experiments are found in Table (3.7). The screws in the probe mounts are adjusted to maximize the probes' returns. Typical return values are -20 dBm to -15 dBm. Once the returns are maximized, Gorilla two-part Epoxy is placed over the tops and edges of the probes to keep them in place (Figure 3.18).

Center (PDV) probe	Side (TPDV) probes
6.5 – 8.5 dB	−19 – −20 dBm

Table 3.7: Light return specifications to target probes.

A flat, planar mirror is attached to the topside of the target. This mirror is larger in diameter than the target plate and will provide a ledge to align the shorting pins. The mirror is placed face down on a hard surface. The brass casing and copper wires of four shorting pins are soldered to eight wires of an ethernet cable (Figure 3.19). The shorting pins are then pushed into the specimen holder such that they are aligned with the target plate's topside and flush with the mirror surface (Figure 3.20). A down barrel probe manufactured by AC Photonic, was also pushed into the specimen holder. The shorting pins and down barrel probe are glued into place using M-Bond 200 adhesive manufactured by Vishay Precision Group.

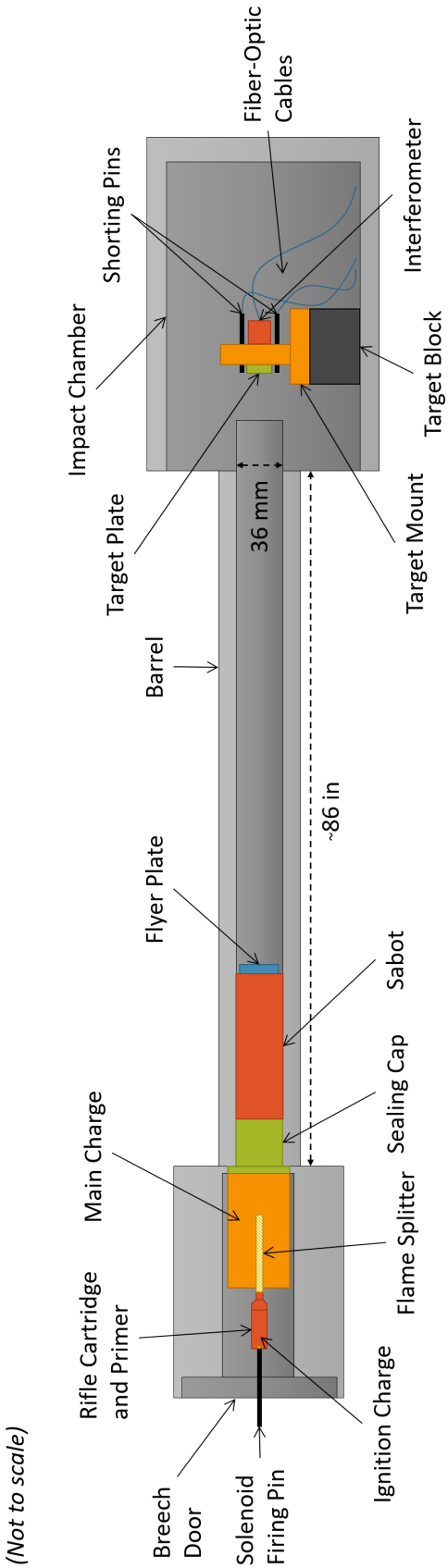

Figure 3.12: GALCIT plate impact system schematic.

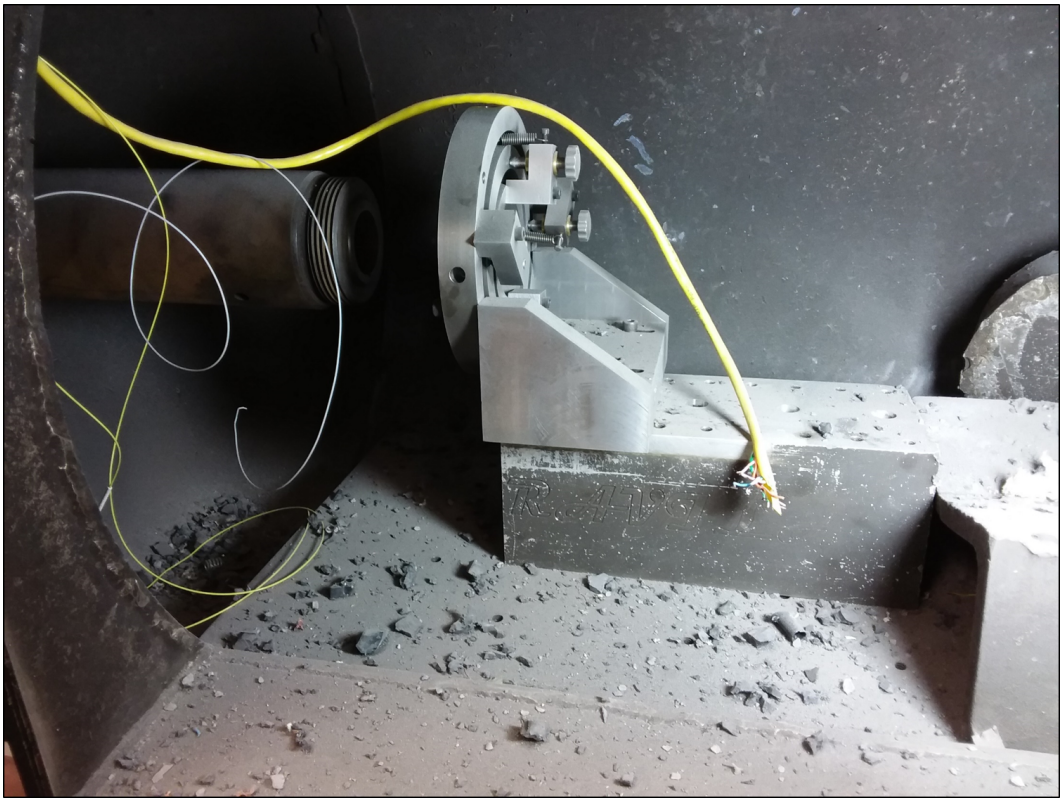

Figure 3.13: Impact chamber debris after an experiment.

The entire specimen assembly is placed into a gyroscopic target holder. Clamps on the gyroscopic target holder hold the specimen holder's arms in place. This mount is screwed into a target block inside of the impact chamber. The fiber-optic cables connected to the probes and the ethernet cable attached to the shorting pins are run through holes in the vacuum flange. Plumber's putty is used to seal the gap between the cables and vacuum flange.

Alignment The impact surfaces of the flyer plate and target plate are aligned perpendicular to the velocity of the flyer plate. Planar alignment is accomplished with an optical technique developed by Kumar and Clifton [57]. A MRA-50 Autocollimator manufactured by Micro-Radian Instruments is used to analyze light reflected through a prism from mirrors rubber banded to the impact surface of the flyer and target plates (Figure 3.23). With this technique, tilt at the beginning of the experiment is minimized to approximately 25 microrad.

Figure 3.14: A metal insert (left) and sabot (right) with key.

Firing

The sabot-flyer plate assembly is pulled back into place at the front end of the barrel using a fishing line. A sealing cap is glued to the back of the sabot. The sealing cap has a flange that rests on the barrel's inner shelf (Figure 3.24). This sealing cap holds the sabot in place during firing until main charge's combustion builds up a critical pressure behind the sealing cap. The fishing line is removed and a small metal tab is glued over the hole in the sealing cap with M-Bond 200 adhesive.

The shorting pins are tested to ensure that they are triggering the oscilloscope. High Vacuum Grease manufactured by Dow Corning is applied to the seal on the impact chamber door. The chamber door is gently shut and parallel bars are screwed into place over the door (Figure 3.25). The impact chamber is evacuated to a vacuum of 1-2 Torr using a DuoSeal 1376 Vacuum pump manufactured by Welch. The vacuum environment prevents air resistance from interfering with the sabot's acceleration and affecting the alignment of the target prior to impact.

The charge is prepared (Figure B.3). The holes in the flame splitter are covered with masking tape to prevent rifle powder from pouring into the holes (Figure 3.26).

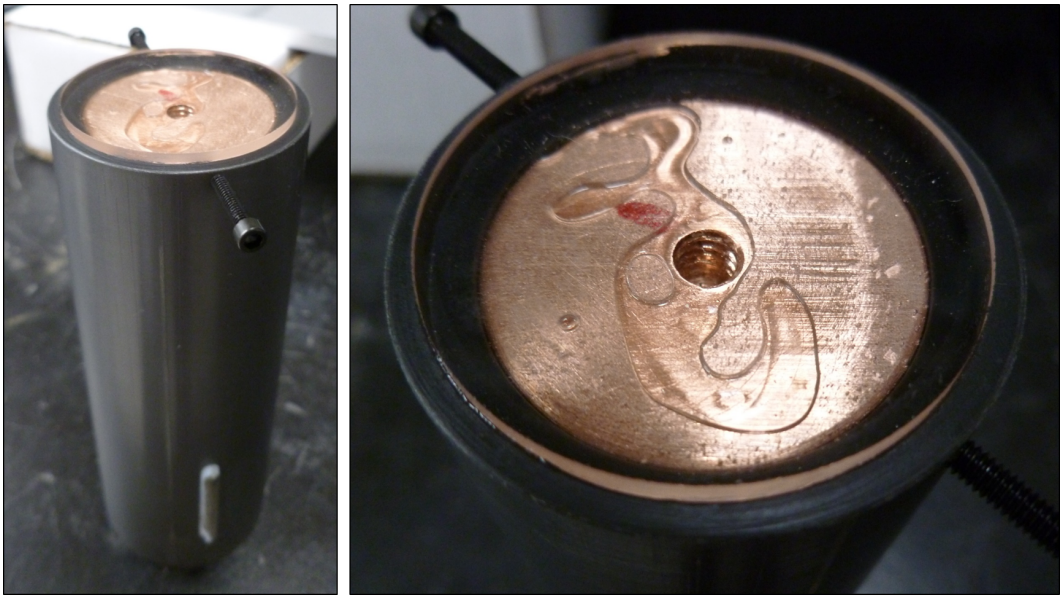

Figure 3.15: A flyer plate is epoxied into a sabot with a metal insert.

Approximately 5 g of Hodgdon's H4198 Rifle powder are poured around the flame splitter. The powder is tamped down with a Kimwipe. The Kimwipe in the flame splitter assembly to hold the powder in place. The velocity of the sabot is controlled by varying the amount of rifle powder in the main charge. If too much rifle powder is used, then the powder will continue to burn after the the sabot has broken free and the sabot will continue to accelerate prior to impact. Too much rifle powder may also result in chamber over-pressurization. This small amount of rifle powder was intended to produce an impact velocity of 200 m/s, which very low for this powder gun system.

A .30-06 Springfield rifle cartridge manufactured by Winchester is filled with approximately 3 g of 2400 of smokeless magnum handgun powder manufactured by Alliant Powder. The powder is tamped down with a Kimwipe and the Kimwipe is left in place to hold the powder down. The rifle cartridge is placed in the base of the flame splitter. The flame splitter assembly is screwed onto the breech door and slid into the breech (Figure 3.27). The breech is closed. A solenoid triggering device manufactured by Guardian Electric is mounted on the back of the breech (Figure 3.28).

The driver laser is turned on 30 minutes prior to the start of the experiment to warm up. A few seconds before the start of the experiment, the interferometer is turned on and light enters the PDV-TPDV system. If light is beamed onto the target for

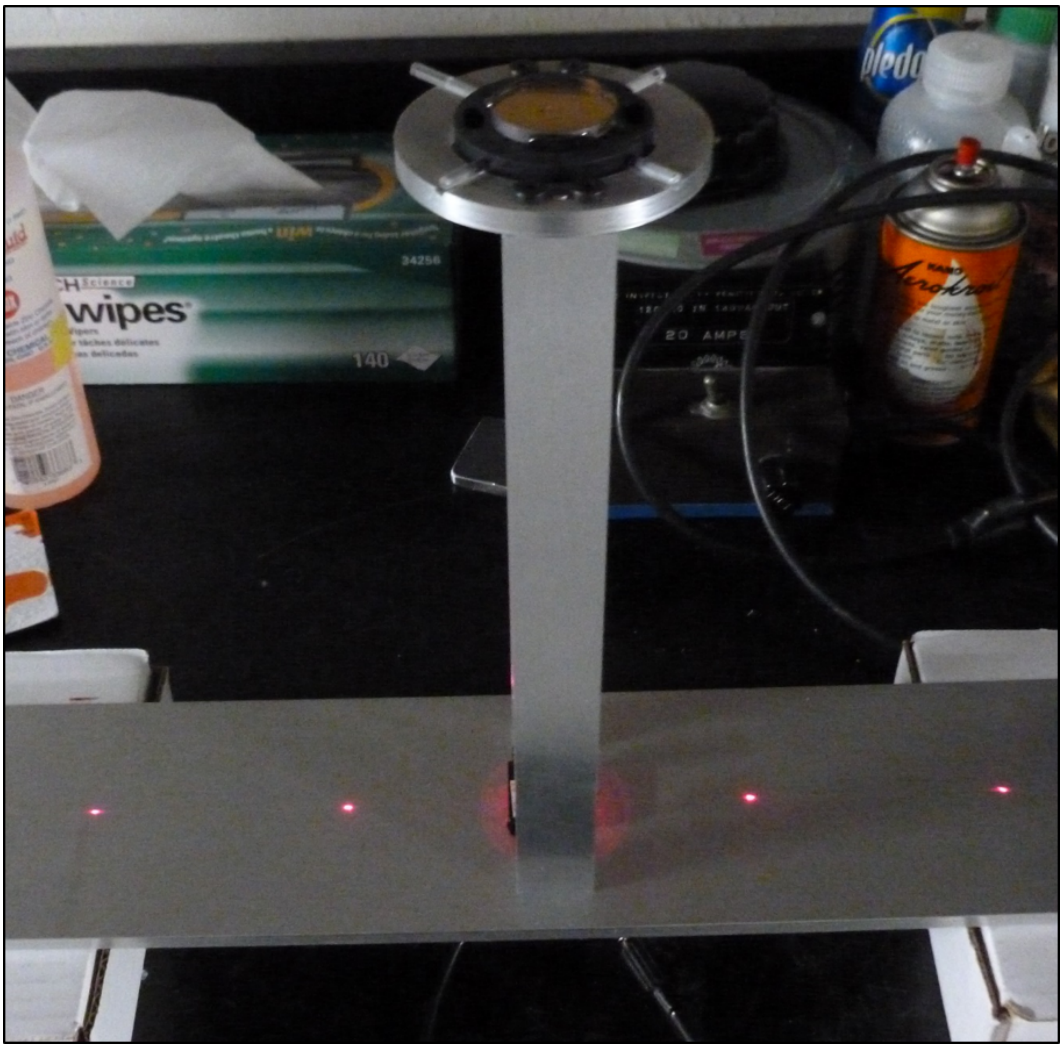

Figure 3.16: A target plate's grating is aligned in a specimen holder by lining up the red diffracted beams of light along a line machined in the alignment device's base (left). This process orients the grating (and the quartz's x-axis) parallel to the specimen holder's upwards direction.

too long, then the grating on the back of the target may be scorched. The red firing button is pressed on the firing box to run the experiment (Figure 3.29).

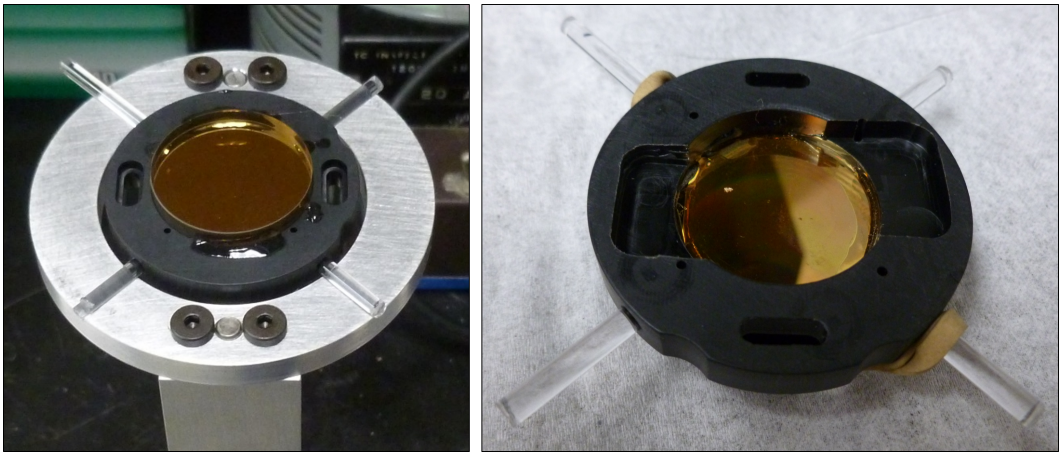

Figure 3.17: A target plate is epoxied into a specimen holder along its topside (left) and backside (right).

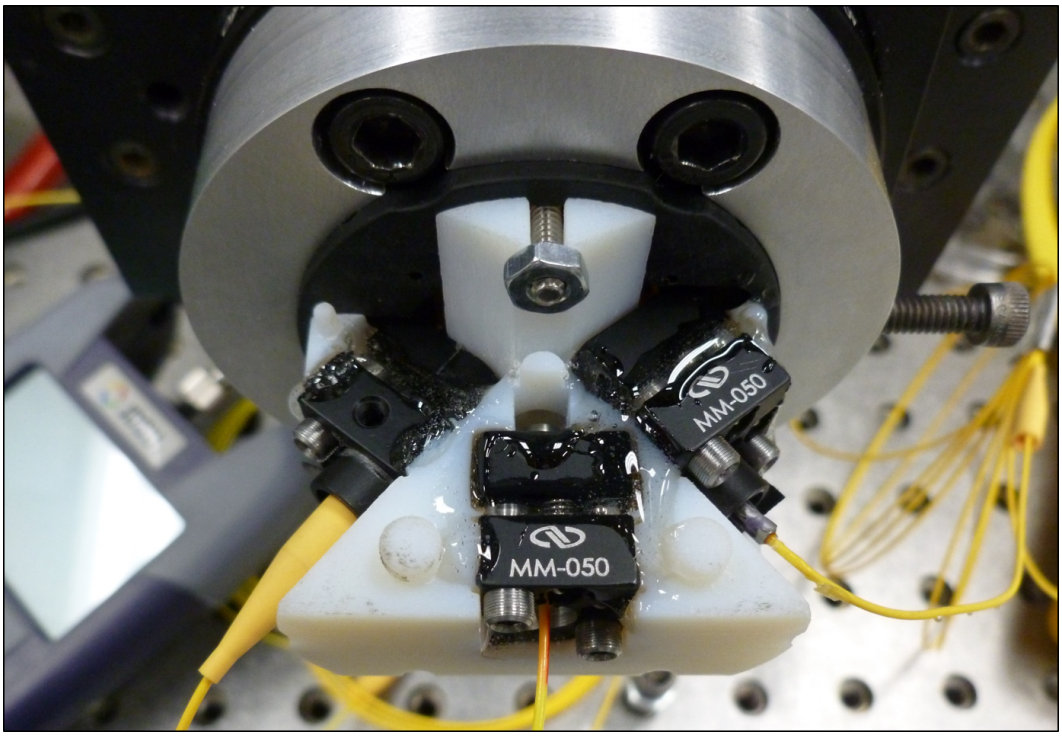

Figure 3.18: Probes are adjusted to maximize return and then epoxied into place.

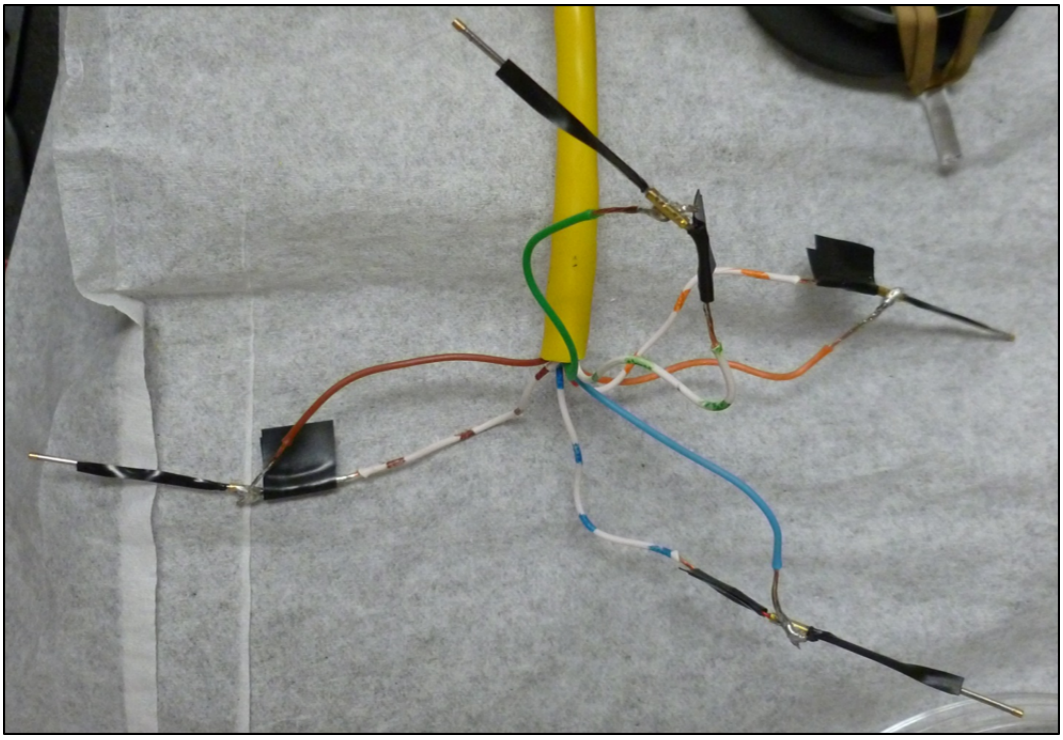

Figure 3.19: Shorting pins soldered to an ethernet cable.

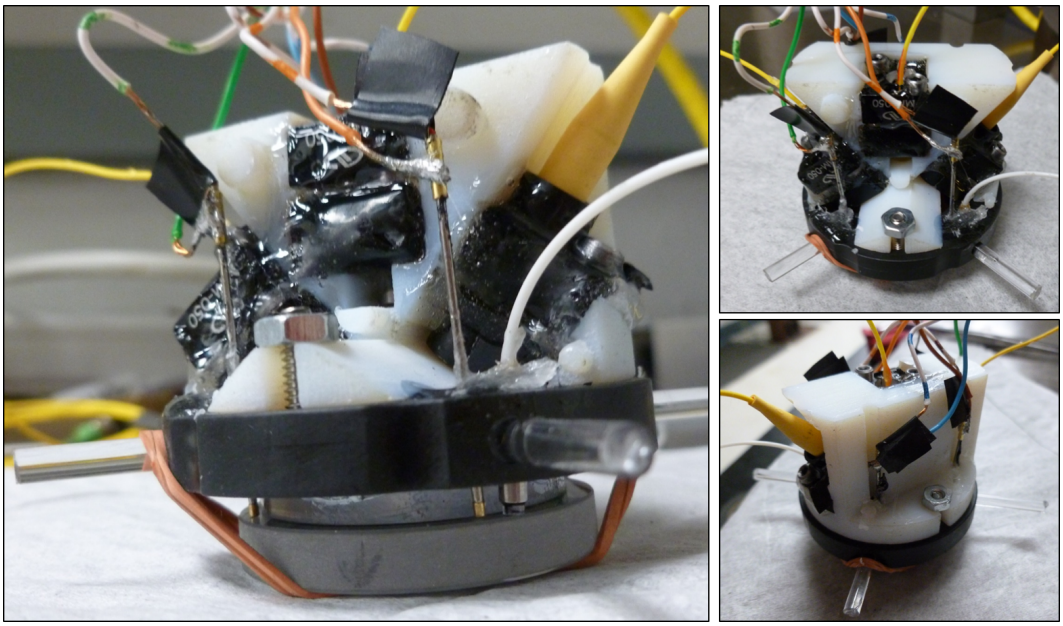

Figure 3.20: Shorting pins are glued into place such that they are planar with the topside of the target plate. This is accomplished by pushing the target pins against a flat common surface.

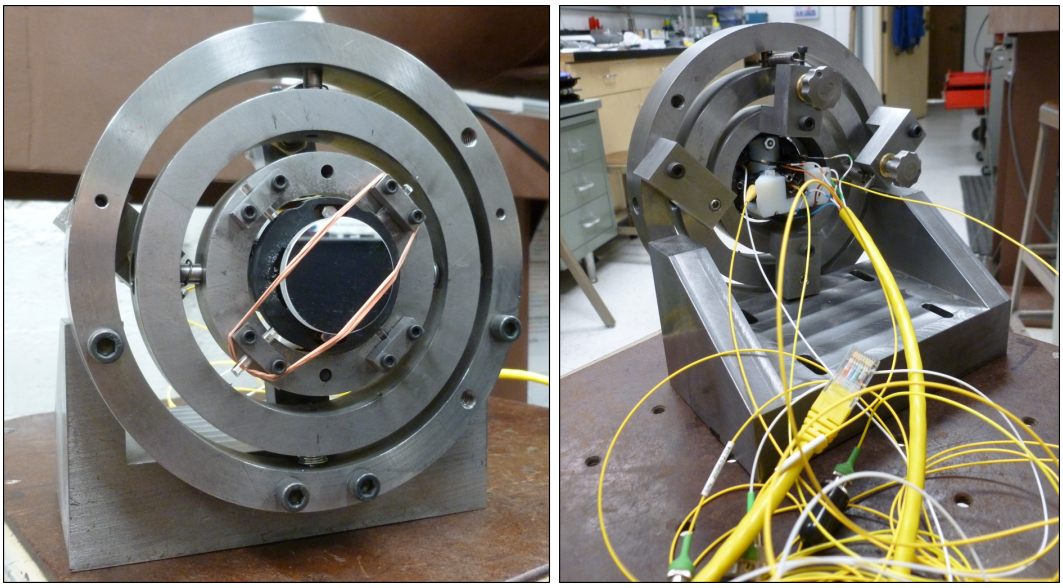

Figure 3.21: Gyroscopic target holder holding the specimen assembly.

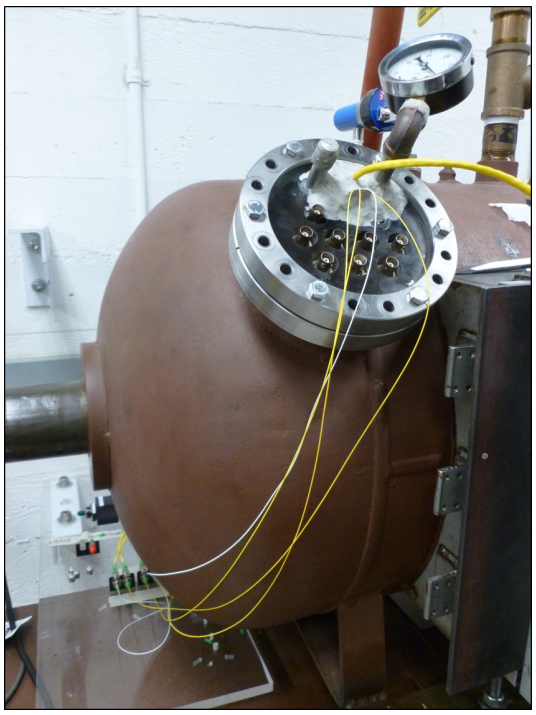

Figure 3.22: Cables inside the impact chamber run through the vacuum flange and are sealed with putty.

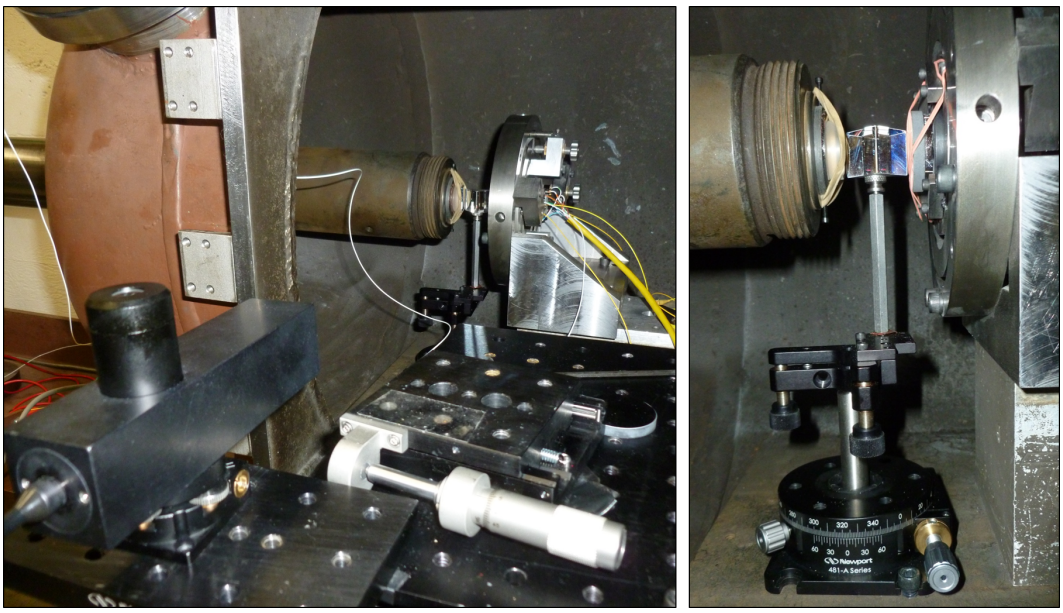

Figure 3.23: An autocollimator (left) analyzes light from a prism to align the mirrors on the flyer and target plates (right).

Figure 3.24: A sealing cap with a key and flared end.

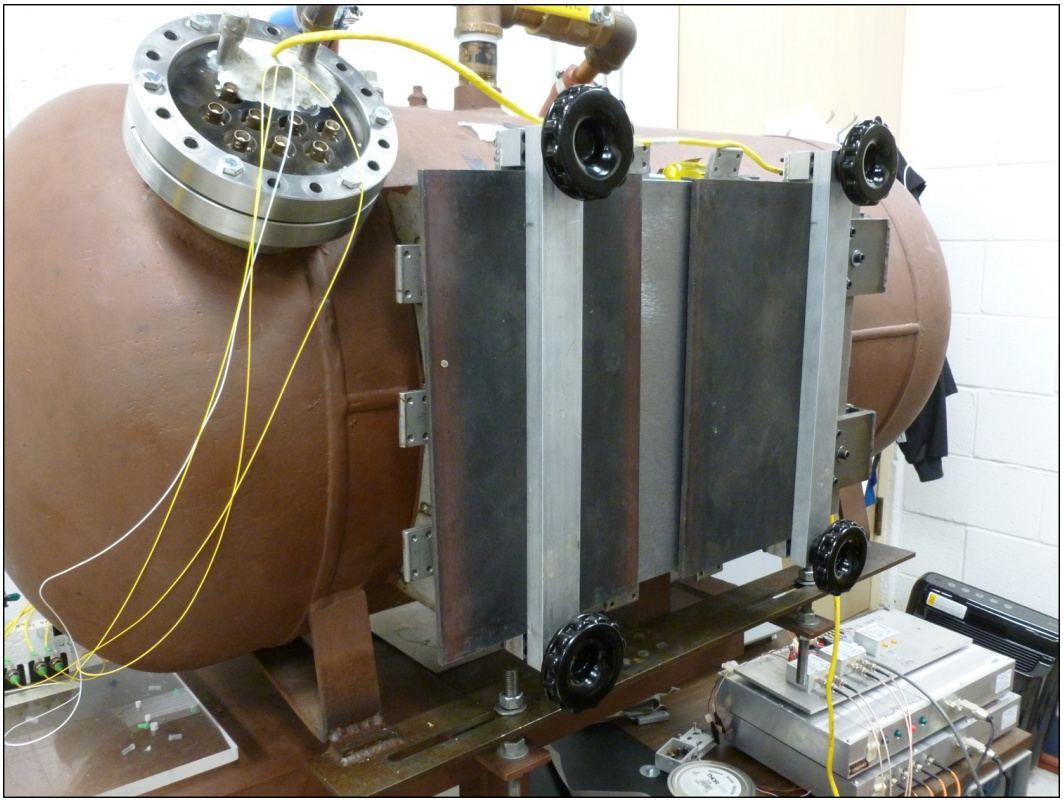

Figure 3.25: The impact chamber is sealed with two metal bars clamping the door shut.

Figure 3.26: A rifle cartridge, flame splitter, and case (left). The rifle cartridge is housed at the base of the splitter (upper middle) and the case is screwed into place around the splitter (lower middle and right).

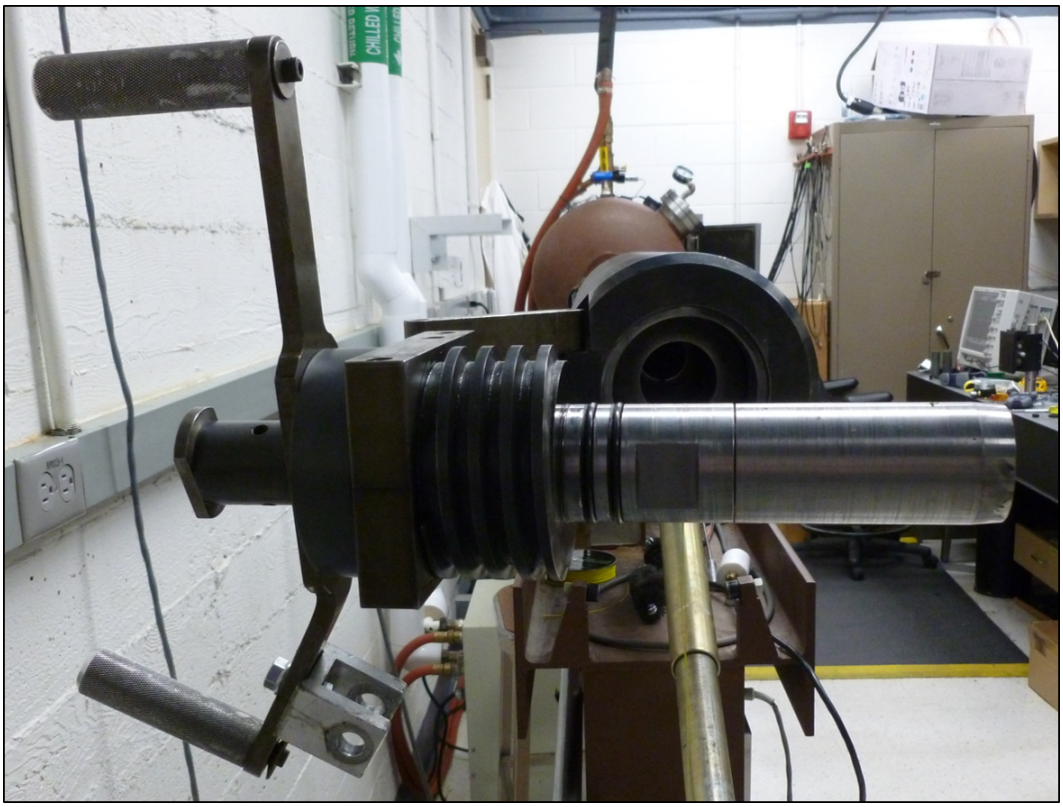

Figure 3.27: A flame splitter in the breech door.

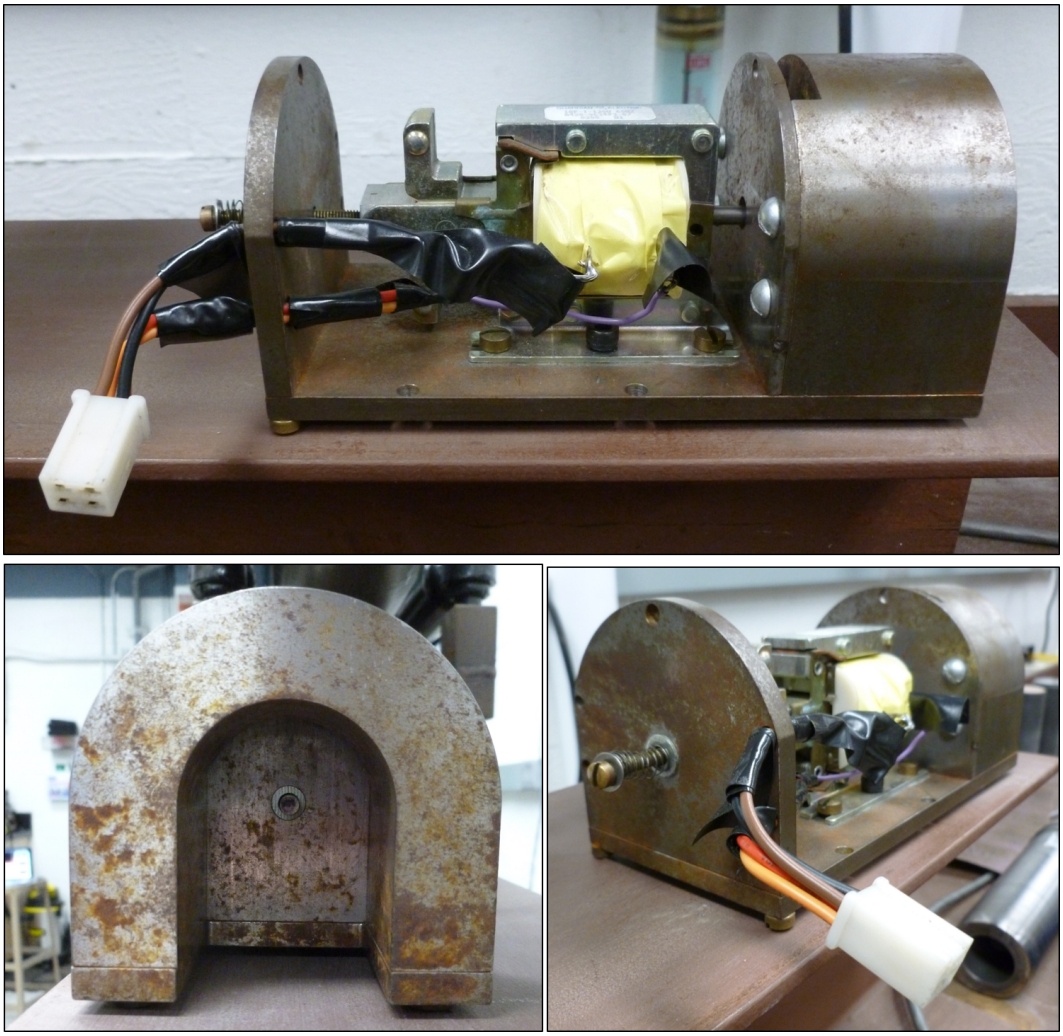

Figure 3.28: Solenoid triggering device.

Figure 3.29: Firing box with red firing button.

Chapter 4

RESULTS

4.1 Signal

Photonic Doppler velocimetry (PDV) and transverse photonic Doppler velocimetry (TPDV) data were gathered from the oscilloscope. One of the two TPDV probes malfunctioned during experimentation. However the oscilloscope traces for the sabot and remaining PDV-TPDV probes were typical of a plate impact experiment (Figures 4.1, 4.2, and 4.3). Zooming in on the trace shows distinctive fringes and sinusoidal oscillations (Figure 4.4). The four shorting pins were crushed at -0.3068 μs, -0.2683 μs, 5.5622 μs, and 0.4657 μs respectively.

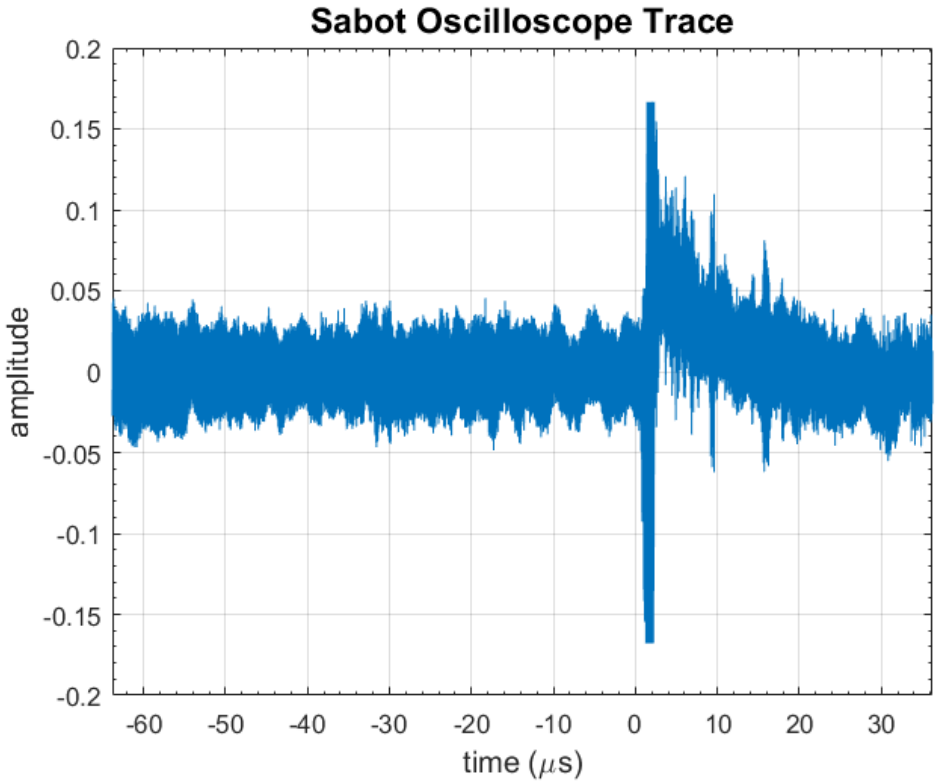

Figure 4.1: The oscilloscope trace for the sabot.

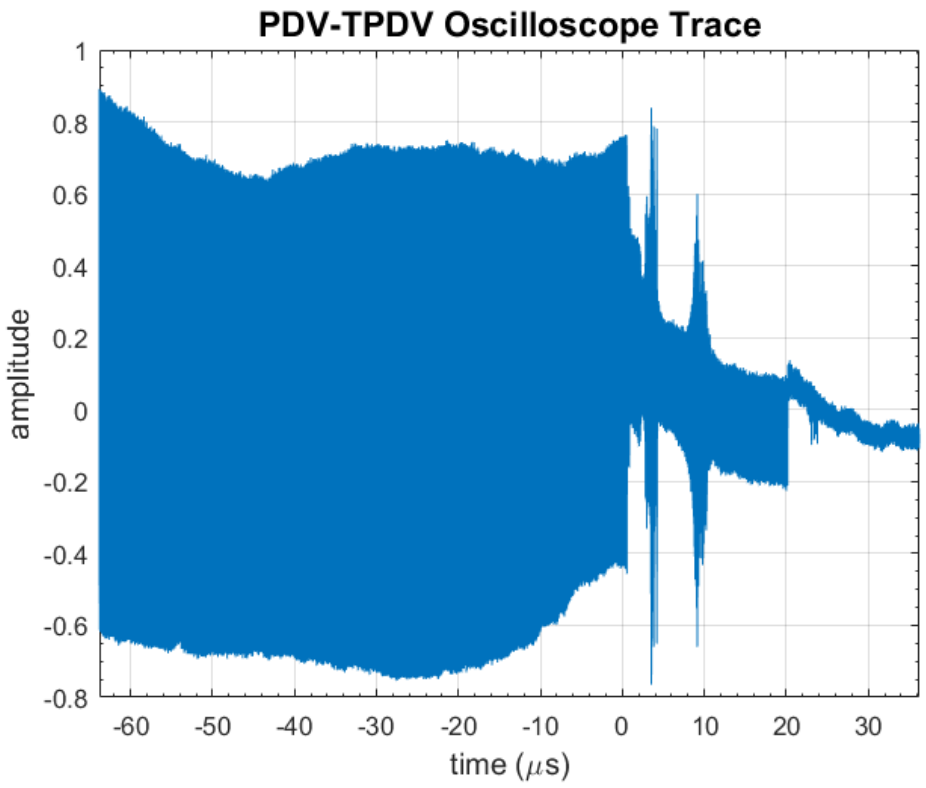

Figure 4.2: The oscilloscope trace for the target plate.

4.2 Free Surface Velocity

Spectrogram

The sabot (down barrel) and PDV-TPDV oscilloscope traces were snipped into three smaller signals and the starting time of the snipped signal was adjusted to zero. Each snipped signal was decomposed into spectrograms of frequency against time using a variety of short time fourier transform (STFT) and discrete Fourier transform (DFT) parameters. Dominant frequencies in the spectrogram are colored bold yellow while weaker frequencies are colored dark blue.

The sabot spectrogram displays two dominant frequencies (Figure 4.5). These strong frequencies are attributed to the sabot's relatively constant velocity and strong light returns to the down barrel probe. The lower frequency band around 0.66 GHz is the signal's carrier frequency. The second frequency band around 0.94 GHz is the upshifted frequency that contains the sabot's velocity information.

The PDV spectrogram also displays a dominant carrier frequency around 0.66 GHz that branches to higher frequencies upon arrival of the quasi-longitudinal (QL) wave around 0.54 μs (Figure 4.6). There is a second frequency increase around

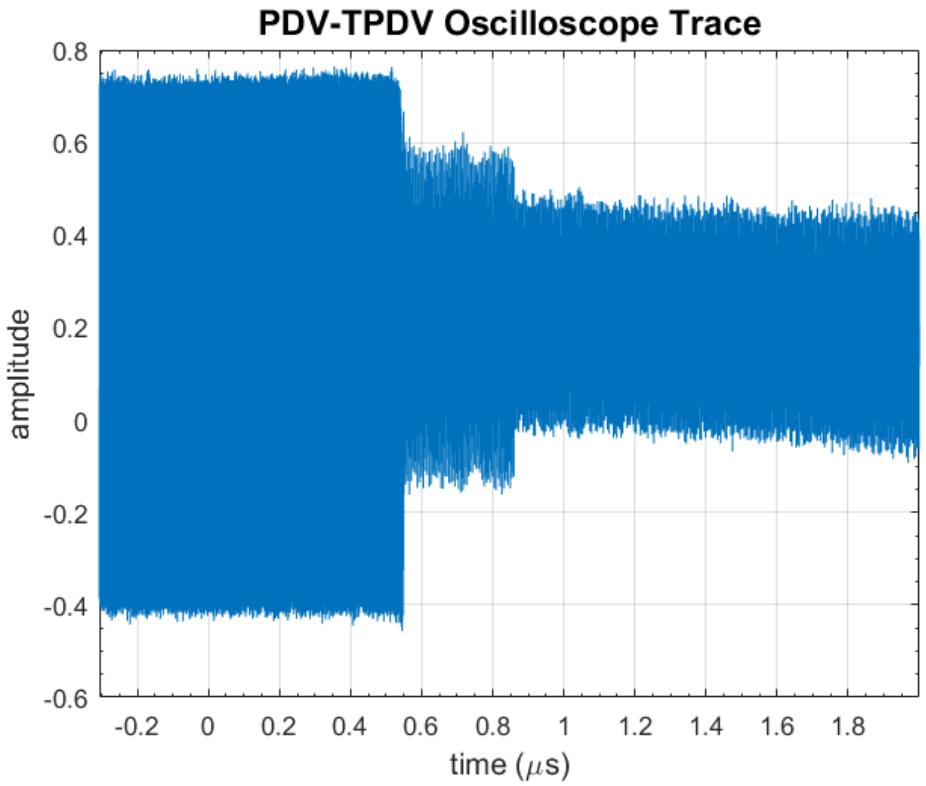

Figure 4.3: The oscilloscope trace for the target plate displays changes in amplitude upon arrival of waves to the free surface as well as amplitude tapering over time.

0.86 μs upon arrival of the quasi-transverse (QT) wave. The lower frequency band containing frequencies between 0.62 and 0.72 GHz was filtered out after the first branch (Figure 4.7). At small window sizes, the lower and upper frequency bands broaden and can bridge together across the frequency gap. Filtering prevents the lower band from bridging and interfering with identification of the dominant frequency caused to longitudinal displacement in the upper band.

The TPDV spectrogram displays similar characteristics to the PDV spectrogram (Figure 4.8). However, when the target plate's surface displaced, the amount of light received by the TPDV probe decreased at a faster rate than that of the PDV probe. This resulted in a weaker TPDV signal.

Velocity

Each signal's dominant frequencies were found at each window's time center using power distributions (Figure 4.9). The initial frequency search range was chosen by visual observation of the frequency bands. The median frequency was found within this search region. Then the frequency search band was narrowed to ±0.15 GHz

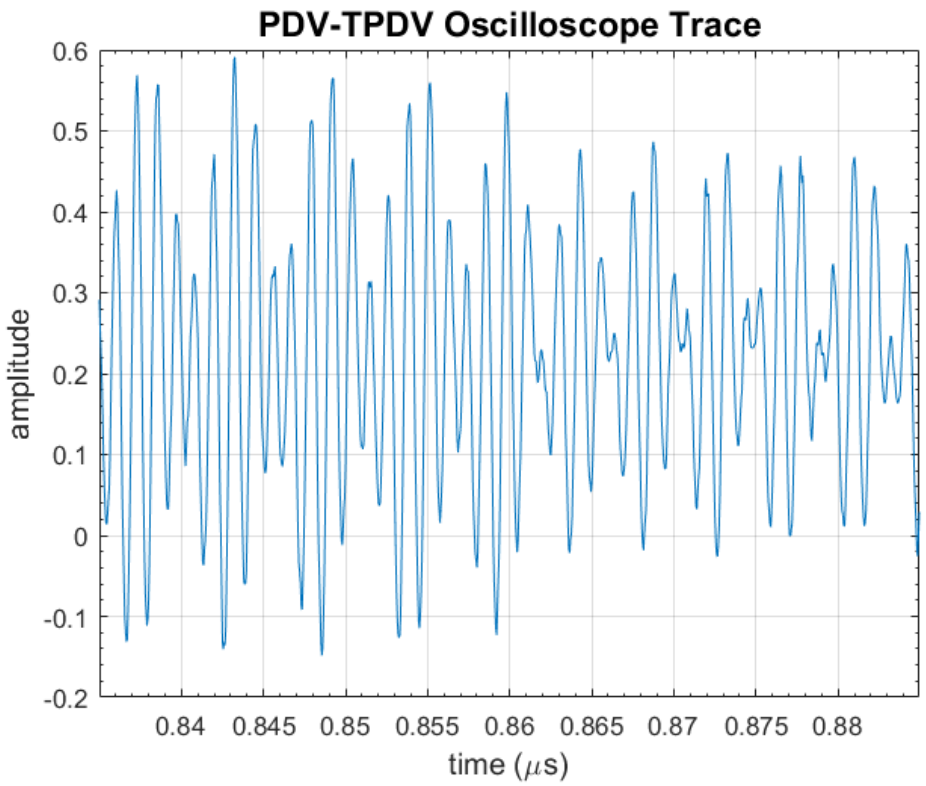

Figure 4.4: Distinct fringes and oscillations are seen in the oscilloscope trace when zoomed in to a 50 ns window.

around the median frequency and the maximum frequency was found within the narrowed search region. Initially, the peaks in the power distributions at each time center were found using a Guassian fitting method [38]. Unexpectedly, Matlab's `fit` function using Guassian parameters found the same maximum in the power distribution as Matlab's `max` function [58, 59]. Since the `max` function runs faster than a Gaussian `fit`, the `max` function was used to determine the dominant frequencies of these large data sets.

These dominant frequencies were used to calculate the sabot's velocity and the target plate's free surface velocities. The sabot velocity was found to be 212 m/s by taking the negative of (2.105). Using this sabot velocity, the target plate's particle velocities and stresses were predicted from elastic-wave theory assuming a no-slip boundary condition (Figures 4.10, 4.11, and 4.12) (Section 2.2). These predictions may not match observations from an ideal experiment since the elastic constants in Tables (3.2) and (3.4) used for these calculations were not obtained under impact conditions.

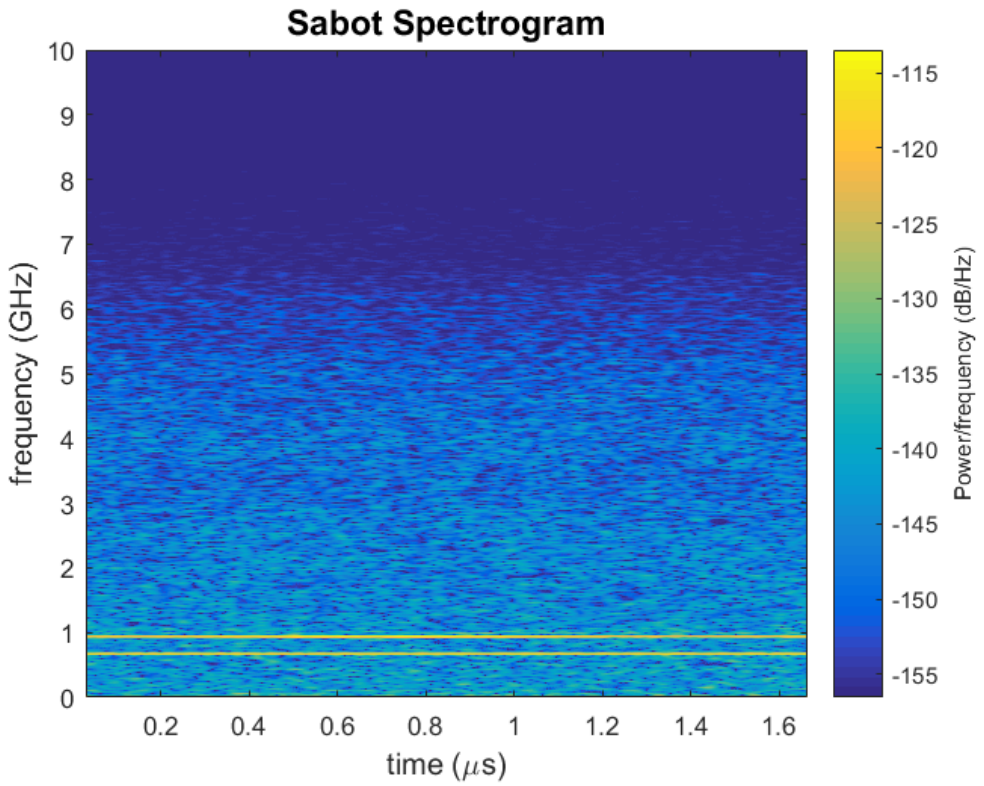

Figure 4.5: A spectrogram of the sabot (down barrel) signal shows a strong carrier frequency around 0.66 GHz and a relatively constant frequency around 0.94 GHz. STFT specs.: Hamming window, 200 ns window length, window shifted by 2 samples, 2^{10} DFT points.

A modified procedure was used to calculate the longitudinal and transverse target free surface velocities. The longitudinal velocity was calculated by taking the negative of (2.105)

$$\dot{u}(t) = \frac{\lambda_0}{2}\left(f_{\mathrm{PDV}} - f_C\right) \tag{4.1}$$

where $\lambda_0 = 1550.012$ nm is the probing wavelength, f_{PDV} is the PDV frequency, and f_C is the carrier frequency. The loss of a TPDV probe resulted in a signal loss associated with either f_+ or f_-. Since (2.121) and (2.122) are equivalent after accounting for the sign of $\sin\theta_n$, the transverse velocity was calculated using a variant of (2.121)

$$\dot{v}(t) = \frac{1}{\sin\theta_1}\left(\lambda_0\left(f_{\mathrm{TPDV}} - f_C\right) - \frac{\lambda_0}{2}\left(f_{\mathrm{PDV}} - f_C\right)\left(1 + \cos\theta_1\right)\right) \tag{4.2}$$

where $\theta_1 = 0.6687$ radians and f_{TPDV} is the TPDV frequency.

For small window sizes, the resulting velocities are fairly noisy (Figure 4.13). Lightly smoothing the data reveals that the data tends to fluctuate around values close to

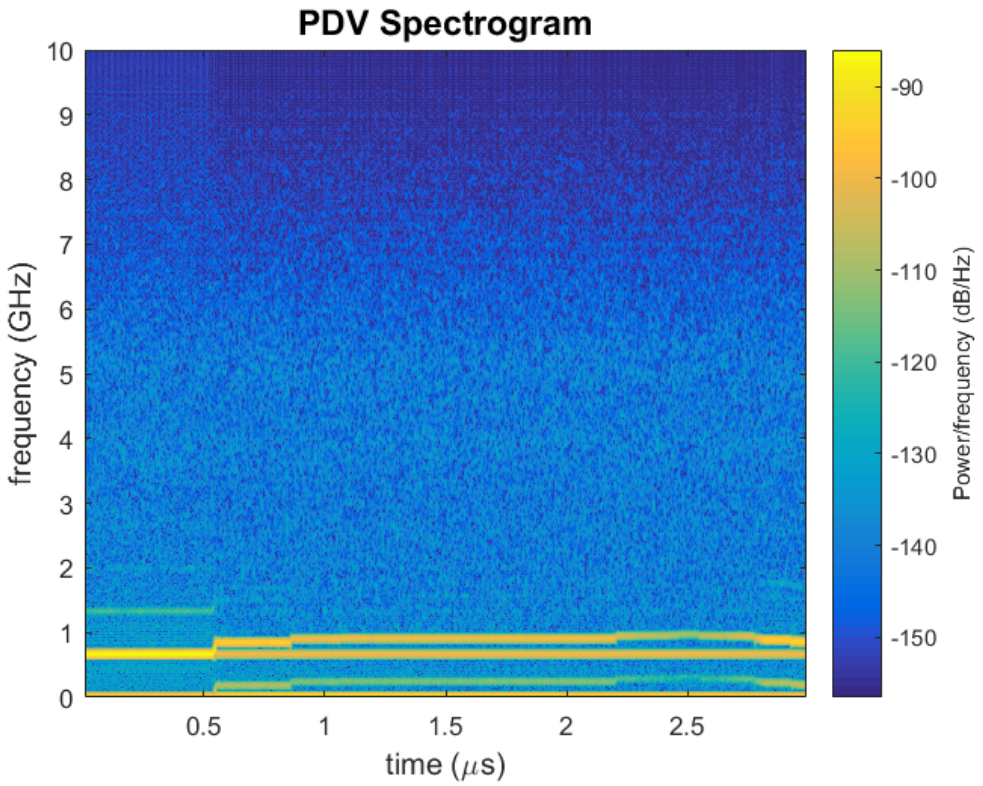

Figure 4.6: A spectrogram of the PDV signal shows a strong carrier frequency around 0.66 GHz. The QL wave arrives at the backside of the target around 0.54 μs and the QT wave arrives at the backside of the target around 0.86 μs. STFT specs.: Hamming window, 20 ns window length, window shifted by 1 sample, 2^{11} DFT points.

those predicted (Figure 4.14). The longitudinal velocity undershoots the predicted transient value by 11.03 m/s and the final value by 11.12 m/s, while the transverse velocity undershoots the predicted transient value by 0.2 m/s and overshoots the final value by 0.26 m/s. The spike in transverse velocity on the rising edge is believed to be caused by a mismatch in the time lengths of the longitudinal and transverse transient regions. This mismatch may be attributed to the frequency-time trade-off associated with the uncertainty principal (2.134) . Additionally, the arrival times of the QL wave around 0.54 μs and QT wave around 0.86 μs do not correspond to the respective predicted arrival times of 0.83 μs and 1.16 μs. This offset is most likely due to the triggering of data collection around -0.3068 μs when the first shorting pin was crushed.

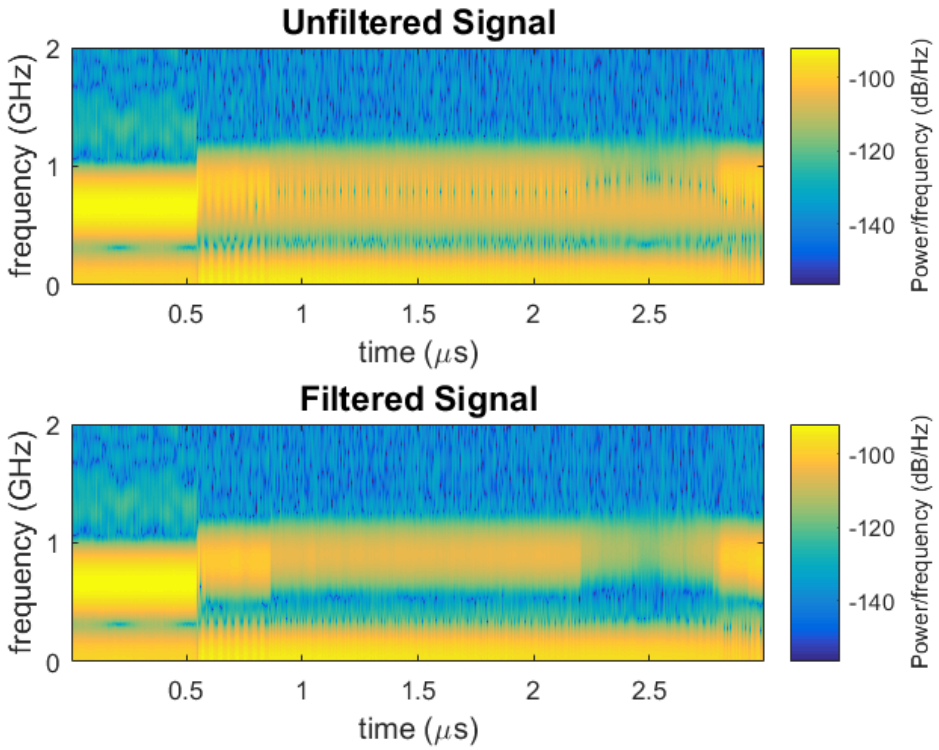

Figure 4.7: When decomposed at small window sizes, the PDV signal's frequencies can blend together. This is visualized in a spectrogram. The carrier band and the band caused by displacement are bridged (top). Filtering out frequencies between 0.62 and 0.72 GHz for times greater than 0.5447 μs prevents bridging (bottom). STFT specs.: Hamming window, 5 ns window length, window shifted by 15 samples, 2^{15} DFT points.

Velocity Uncertainty

The uncertainty of these velocity measurements were calculated from the PDV frequency uncertainty relation (2.139) using additivity of errors [38]. A typical noisy PDV signal to noise ratio, σ, can be taken as 10% [38]. Given a sampling frequency of 20 gigasamples per second, window size of 5 ns, and probing wavelength of 1550.012 nm, the predicted velocity uncertainty Δv is 1.2 m/s for the PDV measurement and 2.4 m/s for the TPDV measurement. In comparison, for a larger window size on 50 ns, the predicted velocity uncertainty is 0.04 m/s for the PDV measurement and 0.08 m/s for the TPDV measurement.

These uncertainties likely underestimate the measurements' errors. Overlaying the smoothed data with the un-smoothed data shows that fluctuations are on the order of several meters per second for the longitudinal velocity and hundreds of meters

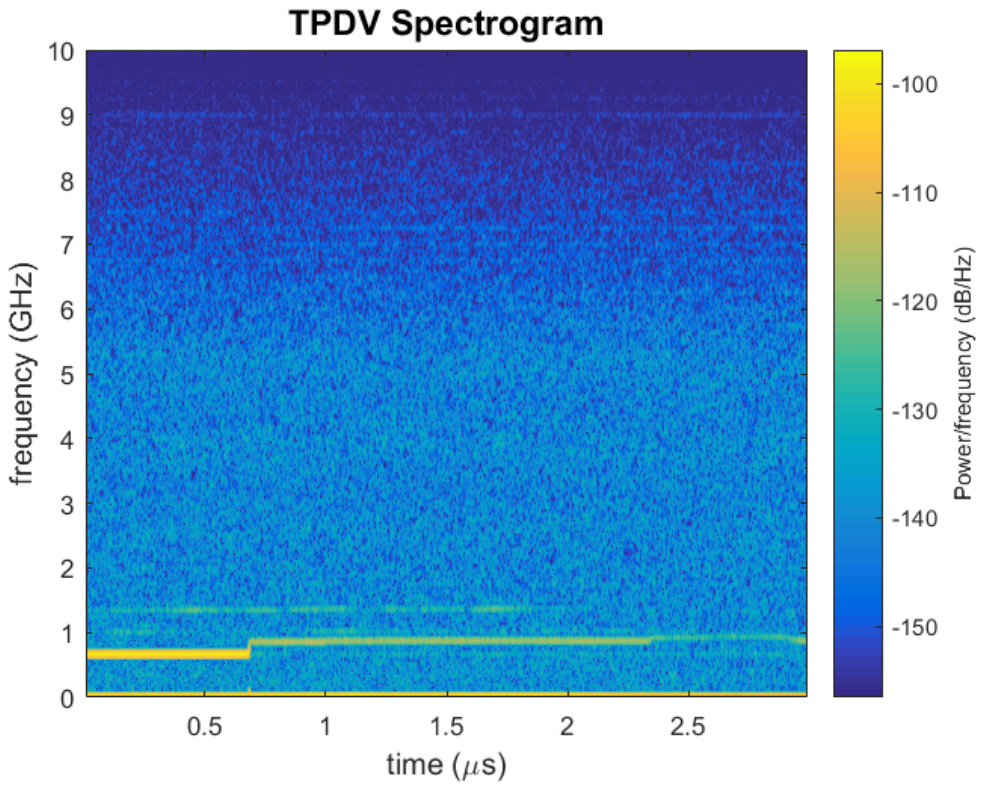

Figure 4.8: A spectrogram of the TPDV signal shows a strong carrier frequency around 0.66 GHz. The TPDV signal was sent through a 4 km delay loop. Therefore the QL wave's arrival time on the TPDV spectrogram does not exactly correspond to that of the PDV spectrogram. STFT specs.: Hamming window, 20 ns window length, window shifted by 1 sample, 2^{11} DFT points.

per second for the transverse velocity (Figure 4.15). This might be caused by a signal-to-noise ratio that is higher than 10%.

Since the uncertainty relation (2.139) shows that error scales inversely with window size, smaller windows are expected to have a higher frequency uncertainty (Figure 4.16). Additionally, because the transverse velocity has greater fluctuations about its mean than that of the longitudinal velocity, a higher TPDV uncertainty is expected. The greater fluctuations in the transverse velocity are most likely caused by the lower amounts of light return to the TPDV probes compared to the PDV probes. Lower amounts of light return are reflected in the power of the TPDV spectrogram compared to the PDV spectrogram. The maximum frequencies in the PDV search region had an average power spectral density of -98.46 dB/Hz while the maximum frequencies in the TPDV search region had an average power spectral density of -111.72 dB/Hz. This means that the PDV signal had about 21 times more power

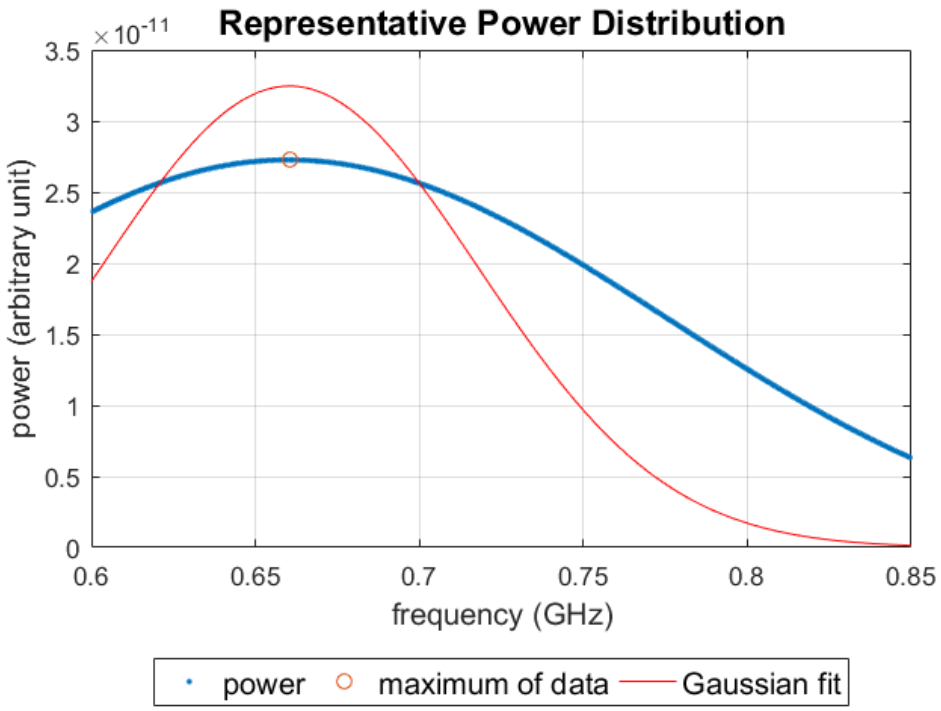

Figure 4.9: A representative power distribution taken from the TPDV signal at 0.0768 μs. The data's maximum corresponds to the peak in the Gaussian fit at 0.6604 GHz. STFT specs.: Hamming window, 5 ns window length, window shifted by 15 samples, 2^{15} DFT points.

than the TPDV signal, and therefore more uncertainty is expected in the transverse velocity.

Rise Time

The 10-90 rise time describes the time needed for the recorded velocity to rise from 10% of the shocked velocity to 90% of the shocked velocity [39]. The ability to resolve the rising portion of the velocity curve depends on a properly sized STFT window. In this case, the rise time is calculated with a shock velocity equal to the average velocity in the transient region. Using a 5 ns window, rise time estimates are 15.75 ns for the longitudinal velocity and 12.75 ns for the transverse velocity (Figures 4.17 and 4.18).

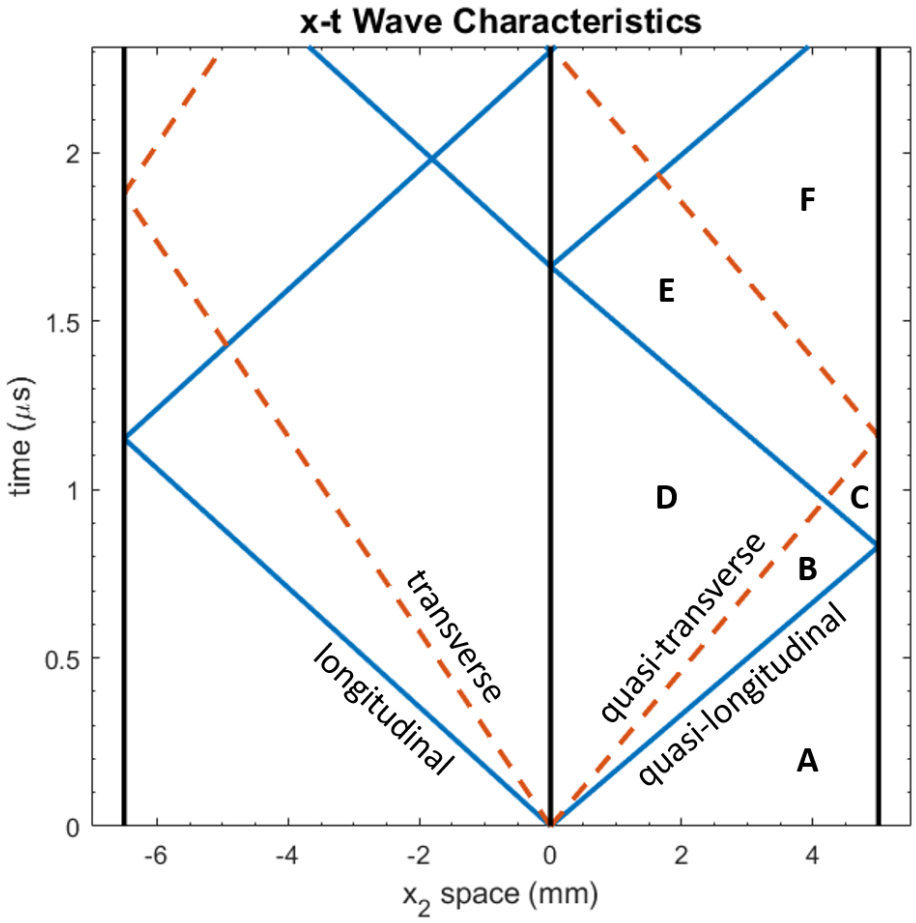

Figure 4.10: An x-t diagram showing the wave characteristics in the flyer plate (-6.5 mm $\leq x_2 \leq 0$ mm) and target plate (0 mm $\leq x_2 \leq 5$ mm).

4.3 Impact Conditions

Tilt

Tilt between the flyer and target plates upon impact can cause experimental values to deviate from their predicted counterparts [30]. This tilt, α, is calculated from the shorting pin signals according to

$$\alpha = \max_{i,j} \left(\left| \tan^{-1} \left(V_0 \frac{(t_i - t_j)}{d_{ij}} \right) \right| \right) \tag{4.3}$$

where $V_0 = 212$ m/s is the flyer plate's velocity, t_i and t_j are the crush times of the i^{th} and j^{th}, and $d_{ij} \approx 32.4$ mm is the distance between pins i and j. At least one, if not two, of the four tilt pins is believed to have malfunctioned during the experiment. Excluding pin three, a worst-case tilt of 5.1 mrad (0.29°) was calculated between pins four and one (4.3).

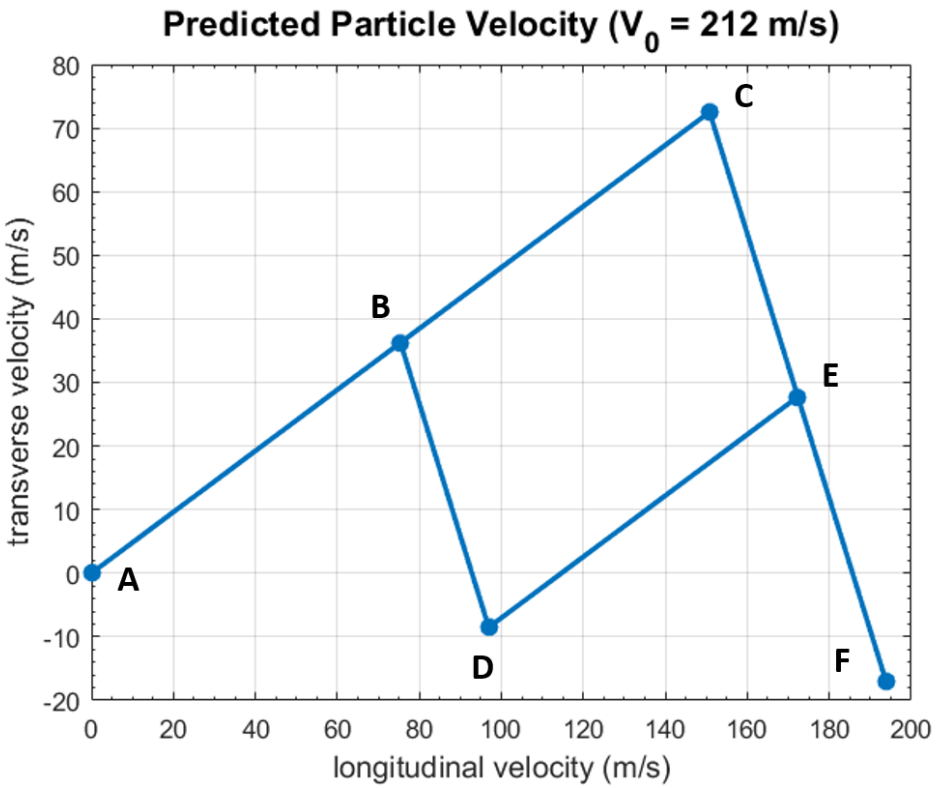

Figure 4.11: Predicted target plate particle velocities for an initial flyer plate (sabot) velocity of 212 m/s. The lettered points correspond to lettered regions in the wave characteristics diagram (Figure 4.10). The longitudinal free surface velocity jumps to 150.79 m/s upon arrival of the QL wave and again to 193.84 m/s upon arrival of the QT wave. The transverse free surface velocity jumps to 72.51 m/s upon arrival of the QL wave and again to −17.02 m/s upon arrival of the QT wave.

Tilt between the impact interfaces affects the relative amount of light returned to the PDV and TPDV probes. Because the TPDV probes are capturing light diffracted at an angle, the PDV-TPDV signals' power ratio worsens with increasing tilt.

Tilt also causes the QL wave to deviate from the quartz crystal's y-direction by [30]

$$\gamma_{QL} \approx \frac{c_{QL}}{V_0}\alpha. \tag{4.4}$$

Using a tilt α of 5.1 mrad and QL wave speed c_{QL} of 6015.64 m/s, the QL wave is predicted to deviate from the y-direction by $\gamma_{QL} \approx 0.14$ rad (8.3°). Using a similar relation, the QT wave traveling at 4318.39 m/s is predicted to deviate from the y-direction by $\gamma_{QT} \approx 0.1$ rad (6°).

Tilt affects the velocity jumps to and from the transient region through γ_{QL} and γ_{QT} [30]. The target plate's ideal QL and QT waves are orthogonally polarized to one

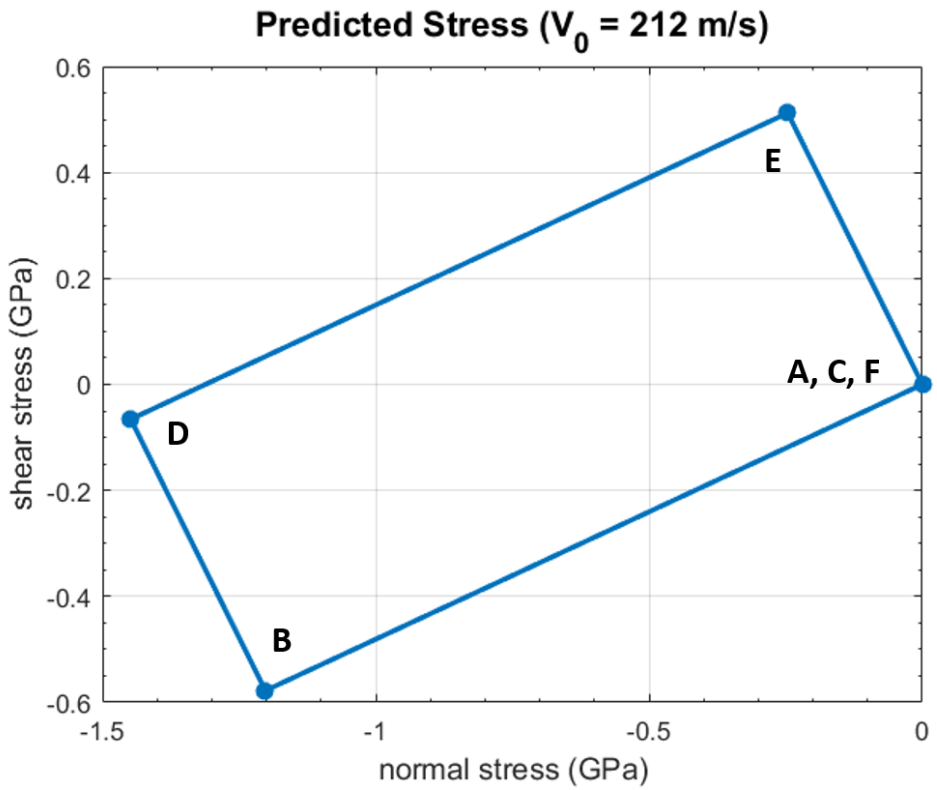

Figure 4.12: Predicted target plate stresses for an initial flyer plate (sabot) velocity of 212 m/s. The lettered points correspond to lettered regions in the wave characteristics diagram (Figure 4.10). The normal traction jumps to −1.2 GPa upon arrival of the QL wave and again to −1.45 GPa upon arrival of the QT wave. The shear traction jumps to −0.58 GPa upon arrival of the QL wave and again to −0.066 GPa upon arrival of the QT wave.

another (2.78)

$$ {}^{t}\boldsymbol{U}^{\mathrm{QL}} \cdot {}^{t}\boldsymbol{U}^{\mathrm{QT}} = \begin{bmatrix} 0 \\ 1 \\ \xi \end{bmatrix} \cdot \begin{bmatrix} 0 \\ -\xi \\ 1 \end{bmatrix} = 0. \tag{4.5} $$

Since the target plate's free surface velocity is proportional to the QL and QT waves' polarization vectors, the transient velocity jump is ideally orthogonal to the final velocity jump.

A plot of transverse velocity v_{yz} against longitudinal velocity v_{yy} graphically shows that the jump in velocity from the transient region due to the arrival of the QT wave was not perfectly orthogonal to the final velocity jump (Figure 4.19). Specifically, the jump upon arrival of the QL wave deviated by 1.7°, and the jump upon arrival of the QT wave deviated by 1.6°.

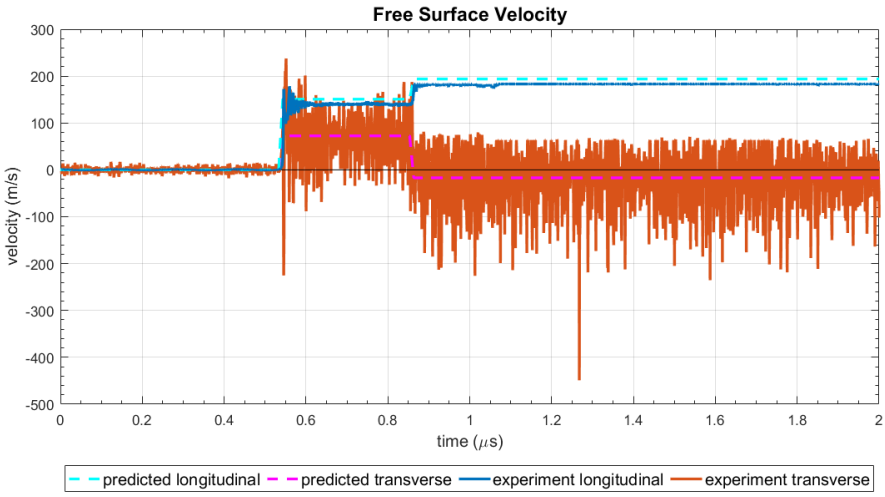

Figure 4.13: PDV-TPDV results for longitudinal and transverse velocities compared to predicted values using a sabot velocity of 212 m/s. STFT specs.: Hamming window, 5 ns window length, window shifted by 15 samples, 2^{15} DFT points.

Because the jump angles are close to ideal, and because the jump angles are not close to γ_{QL} and γ_{QT}, tilt is believed to be less severe than 5.1 mrad. This agrees with optical simulations for different tilt angles using the ratio of power between the PDV and TPDV signals. A high tilt measurement may have been caused by a relatively large variation in shorting pin placement.

Tractions

Jumps in particle velocity produce jumps in traction along the impact face. The jump in normal traction σ_{yy} and shear traction σ_{yz} associated with the QL wave is

$$\begin{bmatrix}\sigma_{yy}\\ \sigma_{yz}\end{bmatrix}_{\mathrm{QL}} = -\frac{1}{2}\rho c_{\mathrm{QL}} v_{\mathrm{QL}} \begin{bmatrix}1\\ \xi\end{bmatrix} \tag{4.6}$$

while the jumps in traction associated with the QT wave is

$$\begin{bmatrix}\sigma_{yy}\\ \sigma_{yz}\end{bmatrix}_{\mathrm{QT}} = -\frac{1}{2}\rho c_{\mathrm{QT}} v_{\mathrm{QT}} \begin{bmatrix}-\xi\\ 1\end{bmatrix} \tag{4.7}$$

where ρ is the material's density, c_{QL} is the QL wave speed, c_{QT} is the QT wave speed, and ξ is from (2.78) [30]. The coefficient v_{QL} is equal to the jump in longitudinal free surface velocity associated with the QL wave while v_{QT} is equal to the jump in transverse free surface velocity associated with the QT wave. Average velocities and associated tractions are found in Table (4.1).

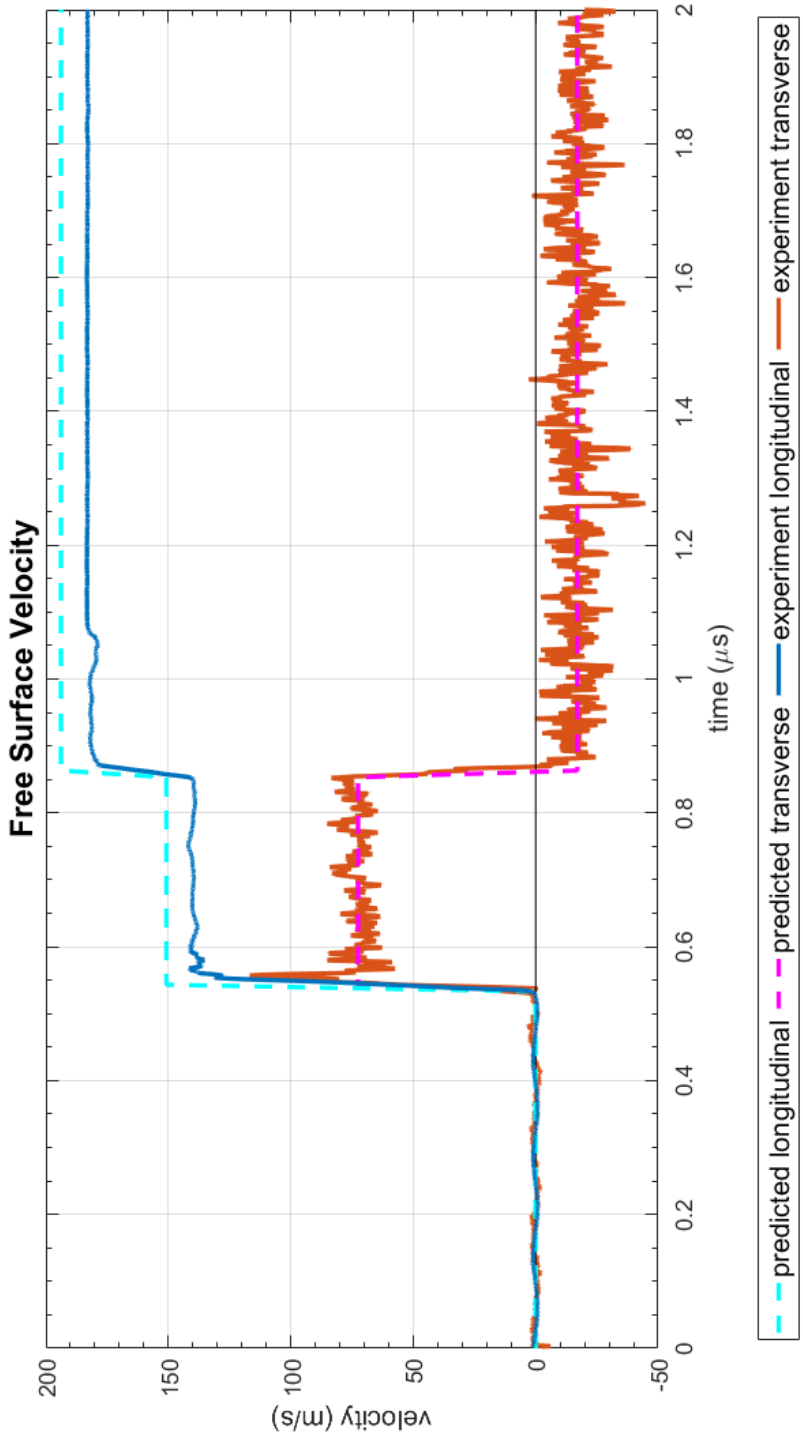

Figure 4.14: PDV-TPDV results for longitudinal and transverse velocities compared to predicted values using a sabot velocity of 212 m/s. The longitudinal velocity rises to a transient of about 139.76 m/s before achieving 182.73 m/s. The transverse velocity rises to a transient of about 72.31 m/s and finally dips to –16.77 m/s. STFT specs.: Hamming window, 5 ns window length, window shifted by 15 samples, 2^{15} DFT points. Post-processing: smoothing using 25 point moving average filter.

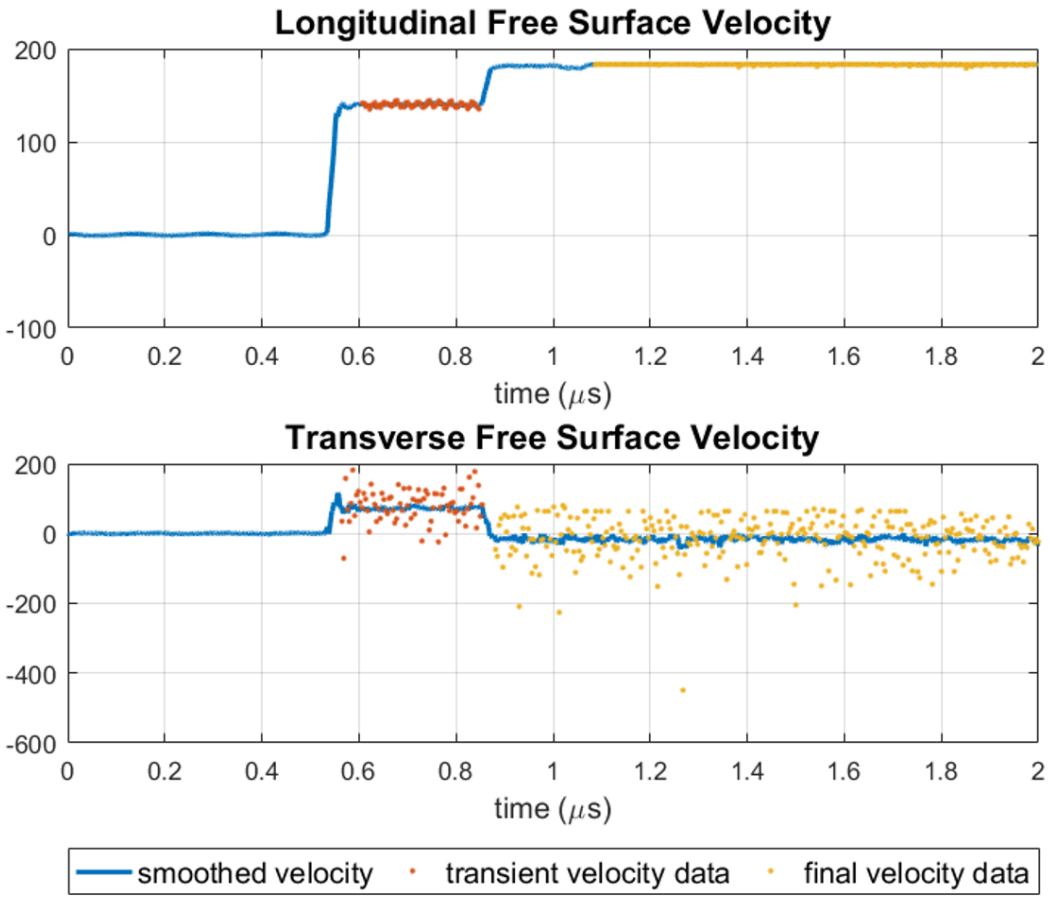

Figure 4.15: Smoothed data overlaid with un-smoothed data show that there are large velocity fluctuations, particularly in the transverse velocity. STFT specs.: Hamming window, 5 ns window length, window shifted by 15 samples, 2^{15} DFT points. Post-processing: smoothing using 25 point moving average filter (blue).

Quantity/Region	Transient	Final
Longitudinal Velocity	139.76 m/s	182.73 m/s
Normal Traction	−1.11 (−1.11) GPa	−1.36 (−1.38) GPa
Transverse Velocity	72.31 m/s	−16.77 m/s
Shear Traction	−0.54 (−0.58) GPa	−0.026 (−0.067) GPa

Table 4.1: Average free surface velocities and tractions. Values not in parentheses are calculated using the ideal $\xi = 0.481$ while values enclose in parentheses are calculated using the 1.7° tilt-corrected $\xi = 0.518$.

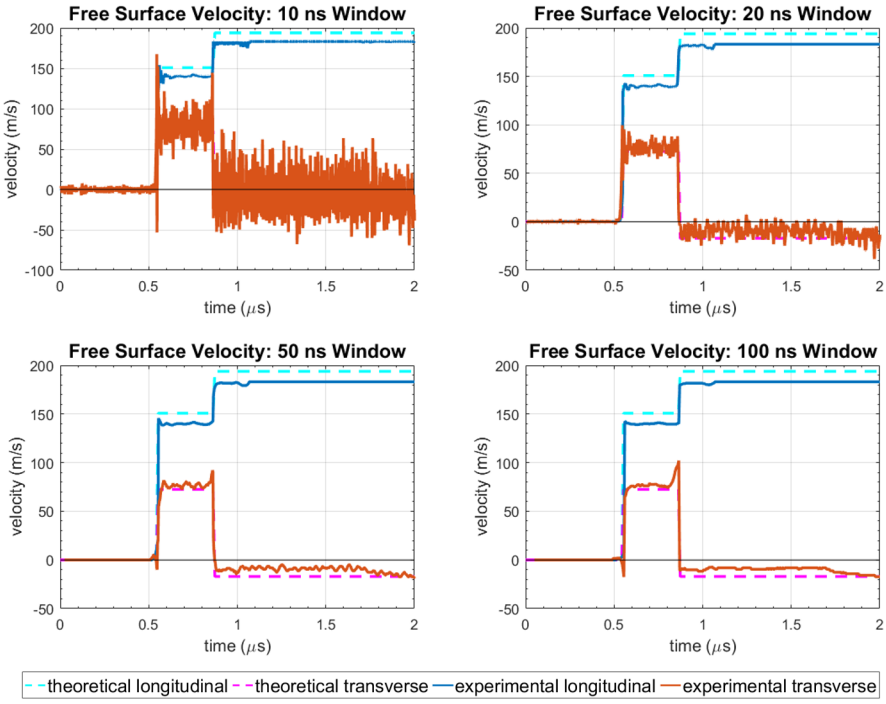

Figure 4.16: The window length τ used to analyze the PDV-TPDV signals greatly affects the frequency – and therefore the velocity – resolution. Smaller window lengths have greater frequency uncertainty than larger windows lengths. However, larger windows lack velocity resolution. STFT specs.: Hamming window, window shifted by 5% of window length, 2^{15} DFT points. Post-processing: due to imprecise knowledge of the start time of the TPDV signal, the transverse velocity was slightly shifted in time to align with the longitudinal velocity and reduce the magnitude of spikes in the transverse velocity.

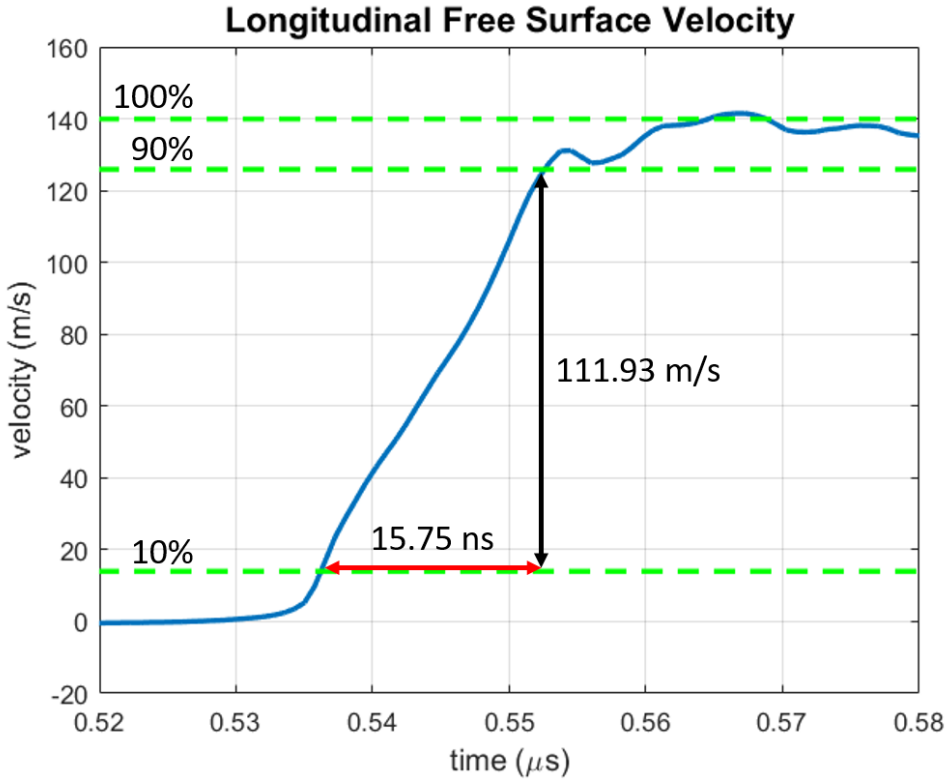

Figure 4.17: The longitudinal velocity 10-90 rise time is approximately 15.75 ns to rise from 13.99 m/s to 125.92 m/s. STFT specs.: Hamming window, 5 ns window length, window shifted by 15 samples, 2^{15} DFT points. Post-processing: smoothing using 25 point moving average filter.

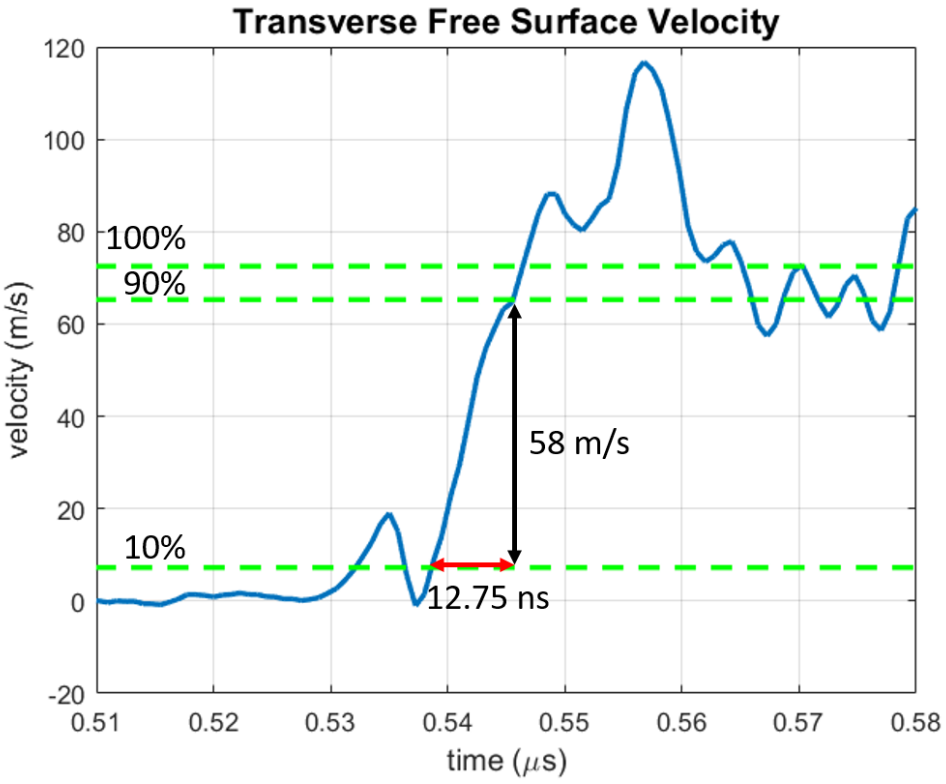

Figure 4.18: The transverse velocity 10-90 rise time is approximately 12.75 ns to rise from 7.25 m/s to 65.26 m/s. STFT specs.: Hamming window, 5 ns window length, window shifted by 15 samples, 2^{15} DFT points. Post-processing: smoothing using 25 point moving average filter.

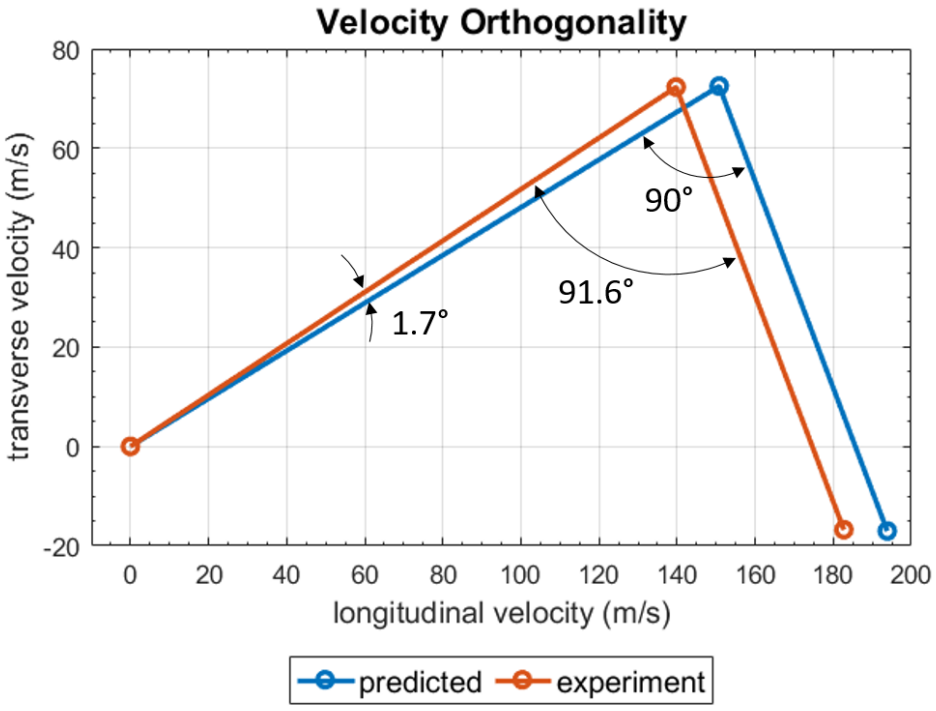

Figure 4.19: The jumps in velocity during the arrival of the QL wave, and later the QT wave, deviated from predicted values. Specifically, the QL wave's polarization vector deviated by 1.7° and the QT wave's polarization vector deviated by 0.1°. An ideal plot has exactly three points since there are three regions of constant longitudinal and transverse velocity. For the experimental data, region averages were taken and the velocity prior to the QL wave's arrival was forced to zero.

Chapter 5

CONCLUSION

Quantifying anisotropic deformation is a complicated endeavor. We built and proved the capabilities of a transverse photonic Doppler velocimetry (TPDV) system that is useful for measuring the longitudinal and transverse velocities of materials during plate impact. Because the TPDV signal was frequency upshifted, spectral analysis techniques produce nanosecond to microsecond time resolutions – even at low velocities during transient events.

High velocity resolution is important when characterizing materials during high-pressure shock loading. For instance, metals with hexagonal symmetry such as Beryllium and Titanium exhibit subtle deformation anisotropy during normal impact that requires a detection device capable of measuring less than 0.8% and 0.25% changes in velocity respectively [28]. In addition, high velocity and time resolution is essential to resolve tiny velocity oscillations caused by shock wave scattering and reflections at interfaces in composite materials [39].

The TPDV will be used to detect shear deformation during pressure-shear plate impact (PSPI) [18]. A collaborator will use the TPDV with the PSPI technique to study high pressure shear waves in fused silica. Fused silica experiences a pressure-induced phase transformation into stishovite during normal shock loading [60, 61]. These experiments will characterize stishovite's constitutive material constants, such as its shear strength, which are important for high pressure material simulations. Understanding the phase transformation of fused silica may reveal mechanisms for stishovite formation in the Earth [62] and during meteorite impact [63].

The TPDV technique does have a major inconvenience – it requires deposition of a diffraction grating on the backside of the target. Quality diffraction gratings, particularly metal gratings for high temperature experiments, are difficult to produce and substantially affect the light return to the PDV-TPDV probes. Developing an extension of the TPDV technique that does not rely on a diffraction grating to detect transverse motion would increase the technique's accessibility for those without technical expertise in grating fabrication and those without access to cleanroom facilities. Further extensions of the TPDV could enable the recording of velocity profiles of surfaces lacking a mirror finish, similar to the Velocity Interferometer

System for Any Reflector [64]. This would streamline sample preparation since a thin reflective coating would not need to be deposited on the back of the target. In addition, similar to the PDV technique, the sensitivity of the TPDV technique can be increased using 1064 nm probing light [65].

Improving the accuracy, precision, and time resolution of displacement measurement techniques is critical to characterizing the properties of materials experiencing impact loading. Awareness of these properties is central to designing better materials for structures [40]. For instance, the interfaces in fiber and layered composites used for spacecraft scatter shock waves and the compressive strength of concrete used for bunkers increases at high strain-rates [66–68]. Even industrial manufacturing techniques harness the power of shock waves [9]. Shock waves are used in explosive welding to bond metals together, diamond synthesis, and rock blasting for mining operations.

Knowledge of shock waves is also critical to understanding Earth's geological processes. For instance, how seismic events such as earthquakes disrupt Earth's surface [69], how meteorite impacts cause ground motion [70], and how meteorite impacts induce mineral metamorphism in craters geology [71]. These applications of shock waves in research and industry, and natural shock events, are a testament that shock waves play an integral role in our world.

Waves are essential to how we comprehend and perceive our surroundings. They dictate how light and sound interact with matter, and how light, sound, and matter change in space and time. Waves are fundamental to the human experience.

BIBLIOGRAPHY

1. Cannon, J. T. & Dostrovsky, S. *The Evolution of Dynamics: Vibration Theory from 1687 to 1742* (Springer-Verlag New York, 1981).
2. Hopkinson, B. A method of measuring the pressure produced in the detonation of high explosives or by the impact of bullets. *Philosophical Transactions of the Royal Society of London. Series A, Containing Papers of a Mathematical or Physical Character* **213,** 437–456 (1914).
3. Field, J., Walley, S., Bourne, N. & Huntley, J. Experimental methods at high rates of strain. *Le Journal de Physique IV* **4,** C8–3 (1994).
4. Gault, D. E. & Wedekind, J. A. The destruction of tektites by micrometeoroid impact. *Journal of Geophysical Research* **74,** 6780–6794 (1969).
5. Melosh, H. J. Impact Ejection, Spallation, and The Origin of Meteorites. *Icarus* **59,** 234–260 (1984).
6. Cintala, M. J. Impact-Induced Thermal Effects in The Lunar and Mercurian Regoliths. *Journal of Geophysical Research-Planets* **97,** 947–973 (1992).
7. Benz, W. & Asphaug, E. Catastrophic disruptions revisited. *Icarus* **142,** 5–20 (1999).
8. King, G. C. P., Stein, R. S. & Lin, J. Static Stress Changes and The Triggering of Earthquakes. *Bulletin of the Seismological Society of America* **84,** 935–953 (1994).
9. Meyers, M. A. in *Dynamic Behavior of Materials* 1–22 (John Wiley & Sons, Inc., 2007). doi:10.1002/9780470172278.ch1.
10. Nemat-Nasser, S. Introduction to High Strain Rate Testing. *Materials Park, OH: ASM International, 2000.* 427–428 (2000).
11. Field, J. E., Walley, S. M., Proud, W. G., Goldrein, H. T. & Siviour, C. R. Review of experimental techniques for high rate deformation and shock studies. *International Journal of Impact Engineering* **30,** 725–775 (2004).
12. Barker, L. M. & Hollenbach, R. E. Interferometer Technique for Measuring the Dynamic Mechanical Properties of Materials. *Review of Scientific Instruments* **36,** 1617–1620 (1965).
13. Stokes, G. G. III. On the aberration of light. *Philosophical Magazine Series 3* **27,** 9–15 (1845).
14. Rafael, F. & Daniel, M. S. Arago (1810): the first experimental result against the ether. *European Journal of Physics* **26,** 195 (2005).
15. Morley, A. A. M. & W., E. On the relative motion of the Earth and the luminiferous ether. *American Journal of Science* (1887).

16. Davis, J. B., Marshall, D. B., Oka, K. S., Housley, R. M. & Morgan, P. E. D. Ceramic composites for thermal protection systems. *Composites Part a-Applied Science and Manufacturing* **30,** 483–488 (1999).

17. Jones, O., Neilson, F. & Benedick, W. Dynamic yield behavior of explosively loaded metals determined by a quartz transducer technique. *Journal of Applied Physics* **33,** 3224–3232 (1962).

18. Gupta, Y. Determination of the impact response of PMMA using combined compression and shear loading. *Journal of Applied Physics* **51,** 5352–5361 (1980).

19. Wenk, H. & Van Houtte, P. Texture and anisotropy. *Reports on Progress in Physics* **67,** 1367 (2004).

20. Manning, P. An optical absorption study of the origin of colour and pleochroism in pink and brown tourmalines. *The Canadian Mineralogist* **9,** 678–690 (1969).

21. Of Encyclopædia Britannica, T. E. *Quartz* Accessed: 2017-05-18. Nov. 2016. `https://www.britannica.com/science/quartz`.

22. Hurcombe, L. M. *Use wear analysis and obsidian: theory, experiments and results* (JR Collis publications Sheffield, 1992).

23. Driscoll, K. *Understanding quartz technology in early prehistoric Ireland* PhD thesis (University College Dublin, 2010). `https://library.ucd.ie/iii/encore/record/C__Rb1872715`.

24. Curie, J. & Curie, P. Développement, par pression, de l'électricité polaire dans les cristaux hémièdres à faces inclinées. *Comptes rendus* **91,** 294–295 (1880).

25. Army, D. o. t. Quartz crystals theory, fabrication, and performance measurements (1950).

26. Cady, W.-G. The piezo-electric resonator. *Proceedings of the Institute of Radio Engineers* **10,** 83–114 (1922).

27. Graham, R. A., Neilson, F. W. & Benedick, W. B. Piezoelectric Current from Shock-Loaded Quartz—A Submicrosecond Stress Gauge. *Journal of Applied Physics* **36,** 1775–1783 (1965).

28. Johnson, J. N. Shock Propagation Produced by Planar Impact in Linearly Elastic Anisotropic Media. *Journal of Applied Physics* **42,** 5522–5530 (1971).

29. Abou-Sayed, A., Clifton, R. & Hermann, L. The oblique-plate impact experiment. *Experimental Mechanics* **16,** 127–132 (1976).

30. Kim, K.-S., Clifton, R. J. & Kumar, P. A combined normal-and transverse-displacement interferometer with an application to impact of y-cut quartz. *Journal of Applied Physics* **48,** 4132–4139 (1977).

31. Luo, S. N. & Ahrens, T. J. Shock-induced superheating and melting curves of geophysically important minerals. *Physics of the Earth and Planetary Interiors* **143,** 369–386 (2004).

32. Bobroff, N. Recent advances in displacement measuring interferometry. *Measurement Science and Technology* **4,** 907 (1993).

33. Helmut, D. & Alfred, J. *Method of producing light-conducting systems* Grant. US Patent 3,480,458. Nov. 1969. https://www.google.com/patents/US3480458.

34. Maurer, R. D. & Schultz, P. C. *Fused silica optical waveguide* Grant. US Patent 3,659,915. May 1972. https://www.google.com/patents/US3659915.

35. Keck, D. & Schultz, P. *Method of producing optical waveguide fibers* Grant. US Patent 3,711,262. Jan. 1973. https://www.google.com/patents/US3711262.

36. Bernsee, G. *Light conducting fibers of quartz glass* Grant. US Patent 3,966,300. June 1976. https://www.google.com/patents/US3966300.

37. Strand, O. T. *et al. Velocimetry using heterodyne techniques* in *26th International Congress on High-Speed Photography and Photonics* (International Society for Optics and Photonics), 593–599.

38. Dolan, D. H. Accuracy and precision in photonic Doppler velocimetry. *Review of Scientific Instruments* **81,** 053905 (2010).

39. Rauls, M. B. *Shock Wave Behavior of Particulate Composites* Dissertation (Ph.D.) (2015). http://resolver.caltech.edu/CaltechTHESIS:05292015-170754625.

40. Hiermaier, S. *Structures under crash and impact: continuum mechanics, discretization and experimental characterization* (Springer Science & Business Media, New York, NY, 2007).

41. Hecht, E. *Optics, 4th* (Addison-Wesley, San Francisco, CA, 2002).

42. Prakash, V. A pressure-shear plate impact experiment for investigating transient friction. *Experimental Mechanics* **35,** 329–336 (1995).

43. Heyliger, P., Ledbetter, H. & Kim, S. Elastic constants of natural quartz. *The Journal of the Acoustical Society of America* **114,** 644–650 (2003).

44. Mello, M. *Optical Interferometry* 2008.

45. *Signal Processing Toolbox Reference* Accessed: 2017-05-17. The MathWorks, Inc., 2017. https://www.mathworks.com/help/pdf_doc/signal/signal_ref.pdf.

46. Gaydecki, P. *Foundations of digital signal processing: theory, algorithms and hardware design* (Institution of Engineering and Technology, 2004).

47. Harris, F. J. On the use of windows for harmonic analysis with the discrete Fourier transform. *Proceedings of the IEEE* **66,** 51–83 (1978).

48. Welch, P. The use of fast Fourier transform for the estimation of power spectra: a method based on time averaging over short, modified periodograms. *IEEE Transactions on audio and electroacoustics* **15,** 70–73 (1967).

49. Daubechies, I. The wavelet transform, time-frequency localization and signal analysis. *IEEE transactions on information theory* **36,** 961–1005 (1990).

50. Liu, S. *et al.* Analysis of photonic Doppler velocimetry data based on the continuous wavelet transform. *Review of Scientific Instruments* **82,** 023103 (2011).

51. Nesse, J. D. *Introduction to optical mineralogy* (Oxford University Press, 1991).

52. Meyers, M. A. in *Dynamic Behavior of Materials* 98–123 (John Wiley & Sons, Inc., 2007). doi:10.1002/9780470172278.ch4.

53. Marsh, S. P. *LASL shock Hugoniot data* (Univ of California Press, 1980).

54. *Borofloat 33 – Mechanical Properties* Accessed: 2017-05-17. Schott North America, Inc. (). http://www.us.schott.com/d/borofloat/e6ba73e8-bb50-4829-b0a7-5a0ccbe36b34/1.0/borofloat33_mech_usa_web2.pdf.

55. Walze, G. *Mikrostrukturierte Oberflächen in Kombination mit optischen Schaltungsmechanismen zum Tageslichtmanagement* Thesis (2006).

56. O'Shea, D. C. *Diffractive optics: design, fabrication, and test* (Spie Press, 2004).

57. Kumar, P. & Clifton, R. J. Optical Alignment of Impact Faces for Plate Impact Experiments. *Journal of Applied Physics* **48,** 1366–1367 (1977).

58. *Curve Fitting Toolbox User's Guide* Accessed: 2017-05-17. The MathWorks, Inc., 2017. https://www.mathworks.com/help/pdf_doc/curvefit/curvefit.pdf.

59. *MATLAB Data Analysis* Accessed: 2017-05-17. The MathWorks, Inc., 2017. https://www.mathworks.com/help/pdf_doc/matlab/data_analysis.pdf.

60. Gleason, A. *et al.* Ultrafast visualization of crystallization and grain growth in shock-compressed SiO2. *Nature communications* **6** (2015).

61. Shen, Y., Jester, S. B., Qi, T. & Reed, E. J. Nanosecond homogeneous nucleation and crystal growth in shock-compressed SiO2. *Nature materials* (2015).

62. Lakshtanov, D. L. *et al.* The post-stishovite phase transition in hydrous alumina-bearing SiO2 in the lower mantle of the earth. *Proceedings of the National Academy of Sciences* **104,** 13588–13590 (2007).

63. Chao, E., Fahey, J., Littler, J. & Milton, D. Stishovite, SiO2, a very high pressure new mineral from Meteor Crater, Arizona. *Journal of Geophysical Research* **67,** 419–421 (1962).

64. Barker, L. M. & Hollenbach, R. E. Laser interferometer for measuring high velocities of any reflecting surface. *Journal of Applied Physics* **43,** 4669–4675 (1972).

65. *Development of a 1064 nm PDV system* (2016). `http://hdl.handle.net/1811/78135`.

66. Zhuang, S., Ravichandran, G. & Grady, D. E. An experimental investigation of shock wave propagation in periodically layered composites. *Journal of the Mechanics and Physics of Solids* **51,** 245–265 (2003).

67. Grote, D., Park, S. & Zhou, M. Dynamic behavior of concrete at high strain rates and pressures: I. experimental characterization. *International Journal of Impact Engineering* **25,** 869–886 (2001).

68. Fang, Q. & Wu, H. in *Concrete Structures Under Projectile Impact* 497–558 (Springer, 2017).

69. Morelli, A., Ekstrom, G. & Olivieri, M. Source properties of the 1997-98 Central Italy earthquake sequence from inversion of long-period and broad-band seismograms. *Journal of Seismology* **4,** 365–375 (2000).

70. Langston, C. A. Seismic ground motions from a bolide shock wave. *Journal of Geophysical Research-Solid Earth* **109,** 23 (2004).

71. Grieve, R. A. F., Langenhorst, F. & Stoffler, D. Shock metamorphism of quartz in nature and experiment .2. Significance in geoscience. *Meteoritics & Planetary Science* **31,** 6–35 (1996).

A p p e n d i x A

EBSD TEXTURE ANALYSIS

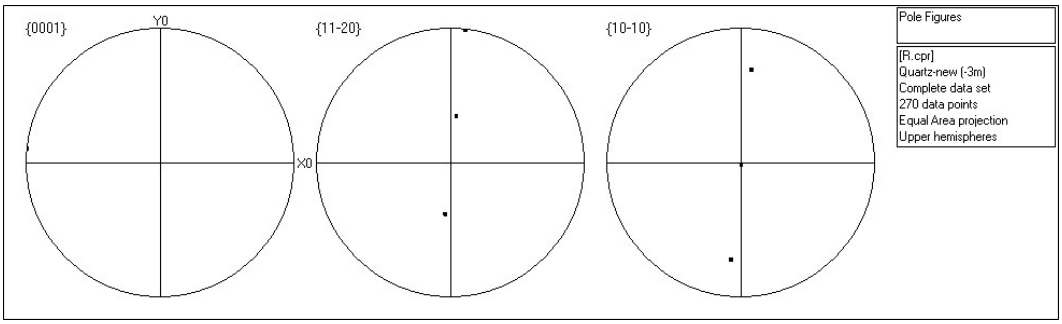

Figure A.1: An EBSD pole figure along the *y*-plane {10-10} shows that the *y*-cut character of this sample is close to ideal.

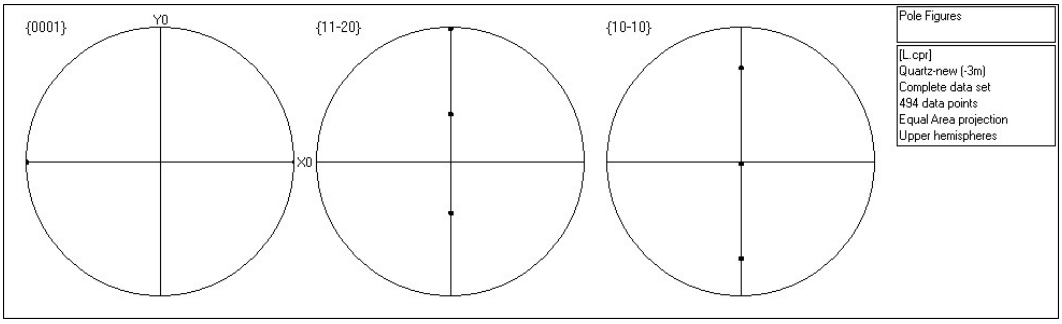

Figure A.2: Another EBSD pole figure along the *y*-plane {10-10} shows that the *y*-cut character of this sample is close to ideal.

Appendix B

SOLID WORKS DRAWINGS

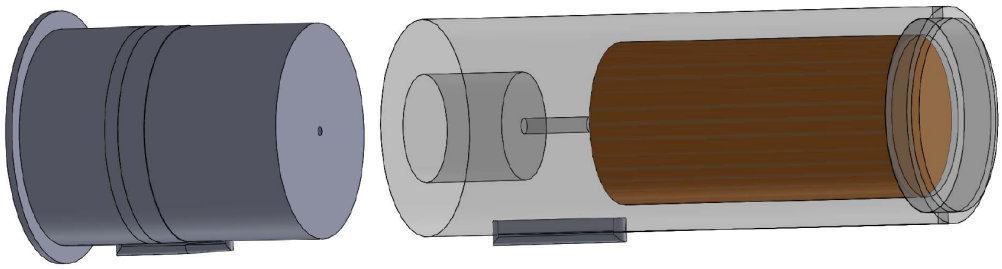

Figure B.1: A Solid Works model of the sabot assembly containing the sabot, metal insert, flyer plate, key, and sealing cap. Courtesy of Christian Kettenbeil.

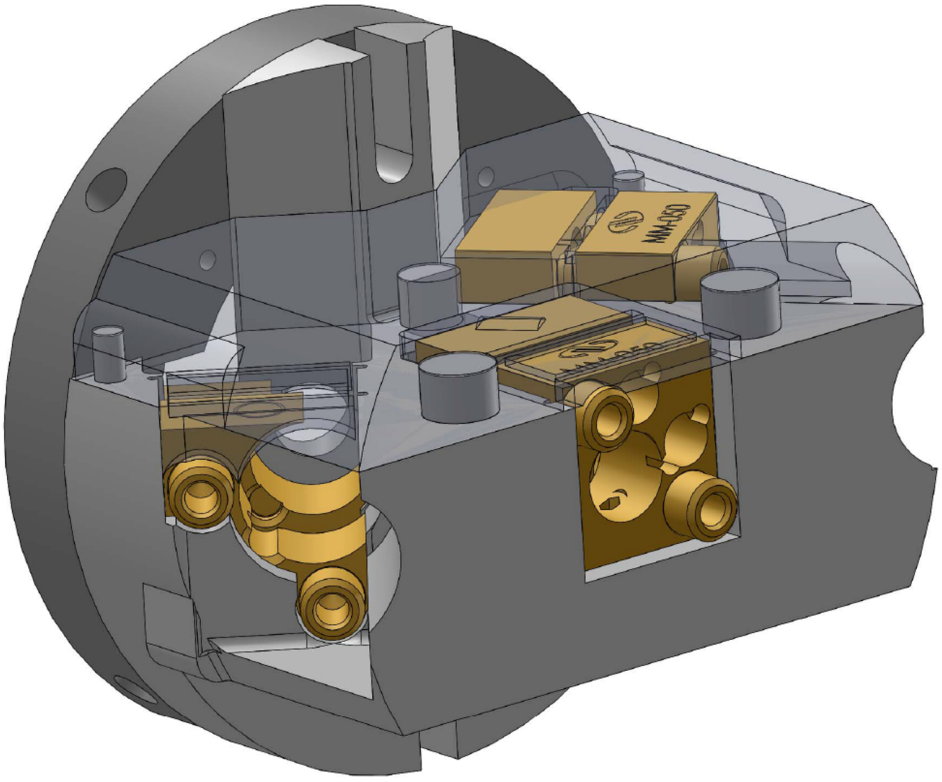

Figure B.2: A Solid Works model of the probe holder containing the probes mounts without the probes. The probe holder is screwed into the specimen holder. Courtesy of Christian Kettenbeil.

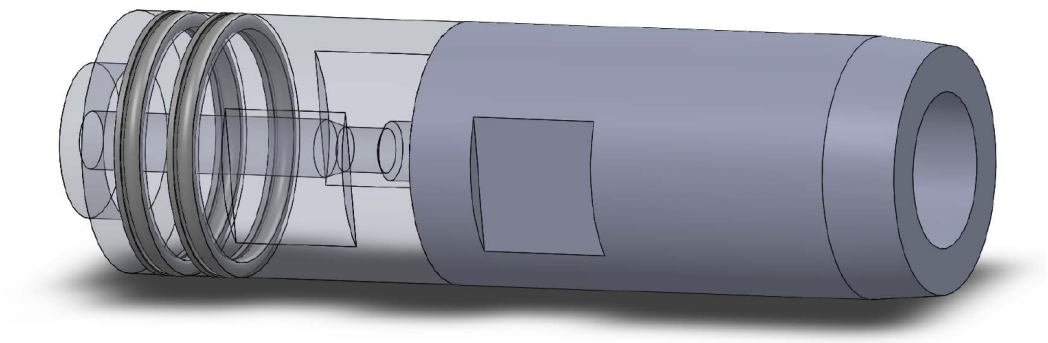

Figure B.3: A Solid Works model of the charge which houses the rifle cartridge and flame splitter (not shown). Courtesy of Christian Kettenbeil.